172 mm

172 mm

64 mm

Dynamics of Paired Bovine Spermatozoa

Kaixuan Zhang

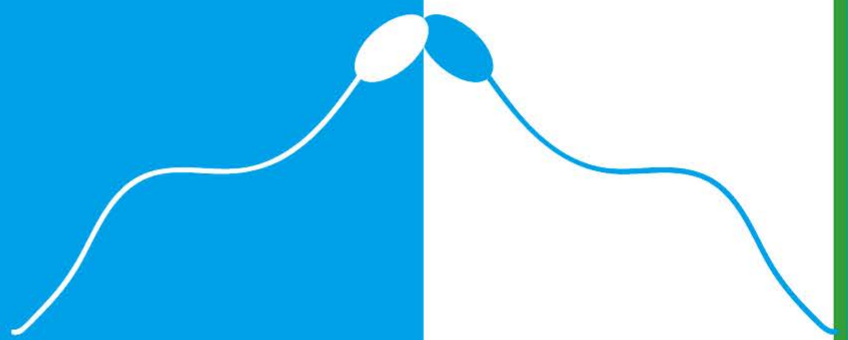

Dynamics of Paired Bovine Spermatozoa

Kaixuan Zhang

Invitation

You are cordially invited to attend the public defense of the PhD thesis title

Dynamics of Paired Bovine Spermatozoa

by

Kaixuan Zhang

Wednesday
9 July 2025 at 11.00 hours

In the Aula of the Academic Building of the University of Groningen

Broestraat 5, Groningen

Paranymphs:

Zihan Wang
Mengyu Gu

244 mm

2 mm bleed

JG

DYNAMICS OF PAIRED BOVINE SPERMATOZOA

Kaixuan Zhang

university of groningen

Dynamics of Paired Bovine Spermatozoa

PhD thesis

to obtain the degree of PhD at the
University of Groningen
on the authority of the
Rector Magnificus Prof. J.M.A. Scherpen
and in accordance with
the decision by the College of Deans.

This thesis will be defended in public on

Wednesday 9 July 2025 at 11.00 hours

by

Kaixuan Zhang

born on 7 April 1994
in Anhui, China

Supervisors

Prof. S. Misra

Dr. I.S.M. Khalil

Assessment Committee

Prof. R. Schirhagl

Prof. Y. He

Prof. P.R. Onck

This work is part of the research project MAESTRO.

This work was supported by the European Research Council (ERC) under the European Union's Horizon 2020 Research and Innovation programme under grant 866494 project-MAESTRO, and financial support from the China Scholarship Council (No. 202006290017) is acknowledged.

This dissertation has been approved by:

Prof. Dr. Sarthak Misra
Dr. Islam S.M. Khalil

Cover design: Kaixuan Zhang
Lay-out: Chuang Li
Printed by: Ipskamp

To those victims of the wars
May their voices be heard
May their stories be remembered
May the fire ignited by their lives illuminate the dark

Samenvatting

Spermatozoa hebben veel aandacht gekregen vanwege hun essentiële rol in seksuele reproductie. Zoogdier-spermatozoa slaan snel met hun flagellen om een lange weg door het vrouwelijke voortplantingsstelsel af te leggen en de eicel te bereiken. Tijdens het reizen schakelen ze tussen verschillende zwemstijlen om zich aan te passen aan de omgeving. Deze opmerkelijke zwemgedragingen hebben biologen en natuurkundigen geboeid en ingenieurs geïnspireerd om zachte microrobots te ontwikkelen die zich kunnen aanpassen aan krappe ruimtes.

Het is experimenteel waargenomen dat spermatozoa coöperatief gedrag vertonen door bundels of paren te vormen waarbij hun koppen aan elkaar hechten. Het bundelen/paren wordt toegeschreven aan evolutionaire selectiedruk, waardoor de zwemsnelheid van de spermatozoa wordt verbeterd. Desondanks blijft ons begrip van dit coöperatieve gedrag beperkt, met nog verschillende onderzoeksvragen die moeten worden opgelost. Bijvoorbeeld, de invloed van het bundelen/paren van spermatozoa op hun kinematica en kinetiek is nog niet volledig begrepen. Experimenteel onderzoek dat de dynamiek van spermatozoa tijdens hun overgang van individuele cellen naar bundels gedetailleerd beschrijft, ontbreekt momenteel. Bovendien is het onduidelijk hoe de flagellaire slagpatronen en de mechanische koppeling tussen spermatozoakoppen de zwemprestaties beïnvloeden. Dit proefschrift heeft als doel deze kennishiaten te overbruggen door middel van zowel experimentele als theoretische benaderingen.

Hoofdstuk 1 biedt een overzicht van de experimentele en theoretische bevindingen met betrekking tot het zwemgedrag van sperma, de onderzoeksuitdagingen die in dit proefschrift worden besproken, en de onderzoeksvragen die in de daaropvolgende hoofdstukken worden behandeld. **Hoofdstuk 2** observeert experimenteel het gehele proces van de overgang van individuele spermatozoën naar paren. De overgang is onderverdeeld in drie fasen: de verre velds-vergrendelingsfase, de rotatie-oscillatiefase en de stabiele-zwemfase. Om de dynamiek van spermatozoa tijdens deze overgang te analyseren, worden tijdsafhankelijke flagellumslaggolven gekarakteriseerd door vier golfvariabelen, d.w.z., de gemiddelde flagellumkromming, de buigingsamplitude, de golflengte en de slagfrequentie. De impact

van spermaparen op de kinematica van spermatozoa wordt aangetoond door deze golfvariabelen, evenals de zwemsnelheden van sperma, vóór en na de paarvorming te vergelijken. Dynamische modellen worden ontwikkeld om de hydrodynamische en/of mechanische interacties tussen de cellen te onderzoeken en om de invloed van de golfvariabelen op de zwemsnelheid en de voortstuwende krachten van de flagellen te voorspellen.

Om de dynamiek van gepaarde spermatozoa nauwkeuriger vast te leggen, ontwikkelt **Hoofdstuk 3** driedimensionale modellen om sperma-geometrie, wandgrenzen, cel-cel hydrodynamische interacties en mechanische kop-kop koppeling te integreren. Hoewel de exacte vorm van de mechanische kop-kop koppeling tot nu toe onbekend is, worden twee potentiële gevallen opgenomen. De flagellaire golfvormen in onze simulaties zijn gereconstrueerd op basis van experimentele metingen. Daarnaast worden gepubliceerde gegevens en onze experimenteel waargenomen zwemtrajecten gebruikt als referentiepunt om onze dynamische modellen te beoordelen. In onze modellen worden de gemiddelde zwemsnelheid, het gemiddelde energieverbruik en de zwemefficiëntie gebruikt om de zwemprestaties van spermaparen met verschillende flagellaire slaappatronen en verschillende kop-kop koppelinggevallen te evalueren. De conclusies van het onderzoek uitgevoerd in **Hoofdstukken 2** en **3** worden gepresenteerd in **Hoofdstuk 4**, gevolgd door een vooruitblik op toekomstig onderzoek naar celbeeldvorming, axonemale dynamica, modellering en toepassingen.

Summary

Spermatozoa have received great attention due to their essential role in sexual reproduction. Mammalian spermatozoa rapidly beat their flagella to travel a long way through the female reproductive tract to meet the ovum. During the traveling, they switch between different swimming gaits to adapt to the environment. These remarkable swimming behaviors have captivated biologists and physicists and inspired engineers to develop soft microrobots adaptive to confined spaces.

Spermatozoa have been experimentally observed to exhibit cooperative behavior by assembling into bundles or pairs with their heads adhered. The bundling/pairing has been attributed to evolutionary selective pressures, whereby sperm swimming speed is enhanced. Nevertheless, our understanding of this cooperative behavior remains limited, with several research questions yet to be resolved. For instance, the influence of sperm bundling/pairing on sperm kinematics and kinetics is not yet fully understood. Experimental research detailing the dynamics of spermatozoa during their transition from individual cells to bundles is currently absent. Additionally, how flagellar beat patterns and the mechanical coupling between sperm heads affect sperm swimming performance remains unclear. This doctoral thesis aims to bridge these research gaps through both experimental and theoretical approaches.

Chapter 1 provides an overview of the experimental and theoretical findings in sperm swimming behaviors, the research challenges confronted in this thesis, and research questions to be addressed in subsequent chapters. **Chapter 2** experimentally observes the whole course of the transition from sperm cells to pairs. The transition is divided into three phases: far field–locking phase, rotational-oscillation phase, and steady-swimming phase. To analyze the dynamics of spermatozoa during this transition, time-dependent flagellar beat patterns are characterized by four wave variables, i.e., mean flagellar curvature, bending amplitude, wavelength, and beating frequency. The impact of sperm pairing on the kinematics of spermatozoa is demonstrated by comparing these wave variables as well as sperm swimming speeds before and after the pair formation. Dynamic models are developed to investigate the hydrodynamic and/or mechani-

cal interactions between the cells and to predict the influence of the wave variables on the swimming speed and flagellar propulsive forces

To more accurately capture the dynamics of paired spermatozoa, **Chapter 3** develops three-dimensional dynamic models to incorporate sperm geometry, wall boundaries, cell-cell hydrodynamic interactions, and mechanical head-head coupling. Although the exact form of the mechanical head-head coupling is hitherto unknown, two potential cases are included. The flagellar waveforms in our simulations are reconstructed from experimental measurements. In addition, published data and our experimentally observed swimming trajectories are used as the benchmark to assess our dynamic models. In our models, average swimming speed, average power consumption, and swimming efficiency are used to assess the swimming performances of sperm pairs with different flagellar beat patterns and distinct head-head coupling cases. Conclusions of research conducted in **Chapters 2** and **3** are presented in **Chapter 4**, followed by an outlook for future research on cell imaging, axonemal dynamics, modeling, and applications.

Contents

1

Introduction

Microorganisms have been one focus of biology since the 17th century when "animalcules", such as bacteria and spermatozoa, were first observed (Figure 1.1). They exist in nearly every corner of biological systems, from plant roots to the human digestive tract, from the soil and water to the air, playing different essential roles. From the perspective of biophysics and cellular locomotion, it is intriguing to know that unicellular microorganisms actively exhibit extraordinary locomotion patterns in response to stimuli. In liquids, swimming microorganisms can effectively spread [1]–[4], forage [5], and evade predators [6]. For instance, when stimulated, *Paramecium* regulates its cilia to swim backward first and then forward in another orientation [7]–[9] (Figure 1.2*A*). *Escherichia coli* bundles and unbundles its flagella to alternate between running and tumbling [10] (Figure 1.2*B*). A similar "run-and-tumble" swimming behavior was also observed in the unicellular alga *Chlamydomonas* (Figure 1.2*C*). For spermatozoa (Figure 1.2*D* and *E*), besides their behaviors in response to stimuli, e.g., chemokinesis [11]–[13], they demonstrate a cooperative behavior by assembling into bundles, most of which are pairs [14]–[16]. Exploring this peculiar and astonishing cooperative strategy of spermatozoa is the first motivation for this thesis.

Another motivation for this thesis is to offer a better understanding of sperm locomotion to facilitate the development of biomedical technologies. The knowledge of spermatozoa has advanced significantly, from a bimillenary debate originating in ancient Greece on the two main ideas about reproduction, i.e., epigenesis and preformationism, to the discovery of the

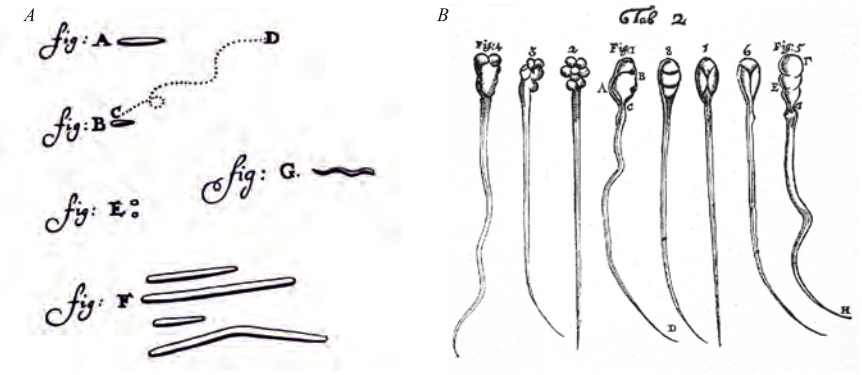

Figure 1.1: The first drawings of bacteria and spermatozoa observed by Anton van Leeuwenhoek. (*A*) These "animalcules" observed in 1674 are suggested to be cocci, bacilli, and spirochetes, respectively [17]. The drawing was initially edited by Clifford Dobell, courtesy of Wellcome Library, London, under Creative Commons Attribution-Share license CC BY-SA 4.0. (*B*) Spermatozoa of the rabbit (the four figures on the left) and the dog (the four figures on the right), from a letter Leeuwenhoek sent to the Royal Society, 1677, courtesy of Wellcome Library, London, CC BY 4.0.

third sperm guidance mechanism, i.e., thermotaxis in recent years [18]–[20]. The deepening knowledge has empowered advancements in contraception and assisted reproduction technologies [21]–[23]. In addition, inspired by sperm swimming behaviors, microrobots for targeted therapy have been developed and applied *ex vivo* [24]–[27]. However, despite many studies on sperm locomotion, their dynamics are not fully understood, especially when they assemble into pairs. Therefore, this doctoral thesis investigates the dynamics of paired spermatozoa. Spermatozoa exhibit morphological diversity across animal species. Except for a limited number of animals, such as *Caenorhabditis elegant* [28] and *Habroleptoides umbratilis* [29], animal sperm cells consist of a head and a flagellum, sharing conserved fundamental functions [30]. Therefore, in this thesis, we focus on the bovine spermatozoon, which is a common cell model for studying mammalian sperm swimming behaviors. Note that spermatozoa are usually not classified as microorganisms nowadays, as they biologically differ from microorganisms that can reproduce. Still, in this thesis, we regard spermatozoa as microorganisms from a perspective of dynamics.

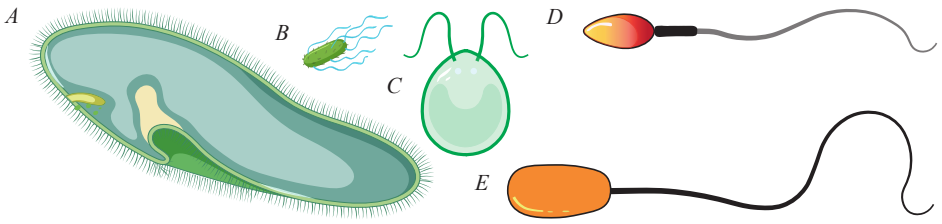

Figure 1.2: Illustration of (*A*) *Paramecium*, (*B*) *Escherichia coli*, (*C*) *Chlamydomonas*, (*D*) human spermatozoon, and (*E*) bovine spermatozoon.

1.1 Swimming Behaviors of Individual Spermatozoa

Spermatozoa vary in morphology among animal species (Figure 1.2*D* and *E*), with most being micro-scale cells. The bovine sperm cell consists of a head resembling a flattened ellipsoid and a flagellum resembling a tube. The total length of a bovine sperm cell, L, is usually 60–90 µm, as shown in Figure 1.2*E*. It swims by propelling the surrounding fluids with its flagellum, achieving a swimming speed on the order of $O(10^1)$ to $O(10^2)$ µm/s. However, it is necessary to point out that the swimming of sperm cells notably differs from the swimming of humans or fish which we may be more familiar with. For a bovine sperm cell swimming in water with speed $U = 200\,\mu\text{m/s}$, the Reynolds number is $Re = \rho U D/\mu \approx 10^{-2}$, where D is the characteristic length of the cell, ρ and μ are the density and dynamic viscosity of water, respectively. The inertia of spermatozoa is negligible, as the Reynolds number represents the ratio of inertial forces to viscous forces per unit volume [31]. Thus, if $Re \ll 1$, swimmers in water cannot coast due to inertia. When exhibiting reciprocal motion at low Re, such as the motion of scallops, they cannot induce a net displacement but an oscillatory motion even after a long time, as first illustrated by Purcell [32]. Nevertheless, spermatozoa can achieve high swimming speed by breaking the motion symmetry with whip-like flagellar beats. It is interesting to find that the flagellum/cilium is a conserved cellular organelle omnipresent in swimming microorganisms. Other microorganisms, such as bacteria [33], green alga [34], and ciliates [35], also use flagella/cilia to swim and/or feed (Figure 1.2).

1.1.1 Responses to Stimuli

In sexual reproduction, the process of spermatozoa swimming a long distance to meet the ovum is stunning. Spermatozoa of marine invertebrates need to locate the ovum in the open seawater. Spermatozoa of mammals must navigate the long female reproductive tract with complex geometry and filled with some cells impairing sperm motility. To reach the oviduct—the fertilization site (Figure 1.3), spermatozoa have evolved some swimming behaviors in response to the external biophysical and biochemical stimuli. When far away from the egg, they are guided by the long-range mechanisms, rheotaxis and thermotaxis (Figure 1.3*A*, *ii*). The rheotaxis guides spermatozoa to swim against the fluid flow (Figure 1.3*B*, *i*) [36]–[39], and thermotaxis guides them to swim toward the warmer spot (Figure 1.3*B*, *ii*) [18]–[20], [40]. While in the short range, spermatozoa exhibit chemotaxis that they swim up toward the chemical gradient (Figure 1.3*A* and *B*, *iii*) [41]–[46]. Contrary to chemotaxis, spermatozoa are recently found to show a chemorepulsive behavior that they swim away from the chemoattractant (Figure 1.3*B*, *iii*) [47], [48].

Besides the guidance mechanisms, spermatozoa show other behaviors, e.g., they tend to swim near the boundary surface rather than the interior space of the fluid environment, as shown in Figure 1.4*A* and *B*. This is known as thigmotaxis [49]–[51], which is thought to increase spermatozoa's chances of meeting the egg [38]. Some of these behaviors may concurrently happen in the sperm cell. Chemokinesis usually accompanies chemotaxis, and rheotaxis coincides if spermatozoa are in a flowing fluid. Interestingly, spermatozoa's responsive behavior to one stimulus is affected by other stimuli. For instance, bovine spermatozoa in a viscoelastic medium (1%PAM+TALP) have a swimming trajectory with larger curvature when exposed to a chemoattractant, 4AP, as shown in Figure 1.4*C*, *i* [13]. While in a viscous medium (TALP), the spermatozoa become more vigorous and swim with less directionality, as shown in Figure 1.4*C*, *ii*. Responding to the changes in medium rheological properties, sperm cells change their flagellar beat and swimming trajectory, which may enhance their motility in the cervical mucus [13], [52], [53]. The aforementioned responsive swimming behaviors to external stimuli have been used for sperm separation and selection [20], [54], [55].

In addition, sperm swimming is regulated by the geometry of environ-

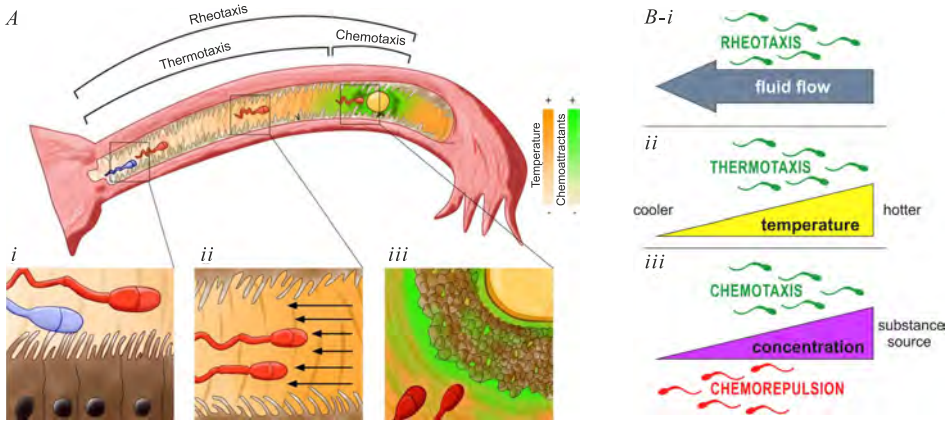

Figure 1.3: (A) Once mammal spermatozoa are capacitated in the lower region of the oviduct (i), they are more sensitive to the gradient of temperature and chemoattractants. They navigate the oviduct by the long-range guidance mechanisms, i.e., rheotaxis and thermotaxis (ii), and the short-range guidance mechanism, chemotaxis (iii). (B) In response to the fluid flow and temperature gradient in the oviduct, mammal spermatozoa swim against the fluid flow and toward the warmer spot, which is known as rheotaxis (i) and thermotaxis (ii), respectively. (iii) Spermatozoa, when near the ovum, can detect and navigate toward it using chemoattractants released by the ovum. Chemorepulsion may also be involved in sperm guidance. Panel (A) is adapted from reference [48] with permission, AME Publishing Company. Panel (B) is adapted from reference [56] with permission, Elsevier.

ments where a larger curvature of the boundary surface induces a larger angle of attack, prolonged physical contact with the boundary, and a lower flagellar beating amplitude (Figure 1.4D) [58]. This spermatozoa's response to the boundary surface curvature within the oviduct may promote their capacitation and fertilization competence. When capacitated, sperm flagellar beat transitions from the progressive pattern, which is symmetric and low-amplitude, to the hyperactivated pattern, which is asymmetric and large-amplitude [59]–[62]. Hyperactivated spermatozoa exhibit higher instantaneous swimming speed but shorter net directional movement. Sperm hyperactivation can be triggered by increased pH or increased concentrations of ATP or Ca^{2+} in the capacitation medium [63]. However, without any changes in the properties and composition of the medium, spermatozoa have also been observed to transition between hy-

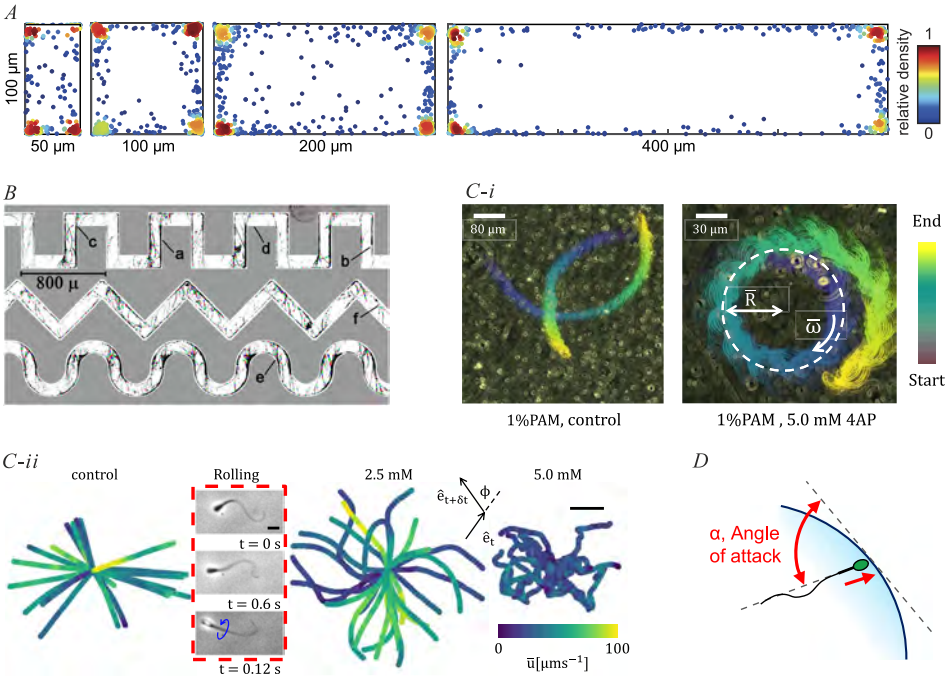

Figure 1.4: Spermatozoa tend to gather in the corner (A) and surface (B) of the boundary. (C) The swimming trajectory of a sperm cell in a viscoelastic medium of 1%PAM (i), and in a viscous medium without PAM (ii). Spermatozoa's response to the chemoattractant, 4AP, is affected by fluid properties. (D) Spermatozoa are encapsulated in droplets with different curvatures to simulate the geometry of the oviduct. Panel (A) is adapted from reference [57], CC BY 4.0. Panel (B) is adapted from reference [49] with permission, National Academy of Sciences. (C) is adapted from reference [13] with permission, American Physical Society. Panel (D) is adapted from reference [58], CC BY 4.0.

peractivated and helical swimming modes [64] (Figure 1.5A), and between a typical three-dimensional (3D) bulk swimming mode and an intermittent two-dimensional (2D) slither swimming mode (Figure 1.5B) [65].

1.1.2 Modeling Sperm Kinematics

Sperm swimming behaviors are biologically complex, while we can quantitatively investigate them from a kinematics or kinetics perspective. Although current mathematical models cannot fully describe sperm swimming

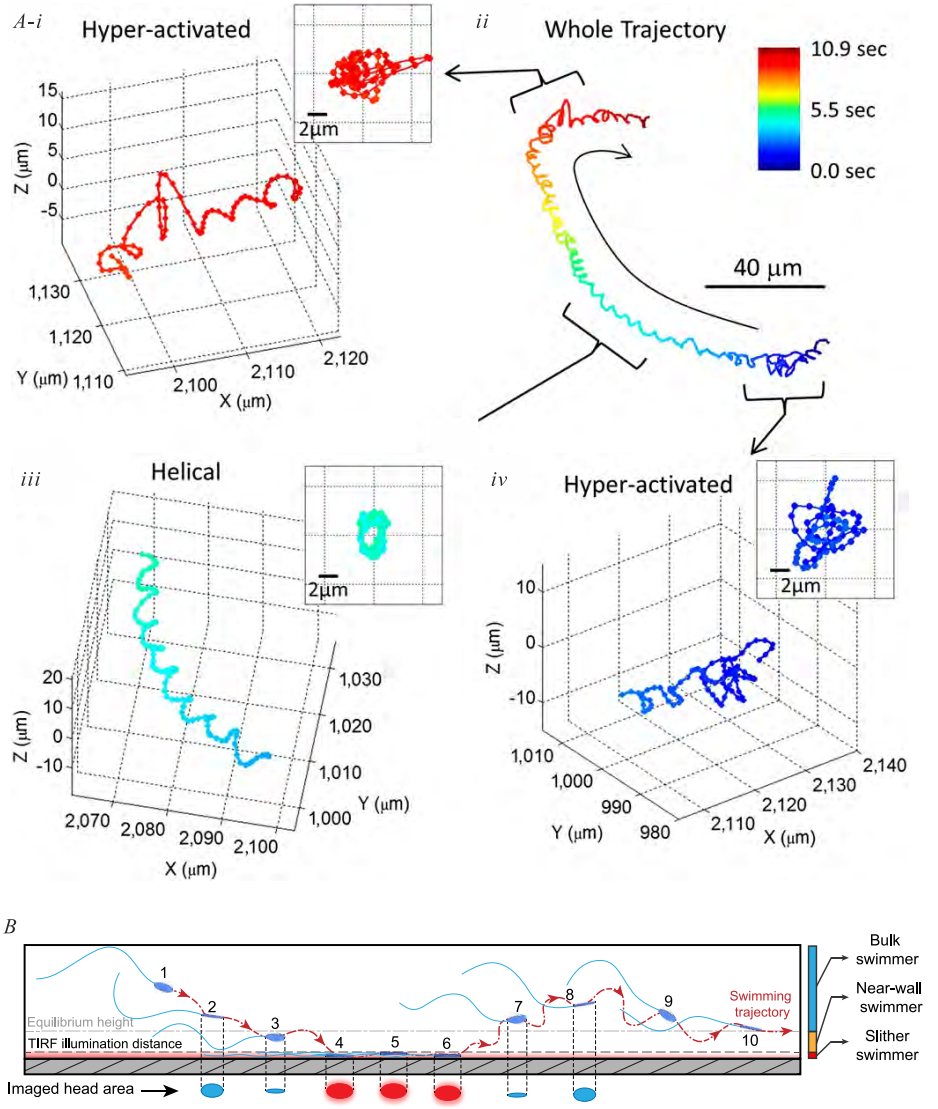

Figure 1.5: (*A*) Sperm swimming trajectory in the 3D space, switching between helical and hyperactivated modes. (*B*) Illustration of the transition from bulk swimming mode to slither swimming mode, in the latter of which the sperm cell is in close proximity to the bottom boundary surface. Panel (*A*) is adapted from reference [64] with permission, National Academy of Sciences. Panel (*B*) is adapted from reference [65], CC BY 4.0.

behaviors, they complement experiments and reveal novel insights that are challenging to obtain experimentally. The theoretical study on the swimming of flagellated microorganisms dates back to the 1950s. As illustrated in Figure 1.6*A*, Taylor ignored the microorganism's head and modeled the flagellum at time, t, in its co-moving frame as a 2D infinite sheet with a transverse sinusoidal wave [66],

$$y' = b\sin(kx' - \omega t), \tag{1.1}$$

where x' and y' are the coordinates in the co-moving frame, b is the amplitude of the wave, k is the wavenumber, and ω is the frequency of the wave. Taylor's analysis indicates that the headless flagellum can swim in the viscous fluid with speed $U = -1/2\omega k b^2$, without external forces acting on it. The swimming direction is opposite to that of wave propagation. Since then, numerous studies have modeled the flagellar bending as a sinusoidal wave [67]–[74].

In addition to being modeled as a sinusoidal wave, flagellar shapes can be extracted from experimental observations and then described mathematically. Spermatozoa often exhibit thigmotactic behavior, tending to accumulate near the boundary surface of a plane [14], [77]–[79]. This behavior simplifies the description of the locomotion of spermatozoa, allowing one to consider the 2D projection of the sperm locomotion on their swimming plane and neglect the out-of-plane component. As illustrated in Figure 1.6*B*, the sperm flagellum can be described by the tangent angle ψ with respect to its co-moving frame spanned by orthogonal unit vectors, $\boldsymbol{e}_1$ and $\boldsymbol{e}_2$ [75], [80]. The vector $\boldsymbol{e}_1$ is parallel with the long axis of the projection of the ellipsoidal head on the swimming plane. The tangent angle at arc-length s, $\psi(s,t), 0 \leq s \leq L$, is enclosed between $\boldsymbol{e}_1$ and the local tangent vector to the flagellar centerline. The sperm head at time t can be characterized with its position vector $\boldsymbol{r}(t)$ and its orientation $\theta(t)$ in the laboratory frame. The orientation $\theta(t)$ is that of the unit vector $\boldsymbol{e}_1$. The point for representing the head position is the head center, which can also be chosen in another position, such as the head tip. Now we can describe the position of an arbitrary point along the flagellum in the laboratory frame by

$$\boldsymbol{r}(s,t) = \boldsymbol{r}(t) - l_{\mathrm{a}}\boldsymbol{e}_1(t) - \int_0^s \left[\cos\psi(s',t)\boldsymbol{e}_1 + \sin\psi(s',t)\boldsymbol{e}_2\right] \mathrm{d}s', \tag{1.2}$$

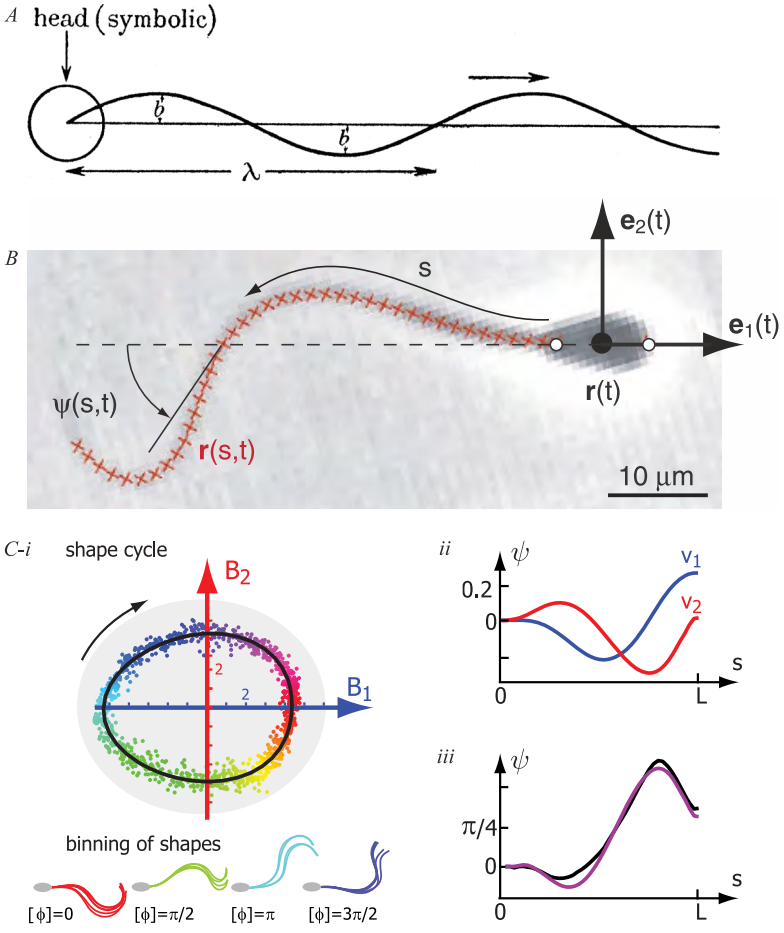

Figure 1.6: (A) The flagellar wave is simplified as a 2D sinusoidal transverse wave with amplitude of b and wavelength of λ. (B) Description of the locomotion of a swimming bovine sperm cell. In the co-moving frame spanned by the orthogonal unit vectors, $\boldsymbol{e}_1$ and $\boldsymbol{e}_2$, the flagellar shape at time, t, is characterized by the tangent angle, $\psi(s,t)$, along the arc-length, $s, 0 \leq s \leq L$. The position vector at any point on the flagellum, $\boldsymbol{r}(s,t)$, is defined with regard to the laboratory frame. (C) According to sperm flagellar shape similarity, the flagellar beats are represented by a limit cycle (i) using principal component analysis. The tangent angle ψ $(ii$ and $iii)$ is reconstructed from the two flagellar shape modes, $\boldsymbol{V}_1$ and $\boldsymbol{V}_2$, and their respective scores, β_1 and β_2, agreeing well with the raw tangent angle. Panel (A) is reproduced from reference [66] with permission, the Royal Society. Panel (B) is reproduced from reference [75] with permission, Company of Biologists. Panel (C) is adapted from reference [76], CC BY 4.0.

where l_a is the semi-major axis of the projection of the ellipsoidal head on the swimming plane, $\boldsymbol{r}(0,t)$ corresponds to the head-flagellum junction, and $\boldsymbol{r}(L,t)$ corresponds to the flagellum distal end (Figure 1.6*B*).

The finer features of flagellar beats can be characterized by four time-dependent wave variables: mean flagellar curvature K_0, bending amplitude A_0, wavelength λ, and beat frequency ω. After ω is experimentally measured, the rest of the wave variables can be determined by

$$K_0 = \frac{\psi_0(s)}{s}, \qquad A_0 = \frac{|\psi_1(s)|}{s}, \qquad \lambda = -\frac{2\pi s}{\arg\psi_1(s)}, \tag{1.3}$$

where ψ_0 and ψ_1 are the zeroth and first Fourier modes of the flagellar tangent angle $\psi(s,t)$ [80]. Here, $\psi(s,t)$ is calculated by

$$\psi(s,t) \approx \psi_0(s) + \psi_1(s)\mathrm{e}^{i\omega t} + \psi_1^*(s)\mathrm{e}^{-i\omega t}. \tag{1.4}$$

The flagellar beat pattern can be reconstructed with these wave variables by

$$\psi(s,t) \approx K_0 s + 2A_0 s\cos(\omega t - 2\pi s/\lambda) \tag{1.5}$$

and Equation (1.2).

As the sperm flagellar beat is regular, it can be regarded as an oscillator to be described by a limit cycle [76], [81]–[83]. Principal component analysis is used to approximate the flagellar tangent angle, $\psi(s,t)$, by

$$\psi(s,t) \approx \psi_0(s) + \beta_1(t)\boldsymbol{V}_1(s) + \beta_2(t)\boldsymbol{V}_2(s), \tag{1.6}$$

where $\psi_0(s)$ is the mean tangent angle [76], [81]. Here, $\boldsymbol{V}_1$ and $\boldsymbol{V}_2$ are the first two flagellar shape modes, and β_1 and β_2 are their respective scores. The two scores form a limit cycle, by which the flagellar beat phase, ϕ, is defined. Specifically, the flagellar beat phase is defined by binning the flagellar shapes according to their shape similarity, as illustrated in Figure 1.6*C*, *i* [81]. Another means to define the flagellar phase is Kralemann's transformation from observations to observable-independent phases [84], [85]. However, Kralemann's transformation cannot be applied to synchronized flagella. We define the sperm flagellar phase using the first means, i.e. the binning of flagellar shapes. Similar to Equation (1.4), Equation (1.6) can be used to reconstruct flagellar tangent angle ψ and hence the flagellar beat pattern, as shown in Figure 1.6*C*, *ii*. Both the two methods (Equations (1.4) and (1.6)) for describing flagellar kinematics account for $> 95\%$ of the variance of ψ.

The sperm swimming trajectory is comprised of structures on two length scales. On a large length scale, the swimming trajectory is circular or helical due to asymmetric flagellar waves [43], [75], [86], as shown in Figure 1.7. On a smaller length scale, the sperm head oscillates during swimming, giving rise to the wiggling trajectory around the average path during one flagellar beat cycle. It is believed that human sperm motility plays a vital role in reproduction, and some variables regarding sperm swimming kinematics are proposed to assess sperm motility and have been used in computer-aided sperm analysis systems (CASAs) [87]–[89]. The variables include the velocity along the curvilinear (VCL), velocity along the average path (VAP), and the amplitude of the lateral displacement of the head (ALH) [90]. Nonetheless, these CASA variables are not mathematically defined and probably vary between instruments. In addition, the values of these CASA variables are subject to some factors such as the measurement duration [91]. The duration of measuring human spermatozoa is recommended to last at least one second by the *WHO laboratory manual for the examination and processing of human semen* [90].

To characterize the displacement of spermatozoa on a finer time scale, net swimming speed, v_{n}, is used, which is the same as VAP but is defined over several beat cycles [75]. Therefore, the net swimming speed over one beat cycle T is defined by $v_{\mathrm{n}} = |(\boldsymbol{r}(t) - \boldsymbol{r}(t+T))|/T$. The speed v_{n} on a finer time scale can well characterize the variation in sperm swimming speed subject to external impacts. The variation in v_{n} also results from the intrinsic phase and amplitude fluctuations of flagellar beating [82]. Moreover, v_{n} depends on the initial phase of flagellar beating. The variation in the values of v_{n} with different initial phases is usually insignificant, and is smaller for a swimming trajectory with smaller curvature.

1.1.3 Modeling Sperm Kinetics

The Reynolds number for spermatozoa $Re \ll 1$, so it is appropriate to use Stokes equations,

$$\mu \Delta \boldsymbol{u} - \nabla p + \boldsymbol{f} = \boldsymbol{0}, \qquad \nabla \cdot \boldsymbol{u} = 0, \tag{1.7}$$

to study their hydrodynamics in the limit of zero Reynolds number of incompressible Newtonian fluid, where $\boldsymbol{u}$ is the fluid flow field, $\boldsymbol{f}$ is a body force applied to the fluid. For an unbounded system with a point force at $\boldsymbol{r}'$

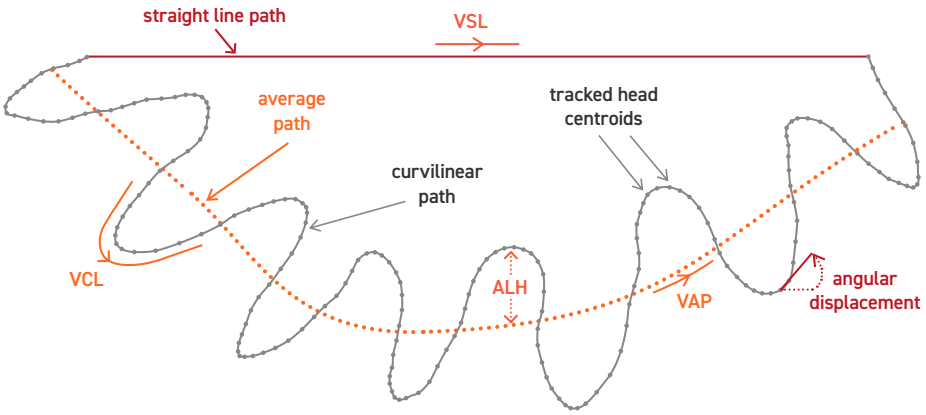

Figure 1.7: Sperm motility is assessed based on its swimming trajectory. This figure is reproduced from reference [90], CC BY-NC-SA 3.0 IGO.

in the Dirac-delta form $\boldsymbol{f}\delta(\boldsymbol{r}-\boldsymbol{r}')$, the flow response at position $\boldsymbol{r}$, termed a Stokeslet, is

$$\boldsymbol{u}(\boldsymbol{r}) = \boldsymbol{G}(\boldsymbol{r}-\boldsymbol{r}')\cdot\boldsymbol{f}, \tag{1.8}$$

where the Oseen tensor $\boldsymbol{G}(\boldsymbol{r})$ is obtained by $\boldsymbol{G}(\boldsymbol{r}) = (1/\boldsymbol{I} + \boldsymbol{r}\boldsymbol{r}/r^3)/(8\pi\mu)$ with the identity tensor $\boldsymbol{I}$ and $r = |\boldsymbol{r}|$. The corresponding pressure field is

$$p(\boldsymbol{r}) = \boldsymbol{H}(\boldsymbol{r}-\boldsymbol{r}')\cdot\boldsymbol{f}, \tag{1.9}$$

where $\boldsymbol{H}(\boldsymbol{r}) = \boldsymbol{r}/(4\pi r^3)$. The sperm cell is immersed in the fluid with a deformable shape. The no-slip boundary condition is applied to its surface, where any point on the surface has an equivalent velocity to the fluid velocity of the corresponding point. Therefore, both the velocities are denoted by $\boldsymbol{u}$.

Equation (1.9) tells a significant feature of Stokes flow that fluid velocity induced by a point force $\boldsymbol{f}$ in the direction parallel with the force, $u_{\parallel}$, is double that in the direction perpendicular to the force, $u_{\perp}$, i.e., $u_{\parallel} = 2u_{\perp}$. The anisotropy is the reason that spermatozoa and other microorganisms can beat their flagella to swim. Except for the Stokeslet, other singular solutions to Stokes equations, like force dipoles and rotlets, can be derived by differentiation. Using the linearity of Stokes equations, one can calculate the flow induced by some geometries with appropriate distribution of the singularities [92]–[94]. The drag force for a slender rod moving at a low Re

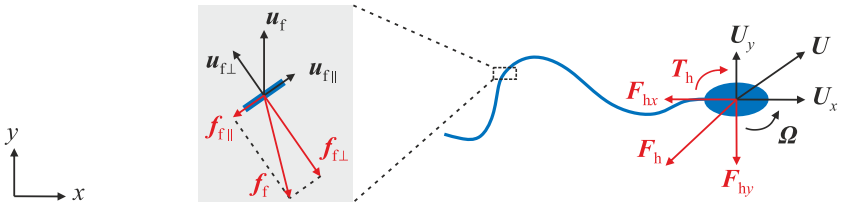

Figure 1.8: Drag on a swimming sperm cell. Because of the drag coefficients $\xi_\parallel < \xi_\perp$, the drag force of a segment of the flagellum, $\boldsymbol{f}_\mathrm{f}$, has a component perpendicular to the direction of the velocity of the segment, $\boldsymbol{u}_\mathrm{f}$. The drag force, $\boldsymbol{F}_\mathrm{h}$, and torque, $\boldsymbol{T}_\mathrm{h}$, on the head counteract those on the flagellum.

can be roughly derived by distributing a line of Stokeslets along the rod [31], which is better approximated by slender body theory (SBT) involving the distribution of Stokeslets and source dipoles along the rod [95]. For an arbitrary segment of a flagellum at the position s along the arc, the drag force $\boldsymbol{f}_\mathrm{f}(s)$ is

$$\boldsymbol{f}_\mathrm{f}(s) = -\xi_\parallel \boldsymbol{u}_{\mathrm{f}\parallel}(s) - \xi_\perp \boldsymbol{u}_{\mathrm{f}\perp}(s), \tag{1.10}$$

where $\boldsymbol{u}_{\mathrm{f}\parallel}$ and $\boldsymbol{u}_{\mathrm{f}\perp}$ are the velocity components of the flagellum segment in the directions parallel and perpendicular to the segment, respectively, as illustrated in Figure 1.8. Here, $\xi_\parallel$ and $\xi_\perp$ are the corresponding drag coefficients. For a thin flagellum with diameter d propagating in the sine waveform with wavelength λ [96], [97], Gray and Hancock developed the well-known resistive force theory (RFT) and derived the values of the drag coefficients, although the values were revised later. The values of the drag coefficients depend on the geometry. For a rod with length L and maximum diameter d [98], its drag coefficients are

$$\xi_\parallel = \frac{2\pi\mu}{\ln(2L/d) + \zeta}, \qquad \xi_\perp = \frac{4\pi\mu}{\ln(2L/d) + \zeta + 1}. \tag{1.11}$$

Here, $\zeta = -1/2$ for a rod with uniform diameter along its axis. Equation (1.11) indicates that the drag force on a flagellum is anisotropic.

The bovine sperm flagellum is a little wider at the base and tapers at the distal end [99]–[101], which is often regarded as a tube with a uniform diameter. Therefore, the total drag force experienced by a flagellum at time t is

$$\boldsymbol{F}_\mathrm{f}(t) = -\int_0^L [\xi_\parallel \boldsymbol{u}_{\mathrm{f}\parallel}(s,t) + \xi_\perp \boldsymbol{u}_{\mathrm{f}\perp}(s,t)]\mathrm{d}s. \tag{1.12}$$

The flagellar beat during a cycle T is non-reciprocal, hence $|\int_0^T \boldsymbol{F}_\mathrm{f}\,\mathrm{d}t| > 0$. Note that the RFT for a planar flagellum cannot accurately capture its hydrodynamics when the condition $L \gg d$ is not satisfied. The helical flagellum must satisfy more geometrical conditions to validate the RFT [102]. Nevertheless, the RFT offers a feasible and useful tool to reveal some significant hydrodynamic features of flagella [75], [94], [103].

As illustrated in Figure 1.8, the prolate spheroidal head at low Re with semi-major axis l_a and semi-minor axis l_b moving in an unbounded fluid with velocity $\boldsymbol{U}$ experiences drag forces,

$$\boldsymbol{F}_{\mathrm{h}x} = -6\pi\mu l_\mathrm{a} C_1 \boldsymbol{U}_x, \qquad \boldsymbol{F}_{\mathrm{h}y} = -6\pi\mu l_\mathrm{a} C_2 \boldsymbol{U}_y, \tag{1.13}$$

where $C_1 = \frac{8}{3}e^3 \Big/ \left[(e^2+1)\ln\frac{1+e}{1-e} - 2e\right]$, $C_2 = \frac{16}{3}e^3 \Big/ \left[(3e^2-1)\ln\frac{1+e}{1-e} + 2e\right]$, the eccentricity $e = \sqrt{1 - l_\mathrm{b}^2/l_\mathrm{a}^2}$ [92], [104]. The subscripts x and y in Equation (1.13) represent the x- and y-components. The drag forces can also be determined by Equations (1.10) and (1.11) with $\zeta = \ln 2 - 3/2$ [98], which asymptotically approximates the results of Equation (1.13). The drag torque, $\boldsymbol{T}_\mathrm{h}$, of the prolate spheroid with angular velocity $\boldsymbol{\Omega}$ can be determined by

$$\boldsymbol{T}_\mathrm{h} = -8\pi\mu l_\mathrm{a} l_\mathrm{b}^2 C_3 \boldsymbol{\Omega}, \tag{1.14}$$

where $\boldsymbol{\Omega} = \Omega \boldsymbol{e}_3$, $\boldsymbol{e}_3 = \boldsymbol{e}_1 \times \boldsymbol{e}_2$, and

$$C_3 = \frac{4}{3}e^3 \left(\frac{2-e^2}{1-e^2}\right)\left[(e^2+1)\ln\frac{1+e}{1-e} - 2e\right]^{-1}.$$

As spermatozoa are self-propelled and neutrally buoyant, they are force-free and torque-free, such that

$$\boldsymbol{F} = \boldsymbol{F}_\mathrm{h} + \boldsymbol{F}_\mathrm{f} = \boldsymbol{0}, \quad \boldsymbol{T} = \boldsymbol{T}_\mathrm{h} + \boldsymbol{T}_\mathrm{f} = \boldsymbol{0}, \tag{1.15}$$

where $\boldsymbol{F}_\mathrm{h}$ is the total hydrodynamic force on the head, $\boldsymbol{T}_\mathrm{f}$ is the total hydrodynamic torque on the flagellum.

More generally, for a self-propelled swimmer, which locomotes by deforming its shape, the swimming problem lies in determining its swimming velocity. Mathematically, the shape deformation of a self-propelled swimmer could be diverse and even unnecessarily exist physically. Examples include a three-link swimmer or a n-link swimmer with their arms rotating relatively (Figure 1.9*A*) [32], [110]–[112], a filament or a sheet with a

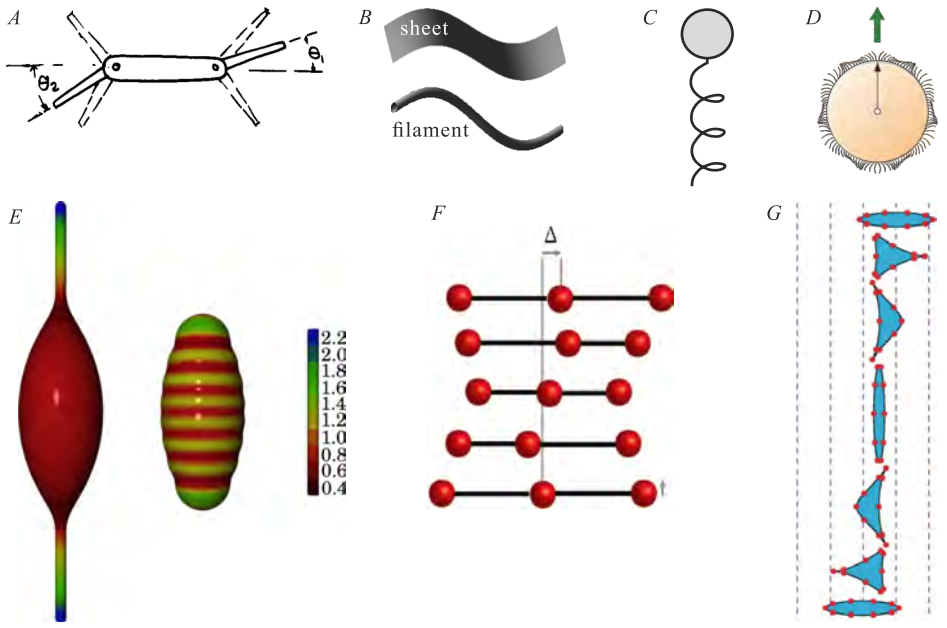

Figure 1.9: (A) Purcell's three-link microswimmer. (B) A sperm cell is simplified to a 2D sheet or a 3D filament. (C) A swimming bacterium with its flagellum represented by a rigid helix. (D) A ciliated swimmer. (E) Two squirmers with distinct geometries. (F) A three-sphere swimmer moves horizontally with time. (G) A 2D closed curve moves horizontally with time. Panel (A) is reproduced from reference [32] with permission, AIP Publishing. Panel (B) is adapted from reference [69] with permission, AIP Publishing. Panel (C) is adapted from reference [105] with permission, Elsevier. Panel (D) is adapted from reference [106], CC BY 4.0. Panel (E) is reproduced from reference [107] with permission, American Physical Society. Panel (F) is adapted from reference [108] with permission, American Physical Society. Panel (G) is reproduced from reference [109] with permission, American Physical Society.

traveling wave (Figure 1.6A and Figure 1.9B) [66]–[69], [113], a bacterium with a rigid helical flagellum rotating about its axis (Figure 1.9C) [105], [114], [115], a ciliated body with a beating cilium array (Figure 1.9D) [106], [116], [117], a squirmer with its surface tangentially slipping (Figure 1.9E) [106], [107], [118]–[120], a two-sphere or a three-sphere swimmer with the distance between its spheres extending and shortening (Figure 1.9F) [108], [121]–[123], and a shape-changing 2D closed curve (Figure 1.9G) [109]. In

the swimming problem of these swimmers, their translational swimming velocity, $\boldsymbol{U}$, and angular velocity, $\boldsymbol{\Omega}$, with respect to the laboratory frame are unknown, while the velocity of an arbitrary point on the swimmers with respect to their co-moving frames, $\boldsymbol{v}$, is usually known. The co-moving frame of reference for a swimmer is fixed to one point on the swimmer. The velocity, $\boldsymbol{u}$, of an arbitrary point at $\boldsymbol{r}$ on a swimmer with respect to the laboratory frame is thus specified by

$$\boldsymbol{u} = \boldsymbol{v} + \boldsymbol{U} + \boldsymbol{\Omega} \times \boldsymbol{r}. \tag{1.16}$$

Equations (1.7), (1.15) and (1.16) complete the kinetics of the swimmers, given the no-slip boundary condition (for e.g., spermatozoa) or a specific slip boundary condition (for e.g., squirmers). Specifically, the sperm translational and angular velocities are represented by those of a fixed point on the sperm head. For simplicity, the fixed point is usually chosen to overlap with the origin of the co-moving frame attached to the sperm head. Therefore, $\boldsymbol{v} \equiv 0$ holds for any point on the head, while $\boldsymbol{v} \not\equiv 0$ holds for any point on the sperm flagellum, except for the head-flagellum junction. The velocity $\boldsymbol{v}$ is prescribed by a sinusoidal wave (Figure 1.6*A*) or experimental measurements of time-varying flagellar shapes (Figure 1.6*B*). Note that the velocity $\boldsymbol{u}$ is unnecessarily expressed in the form of Equation (1.16). In some models for spermatozoa [73], [74], [124]–[126], $\boldsymbol{v}$ is not given explicitly, and Equation (1.16) is replaced with another boundary condition, leaving the swimming problem still well-posed.

1.1.4 Wall Effects

Mammal spermatozoa have evolved many swimming behaviors to navigate the female reproductive tract with complex boundaries as introduced above [49], [57], [65]. Physically, boundaries largely modify the flow field and induce hydrodynamic interaction between spermatozoa and boundaries. The boundary can be solid or deformable. The boundary of the mammalian oviduct should be considered deformable as it is covered with motile cilia [127], [128]. Purcell's scallop theorem does not hold for spermatozoa near the deformable boundary [129]–[132]. However, spermatozoa are often observed *in vitro*, such as in a chamber where the boundary surface is solid. With the presence of a solid plane wall, some wall effects emerge. Closer proximity to the surface increases the viscous drag on a moving body, and

the drag coefficients of a flagellum (Equation (1.11)) need to be revised according to the distance between the wall and the body [98]. Accordingly, the power consumption P increases. Increased viscous drag slows down a moving body with constant power but increases the swimming speed of a moving body with prescribed flagellar waveforms, such as Taylor's sheet as shown in Figure 1.6A [66] and a sperm cell [86] as shown in Figure 1.10A. In addition, the presence of a solid wall has been found to reorient swimming spermatozoa. A sperm cell is reoriented perpendicular (parallel) to a plane wall when its flagellar shape is asymmetric (symmetric) [133].

Spermatozoa can detach from the wall only when their flagellar waveforms exhibit both high asymmetry and amplitude (Figure 1.10B) [134], a behavior that may enhance their chances of fertilization by breaking their binding to the oviduct epithelium, where they become hyperactivated and display such waveforms [59]–[62]. Whether spermatozoa are trapped or escape from a wall depends on their flagellar waveforms [135], [136]. The transition between pushers and pullers has been found in some microswimmers [137], [138], which may account for the wall-trapping or wall-repelling effect of spermatozoa. The wall effects have also been found in other microorganisms, like *Chlamydomonas* and *Escherichia coli* [139]–[144].

The presence of a solid wall presents challenges to theoretical modeling. To address the challenge, a few methods have been proposed. One of them is the method of images [145]–[147]. The idea of the image method is to identify the mirror image of the point force across the wall on the fluid. The image point lies outside the fluid domain and is superposed by singular solutions of the Stokes equations, such as the rotlet, stresslet, and dipole. However, moving bodies with complex geometry increase the difficulty in deriving the linear superposition of singularities to satisfy the no-slip boundary condition on the surfaces of the wall and moving bodies. Furthermore, certain distributions of singularities are non-integrable, rendering this method inapplicable.

Cortez considered a force to be applied over a small ball instead of a point and therefore proposed the regularized Stokeslets method (RSM), which relies on a modified expression for the Stokeslet [148]. The RSM is a good approximation of the fluid flow with no necessity to resort to higher-order singularities. The sperm surface and wall surface can be distributed with n_1 and n_w regularized Stokeslets, respectively. The flow response at

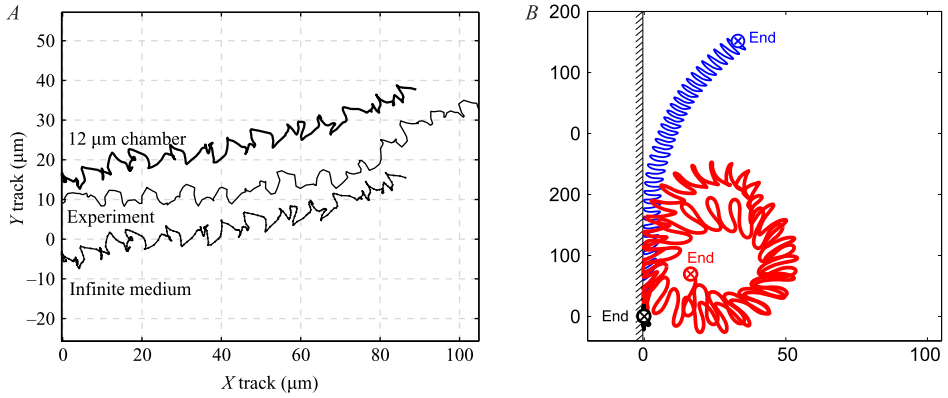

Figure 1.10: (A) The swimming trajectory of a sperm cell is affected by the chamber depth. Closer proximity to the wall increases the sperm swimming speed. (B) The swimming trajectory of a sperm cell with three distinct flagellar waveforms. The cell can only escape from the wall with asymmetric and high-amplitude flagellar waveforms. Panel (A) is adapted from reference [86] with permission, Cambridge University Press. Panel (B) is adapted from reference [134] with permission, Elsevier.

$\boldsymbol{r}_0$ to forces $\boldsymbol{f}_n$ is

$$\boldsymbol{u}\left(\boldsymbol{r}_0\right) = \frac{1}{8\pi\mu} \sum_{n=1}^{n_1+n_\mathrm{w}} \sum_{i=1}^{3} S_{ij}^{\epsilon}\left(\boldsymbol{r}_n, \boldsymbol{r}_0\right) A_n \boldsymbol{f}_{n,i}, \quad i = 1, 2, 3, \tag{1.17}$$

where A_n is the quadrature weight of the nth regularized Stokeslets, $\boldsymbol{f}_{n,i}$ is the ith component of the force $\boldsymbol{f}_n$, ϵ is the regularization parameter [149]. If the velocity of any point, $\boldsymbol{u}$, is known, the forces $\boldsymbol{f}_{n,i}$ can be determined by Equation (1.17). If $\boldsymbol{u}$ is unknown but the velocities of part of the points such as the points on the sperm flagellum in its co-moving frame, $\boldsymbol{v}$, are known, the translational and angular velocities of the sperm cell and the forces on the cell can be solved by combining Equations (1.15) to (1.17) [86]. Equation (1.17) can be applied to spermatozoa swimming in an unbounded fluid by simply removing the regularized Stokeslets on the wall. More walls can also be incorporated by distributing regularized Stokeslets on the walls. For two special cases, i.e. swimming near one plane wall and swimming confined by two parallel plane walls, one wall can be replaced with a system of images, thereby saving computational resources [147], [150], [151]. In this thesis, we choose to discretize two parallel walls.

1.2 Interactions between Spermatozoa

Collective motion is omnipresent in nature, from inanimate objects to motile cells, from actin filaments to animal groups [152]. Sperm cells have been found to form clusters. Within each cluster, cells are aligned, as shown in Figure 1.11*A*. The cluster size and the cell-cell orientation alignment strength are increased by the elastic component of the fluid and cell density [52]. Above a critical cell density, sperm cells further form a turbulence-like structure (Figure 1.11*B*) and a vortex array (Figure 1.11*C*). This spatiotemporal pattern shows two length scales: 1) the smaller structure, i.e., the turbulence-like structure or the vortex structure in one cluster, and 2) the larger structure, i.e., the array formed by the clusters. The structures of both the two scales and associated fluid flow are mediated by sperm density and the chamber depth [153], [154]. The experimental observations indicate that the correlated smaller structures can be formed by hydrodynamic interactions without chemical signals involved. In addition, spermatozoa have been observed to adhere to bundles. The bundle size varies from two to hundreds of cells. They are physically attached at the flagellum (Figure 1.11*D*) or the head (Figure 1.11*E* and *F*) [14], [155], [156]. Considering that the mechanical force due to the attachment between spermatozoa plays an important role in their interactions, in this section, interactions between spermatozoa are reviewed under two categories: 1) the cluster of spermatozoa that swim nearby but separately, and 2) the bundle of attached spermatozoa.

1.2.1 Separate Spermatozoa

There are two common frameworks for investigating the interaction between spermatozoa. The first one is from a perspective of statistical mechanics, i.e., measuring the percentage of spermatozoa that form clusters, the cluster size, the flagellar waveforms, the sperm swimming speed, etc., and calculating correlation functions of the structures regarding quantities such as velocity and vorticity (Figure 1.11*A*–*C*) [52], [153], [154]. The other framework is to incorporate spermatozoa into a dynamic model.

Different dynamic models have been developed. We briefly review some. The first represents each spermatozoon with discrete particles linked by springs, while the surrounding fluid is simulated using a particle-based

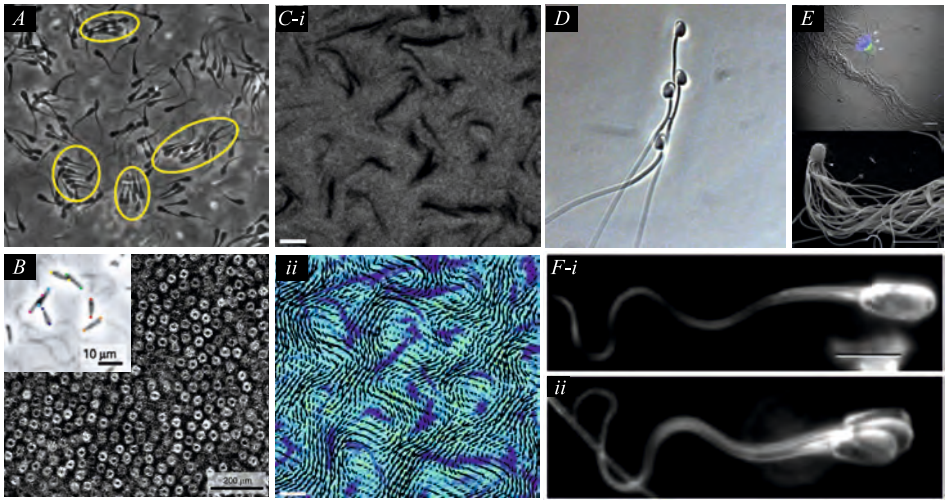

Figure 1.11: (*A*) Bovine spermatozoa form clusters in a viscoelastic fluid. (*B*) Bovine spermatozoa form vortex arrays when reach a critical sperm density. (*C*) Bovine spermatozoa form a turbulence-like structure (*i*) and induce a flow field (*ii*), measured by PIV. (*D*) The heads of *Peromyscus* spermatozoa are attached at flagella. (*E*) *Cataglyphis savignyi* spermatozoa are attached at the head. (*F*) Two (*i*) and three (*ii*) bovine spermatozoa are attached at the head. Panel (*A*) is reproduced from reference [52], CC BY 4.0. Panel (*B*) is adapted from reference [153] with permission, AAAS. Panel (*C*) is adapted from reference [154] with permission, American Physical Society. Panel (*D*) is adapted from reference [155] with permission, Springer Nature. Panel (*E*) is reproduced from reference [156] with permission, the Royal Society. Panel (*F*) is adapted from reference [14] with permission, Company of Biologists.

mesoscopic model known as multiparticle collision dynamics (MPC) [133], [157]. The fluid is represented with N point particles, each of which is imparted with mass m_i and velocity $\boldsymbol{u}_i$ at position $\boldsymbol{r}_i$, $i = 1, 2, \ldots, N$ (Figure 1.12*A*). MPC consists of streaming and collision steps, and particles interact only in the latter step. In the streaming step, the positions of the particles are updated by $\boldsymbol{r}_i(t+\Delta t) = \boldsymbol{r}_i(t)+\boldsymbol{u}_i\Delta t$. In the collision step, the particles are sorted into collision cells of side length a. Particle velocities within the jth cell are updated by $\boldsymbol{u}_i(t+\Delta t) = {}^c\boldsymbol{u}_i(t)+\boldsymbol{R}(\beta)(\boldsymbol{u}_i(t)-{}^c\boldsymbol{u}_i(t))$, where the center-of-mass velocity of the jth cell is specified by ${}^c\boldsymbol{u}_i(t) = \Sigma m_i\boldsymbol{u}_i(t)/\Sigma m_i$, and the rotation matrix $\boldsymbol{R}$ randomly rotates about a fixed

axis by an angle β or $-\beta$ with the same probability. The collision cell is randomly shifted to ensure Galilean invariance [158]. Parameters such as the time step Δt and collision cell size a need to be carefully chosen [159]. The flagellum is represented by one or more filaments, each of which consists of a series of particles linked by springs. A particle is connected to its neighbor particles on the other filaments if there is more than one filament. Here, we consider a flagellum consisting of one filament and beating in the $\boldsymbol{e}_1 - \boldsymbol{e}_2$ plane. The flagellar shape is governed by the energy formulation,

$$E = E_\mathrm{e} + E_\mathrm{b}, \tag{1.18}$$

where

$$E_\mathrm{e} = \frac{k_1}{2} \int_0^L \left(\left| \frac{\partial \boldsymbol{r}}{\partial s} \right| - 1 \right)^2 \mathrm{d}s,$$
$$E_\mathrm{b} = \frac{k_2}{2} \int_0^L \left[\left(\frac{\partial \boldsymbol{r}}{\partial s} \times \frac{\partial^2 \boldsymbol{r}}{\partial s^2} \right) \cdot \boldsymbol{e}_3 - c(s,t) \right]^2 \mathrm{d}s,$$

where s is the arc length of the flagellum, k_1 and k_2 are stiffness coefficients, and $\boldsymbol{e}_3 = \boldsymbol{e}_1 \times \boldsymbol{e}_2$. Here, E_e represents the tensile energy that keeps the flagellum almost inextensible, and E_b is the bending energy that actuates the bending of the flagellum toward a preferred curvature $c(s,t)$. The preferred curvature could take any reasonable form and is usually specified by a sine wave,

$$c(s,t) = c_0 \sin(ks - \omega t + \phi_0), \tag{1.19}$$

where phase ϕ_0 is a constant, and wavenumber k and frequency ω are defined in the same way as in Equation (1.1). The value of c_0 is a constant but differs across existing studies [73], [136], [157], [160]–[162]. The sperm head is often modeled as a circle (in 2D) or sphere (in 3D) with particles connected by springs [133], [157]. To avoid nearby spermatozoa from being overlapped, repulsive steric forces are applied when the distance between the spermatozoa is smaller than a threshold. As the realistic repulsion remains unknown, the formulation of the steric forces varies between existing studies [69], [133], [157], [160].

Instead of simulating the fluid with multiparticle collision, some hydrodynamic models calculate hydrodynamic forces using RFT ([126], [133], [136]), SBT [162], or RSM [73], [134]. In these hydrodynamic models, each flagellum is also modeled by Equation (1.18) or similar governing equations

such as the Euler–Bernoulli rod [162] or the Kirchhoff rod [136], while the sperm head is ignored (Figure 1.12*B* and *C*). The actuation of a flagellum also obeys Equation (1.19) or similar ones [136]. As each flagellum is a self-propelled microswimmer, its translational velocity, $\boldsymbol{U}$, and angular velocity, $\boldsymbol{\Omega}$, can be determined by its force-balance condition,

$$\boldsymbol{g}_{\mathrm{h}} + \boldsymbol{g}_{\mathrm{e}} + \boldsymbol{g}_{\mathrm{b}} = \boldsymbol{0}, \tag{1.20}$$

where the hydrodynamic force on the flagellum $\boldsymbol{g}_{\mathrm{h}} = -\boldsymbol{f}$, the elastic force $\boldsymbol{g}_{\mathrm{e}} = \mathrm{d}E_{\mathrm{e}}/\mathrm{d}\boldsymbol{r}$, and the bending force $\boldsymbol{g}_{\mathrm{b}} = \mathrm{d}E_{\mathrm{b}}/\mathrm{d}\boldsymbol{r}$.

Numerical results show that nearby swimming spermatozoa may achieve in-phase synchronization and attract each other to form clusters (Figure 1.12*A*) [157], [163], which were experimentally observed [52], [154]. The cluster size depends on the sperm density and the distribution of beat frequencies.

As for two nearby swimming sperm cells, their hydrodynamic interactions significantly influence their swimming trajectories and induce hydrodynamic attraction or repulsion between them, regardless of whether in a 2D ([162]) or 3D model ([73]), as shown in (Figure 1.12*B* and *C*). The hydrodynamic interactions are subject to the configuration of spermatozoa (i.e. the relative position and orientation of the two spermatozoa) and flagellar waveforms. Certain configurations would give rise to in-phase flagellar synchronization [162], or higher swimming speed/efficiency than solitary sperm cells [125], [162]. Another interesting phenomenon caused by the hydrodynamic interaction between spermatozoa is that spermatozoa with planar flagellar waveforms can also locomote in the 3D space [73], [125], [136].

1.2.2 Attached Spermatozoa

Sperm bundling/pairing is a cooperative behavior, which is thought to be a consequence of evolutionary selective pressures and can enhance their swimming speed to gain potential advantages in competence [14], [155], [165]–[167], albeit some counterexamples have also been experimentally observed [168], [169]. Bovine spermatozoa are more often attached to the heads rather than the flagella. The attachment between the heads probably involves proteins on sperm plasma membranes [170], but the details of the attachment and how the mechanical interactions between the heads remain

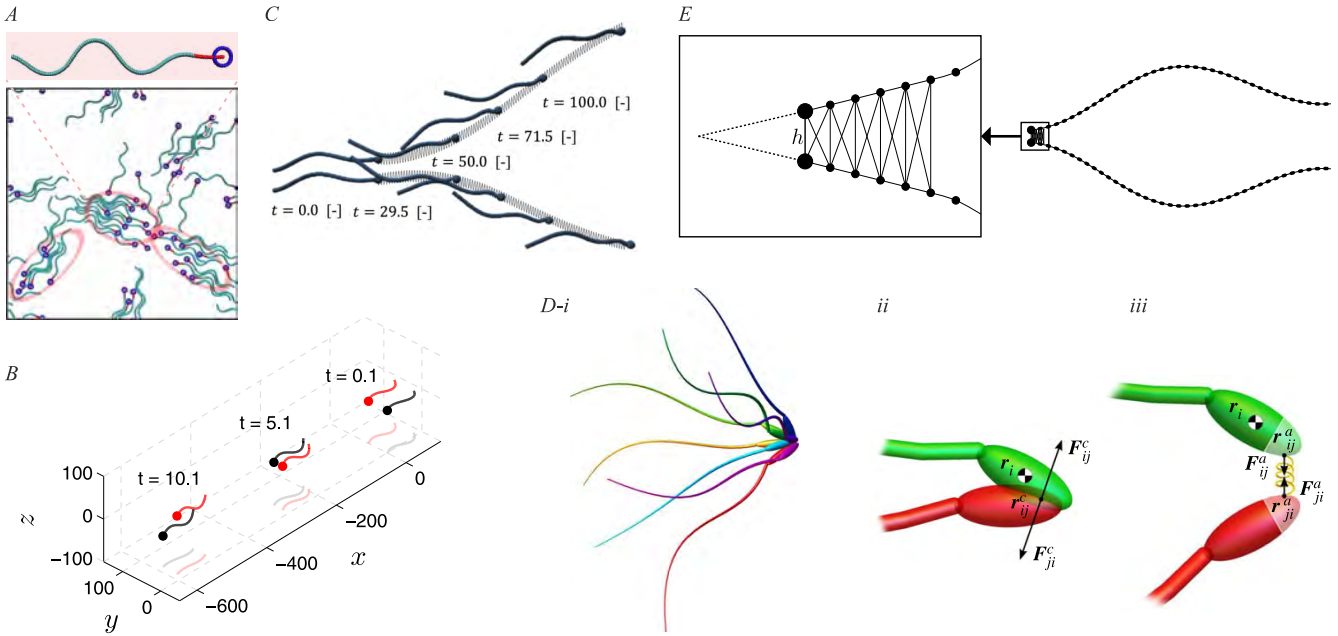

Figure 1.12: (A) Spermatozoa are modeled by MPC and are found to form clusters. (B) Two nearby but separate spermatozoa interact with each other via hydrodynamic forces. (C) Two side-by-side spermatozoa repel each other. (D) Spermatozoa are attached at the head (i). The head-head interactions are represented by steric (ii) and adhesive forces (iii). (E) Paired spermatozoa are modeled with two filaments connected by springs at the front part. Panel (A) is reproduced from reference [157] with permission, American Physical Society. Panel (B) is reproduced from reference [73] with permission, Elsevier. Panel (C) is adapted from reference [162] with permission, AIP Publishing. Panel (D) is adapted from reference [164] with permission, the Royal Society. Panel (E) is adapted from reference [74] with permission, ISU ReD.

largely uninvestigated. A recent 2D simple mechanical model [171] and a 3D persistent random walker model [164] represent the mechanical interaction between the ith and jth sperm heads with a pair of adhesive forces, $\boldsymbol{F}_{ij}^{a}$, and a pair of steric forces, $\boldsymbol{F}_{ij}^{c}$, as illustrated in Figure 1.12*D*. The adhesive forces ensure the head-head attachment, while the steric forces prevent the heads from totally overlapping. The two models showed the trajectory of the sperm bundle is a result of the bundle size, head geometry, and the adhesive region on the heads. An optimal bundle size exists, which induces the fastest traveling speed. Compared with individual sperm cells, sperm bundles have a slower instantaneous swimming speed but a faster net swimming speed due to the reduced directional fluctuation by the tightly attached heads.

Fauci and Peskin developed a hydrodynamic model for aquatic animal locomotion [160], which has been extended for paired sperm cells [74], [125]. In the extended model, the heads are ignored again and represented by several points connected by springs, as shown in Figure 1.12*E*. The numerical study of Cripe et al. indicates that the swimming speed, power, and efficiency are highly dependent on the angle between the heads and the phase lag between the flagella [74]. Enhanced swimming speed and efficiency only happen in sperm pairs with out-of-phase flagellar waves rather than in-phase flagellar waves. However, Woolley et al. experimentally observed that in-phase flagellar synchronization of paired sperm cells led to higher swimming speed than individual sperm cells [14].

We emphasize that the role of mechanical head-head attachment in sperm swimming is salient. Compared with two detached spermatozoa, paired spermatozoa cannot be regarded as the former with a closer distance, considering the experimental and numerical observations of the significant enhancement in swimming speed and efficiency than individual spermatozoa or two detached spermatozoa [14], [125].

1.3 Research Gaps and Objectives

Spermatozoa show spectacular swimming behaviors and have been appealing to researchers. A large number of studies conducted during the past decades have revealed an increasingly clear picture of sperm swimming behaviors. Nonetheless, many intriguing aspects of sperm swimming behaviors remain not fully understood, particularly the cooperative behavior that

sperm cells assemble into bundles/pairs. These research gaps, together with their potential inspiration for the development of biomedical technologies and my curiosity about the cooperative behavior of spermatozoa, motivate my exploration of the dynamics of sperm pairs in this thesis. The research gaps and research questions (**RQs**) are stated below. The first research question is

RQ. 1

How does the sperm pairing influence sperm swimming behaviors?

To answer **RQ. 1**, one potential approach is to statistically compare the swimming behaviors of individual sperm cells and sperm pairs. Nevertheless, a large quantity of samples is required to reveal the details of the impacts of sperm pairing on sperm swimming behaviors. The data volume is too vast for manual detection and tracking of sperm head position, orientation, and flagellar shapes. Although algorithms for automatically tracking flagellar shapes of individual sperm cells have been developed in recent years [80], [172]–[175], no reliable algorithms for tracking sperm bundles/pairs have been reported, because for sperm bundles/pairs, the flagella overlap each other frequently, and the heads are stacked, disrupting the stable image features on which the algorithms are based. The lack of algorithms makes this statistical approach less feasible.

We adopt the second approach: experimentally comparing the swimming behavior of sperm cells before and after they assemble into sperm pairs. This approach requires a much smaller sample size. Notwithstanding, we still face a challenge that approximately 0.1–3% of bovine spermatozoa *in vitro* are observed to assemble into bundles. After conducting many experiments, we encountered four sperm cells assembling into two sperm pairs, as presented in **Chapter 2**. In our experiments, we measure the flagellar waveforms and characterize them with four time-dependent wave variables: mean flagellar curvature K_0, bending amplitude A_0, wavelength λ, and beat frequency ω. These wave variables are mathematically defined in Equation (1.3) in this chapter. The wave variables and swimming speeds reflect the impacts of sperm pairing on their swimming behaviors. Moreover, theoretical models are used to explore the dynamic interactions between sperm cells.

Individual sperm cells have been investigated extensively, while few

studies on the kinetics of attached spermatozoa have been reported. The few studies focused on the stable states of sperm cells, i.e., separate sperm cells or attached sperm cells with regular flagellar beats. The investigation into the transition between the two states is missing. Thus, the second research question is

RQ. 2

How do the dynamics of sperm cells evolve during the transition between the states of being separate and attached?

RQ. 2 is a naturally occurring question after the second approach to answering **RQ. 1** has been adopted. To answer **RQ. 2**, we record the whole course of the transition between the states and characterize the sperm dynamics with the wave variables (K_0, A_0, λ, and ω) and swimming speed. The angle between the heads of a sperm pair is another significant quantity, which represents the rotational dynamics of sperm cells during the transition. These time-varying variables across the whole transition course are presented in **Chapter 2**.

As the "propeller" of spermatozoa, the flagellum plays a salient role in the swimming behavior of solitary spermatozoa (as reviewed in Section 1.1) and a system of multiple separate spermatozoa (as reviewed in Section 1.2.1). But, what about paired sperm cells?

RQ. 3

How do flagellar beat patterns impact the swimming behavior of sperm pairs?

Previous studies primarily concentrated on comparing the swimming speeds of sperm bundles/pairs with those of individual sperm cells [155], [165]–[169]. One experimental study showed that the in-phase flagellar synchronization increases the flagellar beat frequency and swimming speed [14]. One numerical study showed that the flagellar phase lag $\Delta\phi$ significantly influences the swimming performances of sperm pairs [74]. Further understanding of the role of flagellar beat patterns in swimming performances is lacking. Can we answer **RQ. 3** with experiments alone? The answer is no, as it is very challenging to control the beating phase lag be-

tween the flagella of a sperm pair in experiments. The difficulty would be higher considering the low probability of the occurring of sperm pairing. Therefore, simulations seem indispensable for answering **RQ. 3**. Even though the numerical study of Cripe et al. has uncovered some important underlying physics of paired sperm cells, their 2D model excluded sperm heads, ignored the radius of flagella, and represented flagellar waves with sinusoidal waves [74]. These simplifications, particularly the exclusion of heads, skip the significant impacts of the mechanical coupling due to the head-head attachment on the locomotion of sperm pairs [14], [164], [171], which raises the fourth research question:

RQ. 4

What role does the head-head coupling have in sperm swimming performances?

RQ. 4 has not been answered well by previous studies. As reviewed in Section 1.2.2, the models of Fisher et al. and Pearce et al. revealed the prominent impacts of head-head coupling on the locomotion of sperm bundles, but ignored hydrodynamic forces and represented flagella with stochastic noise [164], [171]. Woolley et al. primarily focused on in-phase flagellar synchronization [14]. Regarding **RQ. 4**, due to experimental challenges, the experimental observations by Woolley et al. only provided us with a finding that the rigid head-head attachment leads to in-phase flagellar synchronization. **RQs. 3** and **4** are integrated, posing a research challenge.

To answer **RQs. 3** and **4**, 3D models in **Chapter 4** are developed, which incorporate sperm geometries, hydrodynamic interactions between sperm cells, and mechanical interactions between sperm heads. In the models, flagellar wave patterns are prescribed from experimental measurements. The experimentally observed flagellar kinematics are the result of internal and external disturbances in the flagellar beating and the elasticity of flagella, which are intrinsically incorporated into our models.

The knowledge of head-head attachment is currently insufficient to account for its formation, and the mechanical head-head coupling due to the attachment remains elusive. Therefore, in **Chapter 4**, we incorporate two potential cases of head-head coupling and investigate their influence on sperm swimming.

1.4 Research Framework and Scientific Output

All the research studies that constitute this doctoral thesis have been supported by funds from the European Research Council (ERC) under the European Union's Horizon 2020 Research and Innovation programme under grant 866494 project-MAESTRO, and financial support from the China Scholarship Council (No. 202006290017).

The studies presented in this doctoral thesis are adapted from the following peer-reviewed journal articles. No changes to the technical contents have been made.

1. **Kaixuan Zhang**, Anke Klingner, Yohan Le Gars, Sarthak Misra, Veronika Magdanz, and Islam S.M. Khalil, "*Locomotion of bovine spermatozoa during the transition from individual cells to bundles*", Proceedings of the National Academy of Sciences, vol. 120, no. 3, p. e2211911120, 2023.

2. **Kaixuan Zhang**, Aaron Lewis, Anke Klingner, Veronika Magdanz, Sarthak Misra, and Islam S.M. Khalil "*Locomotion of paired spermatozoa during flagellar synchronisation*", Journal of Fluid Mechanics, in press, January 2025.

2

Locomotion of Bovine Spermatozoa during the Transition from Individual Cells to Bundles

Note: *This chapter is adapted from the article "Locomotion of bovine spermatozoa during the transition from individual cells to bundles" by* ***Kaixuan Zhang****, Anke Klingner, Yohan Le Gars, Sarthak Misra, Veronika Magdanz, and Islam S.M. Khalil, published in "Proceedings of the National Academy of Sciences", vol. 120, no. 3, p. e2211911120, 2023.*

2.1 Significance

Evolutionary selective pressures drive spermatozoa to assemble into bundles for increased fertilizing ability. To understand this type of collective behavior of spermatozoa, we investigate the underlying mechanisms that make spermatozoa form bundles. Here we explore the dynamic processes during the bundle formation by characterizing the cell-cell interactions in three consecutive phases: far field–locking, rotational-oscillation, and steady-swimming phase. During these phases, the interactions are found to regulate flagellar beat and lead to three dynamic behaviors: hydrodynamic attraction/repulsion, alignment, and in-phase synchronization, whereby sperm cells can obtain enhanced swimming speed. Our study not only reveals the efficient collective locomotion of spermatozoa at low Reynolds numbers but also inspires the design of adaptive and powerful soft microrobots.

2.2 Abstract

Various locomotion strategies employed by microorganisms are observed in complex biological environments. Spermatozoa assemble into bundles to improve their swimming efficiency compared to individual cells. However, the dynamic mechanisms for the formation of sperm bundles have not been fully characterized. In this study, we numerically and experimentally investigate the locomotion of spermatozoa during the transition from individual cells to bundles of two cells. Three consecutive dynamic behaviors are found across the course of the transition: hydrodynamic attraction/repulsion, alignment, and in-phase synchronization. The hydrodynamic attraction/repulsion depends on the relative orientation and distance between spermatozoa as well as their flagellar wave patterns and phase shift. Once the heads are attached, we find a stable equilibrium of the rotational hydrodynamics resulting in the alignment of the heads. The in-phase synchronization results from the combined influence of hydrodynamic and mechanical cell-cell interactions. Additionally, we find that the flagellar beat is regulated by the interactions during the bundle formation, whereby spermatozoa can synchronize their beats to enhance their swimming speed.

2.3 Introduction

Collective locomotion emerges in multiscale biological systems ranging from cilia/flagella arrays [98], bacterial colonies [176], and insect swarms [177] to animal herds [152]. These systems show interesting ordering phenomena [152]. For instance, at the microscale, biological cilia/flagella arrays can spontaneously exhibit metachronal waves, resulting in enhanced fluid transport [178], [179]. Facilitated by the collective locomotion of their cilia/flagella, some unicellular organisms exhibit high efficiency in spreading [176], feeding [180], or swimming [98]. Collective locomotion also emerges in spermatozoa driven by flagella. In some higher organisms (e.g., bulls [14], rodents [155], [166], and insects [181]), spermatozoa are found to assemble into bundles. The assembly is an efficient locomotion strategy at low Reynolds number, which has been numerically [74], [125], [162], [164], [171] and experimentally [14], [155], [166] demonstrated to increase the swimming speed of spermatozoa, whereby their fertilizing ability is favored

[166], [167].

The swimming speed of sperm bundles comprising multiple cells results from complex cell-cell interactions. A mechanical model of sperm bundles suggests that the swimming speed of sperm bundles is subject to the bundle size and there exists an optimal sperm bundle size giving rise to a maximum rectilinear speed [171]. In addition, the performance of sperm bundles is significantly affected by the geometry of sperm heads, the structure of the adhesive region of the heads, and the angle between the heads [74], [164].

However, as the minimal model of collective locomotion of sperm cells, the system of two spermatozoa already shows complex interactions. The interactions are found to cause in-phase flagellar synchronization [14], [157] and attraction/repulsion between two sperm cells [136], [157], [162]. The emergence of flagellar in-phase synchronization is attributed to either only hydrodynamic interactions [136], [162], [182] or dominantly mechanical interactions [14], [81]. The cell-cell attraction/repulsion as well as the swimming speeds of two sperm cells depend on their configuration, separation distance, and phase shift of flagellar waves [136], [162], which is consistent with the prediction of a numerical model of two three-sphere swimmers [108].

Although the collective locomotion of sperm cells has been preliminarily disclosed [14], [136], [157], [162], [164], [171], it is still not fully understood, especially the dynamic processes during the transition from individual cells to bundles. A recent study explains that the bundling of sperm cells is a result of hydrodynamic and adhesive interactions which occur frequently during prolonged incubation times. Mostly pairs of two motile sperm cells are formed [15]. There are only a few studies of bundle formation for two key reasons. First, the momentary formation of sperm bundles occurs randomly, limiting our ability to observe and measure their motion characteristics. Second, the locomotion of spermatozoa during bundle formation is influenced by time-varying cell-cell interactions. The interactions and bundle formation are likely to be affected by intrinsic and external factors. The intrinsic factors that characterize the locomotion of sperm cells are represented by the time-dependent wave variables (i.e. the mean flagellar curvature K_0, bending amplitude A_0, wavelength λ, and angular frequency ω) of the actively propagating waves along flagella, the phase shift of the flagellar waves $\Delta\phi$, and the angle between the heads $\Delta\theta$. The external factors denote the parameters that can influence the bundle formation through

the environment, such as the geometry of the surrounding environment [58], chemoattractants [43], and the viscosity of fluids [52].

In this study, we investigate the dynamic formation of bundles of two sperm cells with regard to the intrinsic factors and the external factor, fluid viscosity μ. We divide the formation into three phases: far field–locking (FFL) phase, rotational-oscillation (RO) phase, and steady-swimming (SS) phase. These phases are experimentally observed during the bundle formation. We numerically investigate the hydrodynamic cell-cell interactions of the spermatozoa during the three consecutive phases. Further, time-dependent wave variables are measured to characterize the flagellar wave pattern across the whole course of the transition.

2.4 Results

2.4.1 Formation of Sperm Bundles

Spermatozoa display a variety of three-dimensional (3D) swimming patterns [64], [65]. However, they tend to gather near the bottom surface and hence exhibit flagellar beats that consist mostly of planar waves due to hydrodynamic cell-surface interactions [78], [135]. Therefore, we characterize the flagellar waves in the plane where sperm cells swim, neglecting the out-of-plane component (Figure 2.1*A*). The time-varying flagellar wave pattern of the ith sperm cell is characterized in terms of the position vector of the centerline of the flagellum ${}^{i}\boldsymbol{r}(s_i, t)$ in the laboratory frame, and in terms of the wave variables in the co-moving frame spanned by the orthonormal unit vectors ${}^{i}\boldsymbol{e}_1$ and ${}^{i}\boldsymbol{e}_2$ [75], [80] (Appendix 2.6.4). Here, ${}^{i}\boldsymbol{e}_1$ and ${}^{i}\boldsymbol{e}_2$ are the unit vectors oriented along the long axis and short axis of the projection of the head of the ith sperm cell in the swimming plane, respectively (Figure 2.1*B*).

Flagellar beats are governed by the balance between the internal force generated by many active elements (e.g., dyneins) and passive elastic elements (e.g., nexins) and the external forces on the flagellum [80], [183]. The external forces can result from either the fluid flow induced by other cells or the mechanical coupling when the cells are in physical contact. Therefore, the flagellar beat as well as the movement of cells is regulated by hydrodynamic or mechanical cell-cell interactions during the bundle formation, which consists of three phases. In the FFL phase, two sperm cells approach

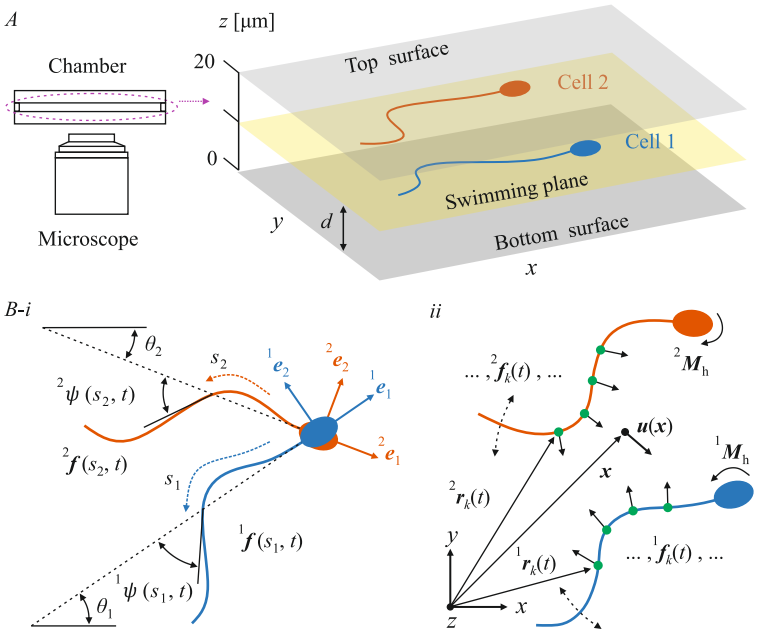

Figure 2.1: Locomotion and hydrodynamic interactions of sperm cells are modeled. (*A*) Sperm suspension is pipetted in a 20 µm high chamber and recorded with an inverted microscope. Near the bottom surface of the chamber, the sperm cells exhibit primarily planar flagellar beats in the swimming plane with distance d from the bottom surface. (*B*, *i*) The locomotion of sperm cells is characterized in the swimming plane. The flagellar pattern at a time t can be characterized by the tangent angle ψ along the flagellum in the co-moving frame spanned by orthonormal vector $\boldsymbol{e}_1$ and $\boldsymbol{e}_2$. The orientation θ_1 is positive, and θ_2 is negative. (*B*, *ii*) Each sperm cell is discretized with N points. The hydrodynamic force ${}^i\boldsymbol{f}_k$ on the kth points along the ith flagellum and fluid flow $\boldsymbol{u}(\boldsymbol{x})$ at the point $\boldsymbol{x}$ are contributed by every regularized Stokeslets on the surface of the sperm cells. Here, the force ${}^i\boldsymbol{f}_k$ is the discretization of ${}^i\boldsymbol{f}(s_i, t)$. Further, the rotation of ith head leads to a hydrodynamic torque in the swimming plane ${}^i\boldsymbol{M}_\mathrm{h}$. The position vector ${}^i\boldsymbol{r}_\mathrm{k}$ is used to determine the time-varying flagellar waveform. Note that the force $\boldsymbol{f}_k$, torque $\boldsymbol{M}_\mathrm{h}$, velocity of the fluid $\boldsymbol{u}$, and position vector $\boldsymbol{r}_k$ and $\boldsymbol{x}$ are vectors in the three-dimensional space.

each other until their heads come into contact. The hydrodynamic attraction between the cells is likely to facilitate the approach. Once the heads are attached, the mechanical interaction between the heads constrains the

relative translational motion but allows the ith cell to rotate about the axis ${}^{ij}\boldsymbol{e} = {}^{i}\boldsymbol{e}_1 \times {}^{j}\boldsymbol{e}_1$, $(i+j=3)$ (Figure 2.2*A*, *iii* and *iv* and *B*, *iii* to *v*). During this RO phase, the interactions break the regular flagellar beat and result in the alignment of the heads. Finally, under the combined influence of the hydrodynamic and mechanical cell-cell interactions, the sperm bundles resume regular flagellar beats during the SS phase (Figure 2.2*A*, *v* and *vi* and *B*, *vi*).

2.4.2 Flow Fields during Far Field–Locking Phase

From a dynamic perspective, the only way spermatozoa interact with neighbor cells is through the induced flow field. To elucidate the influence of the intrinsic and external factors on the locomotion of sperm cells, we construct a 3D fluid model to calculate the hydrodynamic forces on the cells and the flow field by solving the Stokes equations using regularized Stokeslets method (Appendix 2.6.5). Previous studies show that a large proportion of the sperm cells near the bottom are approximately between 0.05 and 0.2 times of their body length from the bottom surface [77], [133], [184]. With a body length of 60 µm of bovine sperm, we can assume that they swim approximately between 3 and 12 µm from the bottom surface. In our 3D model, the two sperm cells swim in the same plane with distance d from the bottom surface (Figures 2.1*A* and 2.3). A series of calculations for hydrodynamic force $\langle \Delta \boldsymbol{F}_y \rangle$ on the sperm cells are performed at different distances d of 3, 4, 10 µm as well as the far-field condition (Figures 2.A1, 2.4 and 2.5). The compliance of the flexible flagella is also considered in the calculation by reconstructing the flagellar wave patterns of the cells with the time-averaged wave variables over the far field–locking phase measured in the experiments (see Table 2.1).

In biological fluids, the orientation of sperm cells and propagating waves along the flagella vary among cells. Our calculation shows that both the relative orientation of two sperm cells $\Delta\theta$ and the phase shift between the flagellar wave $\Delta\phi$ affect the flow field as well as the associated hydrodynamic forces on the cells (Figures 2.3 to 2.5). The time-averaged flow field in the swimming plane is shown in Figure 2.3. Here, the relative orientation $\Delta\theta$ is denoted by the difference between the angles $\Delta\theta = \theta_1 - \theta_2$, as illustrated in Figure 2.1*B*. The phase shift $\Delta\phi$ is denoted by the difference between the first Fourier modes of the tangent angle $\psi(s_i, t)$ of the

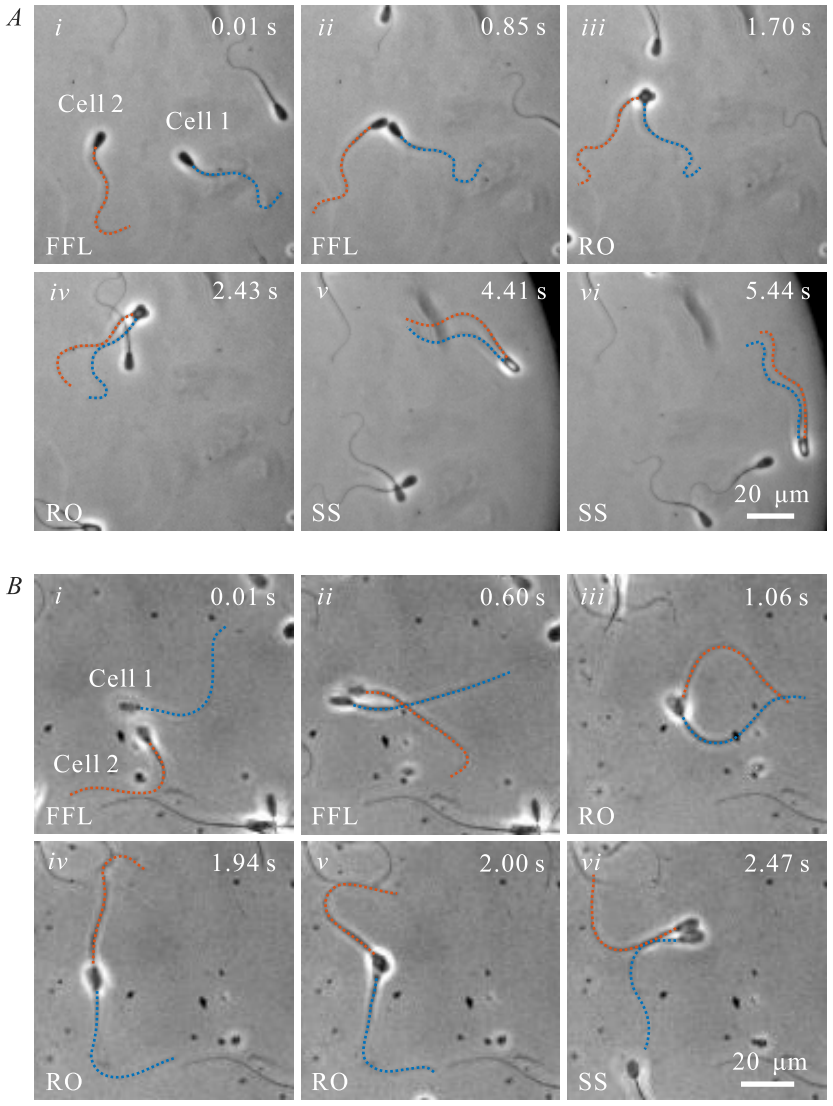

Figure 2.2: The transition from individual cells to a bundle of two cells was observed in low- and high-viscosity media. (*A*) In the relatively high-viscosity medium of 15 mPas, the transition course was divided into far field–locking (FFL) phase (*i* and *ii*), rotational-oscillation (RO) phase (*iii* and *iv*), and the steady-swimming (SS) phase (*v* and *vi*). (*B*) In the relatively low-viscosity medium of 1.2 mPas, two sperm cells were observed to transition through the FFL phase (*i* and *ii*), RO phase (*iii* to *v*), and SS phase (*vi*).

Figure 2.3: Hydrodynamic interactions between spermatozoa with distance 4 µm from the bottom surface. Seven representative time-averaged flow fields in the swimming plane induced by the sperm cells over one beat cycle T in the medium with a viscosity μ of 15 mPas. (A) The cells are in the swimming plane 4 µm from the bottom surface. The flagellar wave shift $\Delta\phi$ is zero, and the angle between the heads $\Delta\theta$ equals 0 (B), $\pi/6$ (C), $\pi/3$ (D), $\pi/2$ (E), $2\pi/3$ (F), $5\pi/6$ (G), and π (H), respectively.

Table 2.1: Experimental results of time-averaged wave variables. The wave variables here are represented as mean±SD, and averaged over respective phases. In the low-viscosity medium of μ=1.2 mPas, the averaged angular frequency $\langle\omega_2\rangle$ excludes the 8th, 9th and 10th beat cycles, which correspond to the period when cell 1 drastically decelerates its beat for unknown reasons. In the high-viscosity experiment of μ=15 mPas, the flagellar waves of the cells are synchronized during the steady-swimming (SS) phase, hence both the cells have 11 beat cycles. However, because the sperm cells regulate their beat during the formation of sperm bundles, the number of beat cycles analyzed for cell 1 (N_1) and cell 2 (N_2) is different even in the same phases. The values of N_1 and N_2 at each phase are the number of beat cycles for cell 1 and cell 2 during the same phase, respectively.

μ [mPas]	Phase	$\langle {}^1K_0\rangle$ [rad/mm]	$\langle {}^2K_0\rangle$ [rad/mm]	$\langle {}^1A_0\rangle$ [rad/mm]	$\langle {}^2A_0\rangle$ [rad/mm]	N_1 [cycles]	N_2 [cycles]
15	FFL	5.3 ± 1.0	24.8 ± 2.1	9.8 ± 1.2	11.2 ± 1.6	5	7
	RO	6.6 ± 2.1	22.2 ± 1.7	9.7 ± 1.7	8.8 ± 1.4	24	29
	SS	7.1 ± 1.1	7.1 ± 1.0	7.6 ± 1.1	7.3 ± 1.3	11	11
1.2	FFL	24.6 ± 1.4	23.0 ± 1.7	11.4 ± 1.2	12.0 ± 1.2	9	9
	RO	24.8 ± 1.5	23.7 ± 2.0	10.3 ± 1.4	9.7 ± 1.3	27	22
	SS	25.1 ± 1.3	23.9 ± 1.5	10.1 ± 1.3	9.2 ± 1.4	7	6
μ [mPas]	Phase	$\langle\lambda_1\rangle$ [µm]	$\langle\lambda_2\rangle$ [µm]	$\langle\omega_1\rangle$ [rad/s]	$\langle\omega_2\rangle$ [rad/s]	N_1 [cycles]	N_2 [cycles]
15	FFL	45.6 ± 3.5	36.8 ± 2.9	37.3 ± 2.5	55.6 ± 7.4	5	7
	RO	46.7 ± 3.8	42.5 ± 4.0	42.6 ± 6.0	52.8 ± 8.8	24	29
	SS	49.2 ± 2.6	47.3 ± 2.7	51.1 ± 6.1	50.0 ± 7.2	11	11
1.2	FFL	59.6 ± 3.1	57.5 ± 3.3	115.3 ± 4.7	89.4 ± 7.4	9	9
	RO	60.5 ± 5.2	64.2 ± 4.2	109.5 ± 18.0	86.2 ± 11.6	27	22
	SS	60.1 ± 3.4	65.4 ± 3.2	106.6 ± 9.8	86.5 ± 10.7	7	6

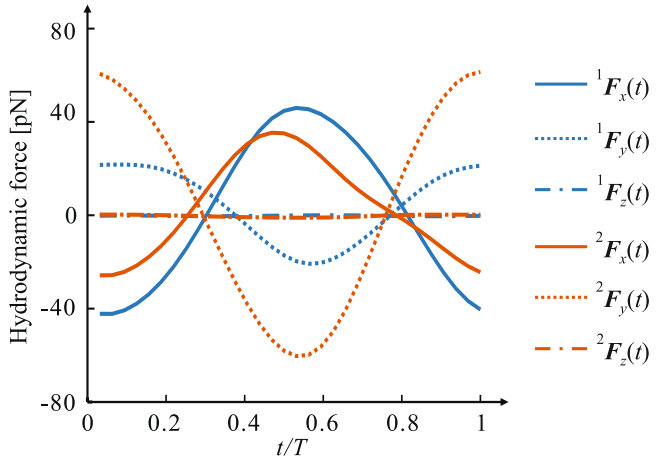

Figure 2.4: The hydrodynamic forces for the spermatozoa in Figure 2.3 with $\Delta\phi = \pi/3$ and $\Delta\theta = \pi/2$ are time-varying during the same beat cycle T. Here, ${}^i\boldsymbol{F}_x(t)$, ${}^i\boldsymbol{F}_y(t)$ and ${}^i\boldsymbol{F}_z(t)$ are the hydrodynamic force on the ith sperm cell along the x-, y-, and z-axis, respectively. The curves for ${}^1\boldsymbol{F}_z(t)$ and ${}^2\boldsymbol{F}_z(t)$ are overlapped as their differences are very small.

centerline of the two flagella (Appendix 2.6.4). Further, the hydrodynamic forces on the cells are time-varying over one beat cycle T. For example, for the case where $\Delta\theta = \pi/3$ and $\Delta\phi = \pi/2$, the hydrodynamic force along the y-axis ${}^1\boldsymbol{F}_y(t)$ on cell 1 propels it to move along the positive y-axis ($0 < t/T < 0.4\,s$), then negative y-axis ($0.4\,s \leq t/T < 0.8\,s$), and positive y-axis ($0.8\,s \leq t/T < 1\,s$) again during one beat cycle, as shown in Figure 2.4. Over one beat cycle, the time-averaged hydrodynamic force on cell 1 along the y-axis $\langle {}^1\boldsymbol{F}_y \rangle$ is positive (Appendix 2.6.5), which indicates that the net displacement of cell 1 along the y-axis in the laboratory frame is positive. Similarly, cell 2 has a smaller positive displacement along the y-axis over the same beat cycle. Therefore, the distance between cells decreases by the attractive flow field.

The force difference between the cells $\langle \Delta\boldsymbol{F}_y \rangle = \langle {}^2\boldsymbol{F}_y \rangle - \langle {}^1\boldsymbol{F}_y \rangle$ is used to denote the forces that attract (negative values in Figure 2.5) or repel (positive values in Figure 2.5) the cells. For the cells in the high-viscosity medium of $\mu = 15\,\mathrm{mPas}$, the forces $\langle \Delta\boldsymbol{F}_y \rangle$ are attractive only when $\Delta\theta = \pi/3$ or $\pi/2$. For the cells in the low-viscosity medium of $\mu = 1.2\,\mathrm{mPas}$, the forces lead to the cell-cell repulsion only when $\Delta\theta = \pi$.

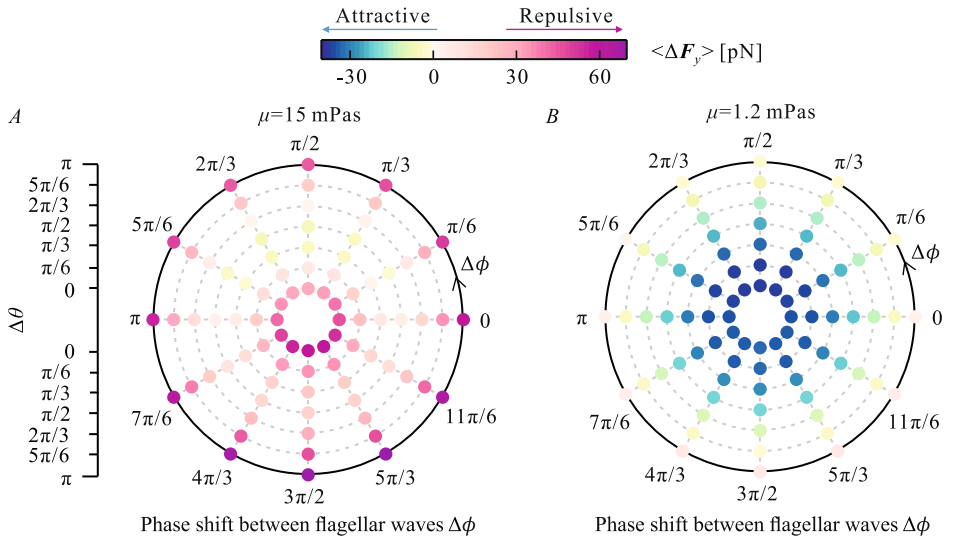

Figure 2.5: The difference between the forces $\langle \Delta \boldsymbol{F}_y \rangle = \langle {}^2\boldsymbol{F}_y \rangle - \langle {}^1\boldsymbol{F}_y \rangle$ characterizes the cell-cell attraction/repulsion and is computed for $\Delta\theta$ (the radial coordinate) in the range of 0 to π and $\Delta\phi$ (the angular coordinate) in the range of 0 to 2π. Each combination of $\Delta\theta$ and $\Delta\phi$ represents a configuration of the two cells. Each dot in the polar scatter charts denotes a value of $\langle \Delta \boldsymbol{F}_y \rangle$ regarding a configuration of the two cells. (A) The force $\langle \Delta \boldsymbol{F}_y \rangle$ for a pair of cells swimming in the high-viscosity medium of $\mu = 15$ mPas is calculated. The maximum repulsive force emerges from the configuration of $\Delta\theta = \pi$ and $\Delta\phi = 3\pi/2$. The waveforms of the spermatozoa in the high-viscosity medium of 15 mPas are reconstructed with the wave variables (i.e. the mean flagellar curvature K_0, bending amplitude A_0, wavelength λ, and angular frequency ω), such that ${}^1K_0 = 5.3$ rad/mm, ${}^1A_0 = 9.8$ rad/mm, $\lambda_1 = 45.6$ µm, $\omega_1 = 45.5$ rad/s, ${}^2K_0 = 24.8$ rad/mm, ${}^2A_0 = 11.2$ rad/mm, $\lambda_2 = 36.8$ µm, and $\omega_2 = 45.5$ rad/s. The values of these wave variables are the averaged values over the far field–locking phase (see Table 2.1). (B) The force $\langle \Delta \boldsymbol{F}_y \rangle$ for a pair of cells swimming in the low-viscosity medium of $\mu = 1.2$ mPas is calculated. The maximum attractive force is induced when the configuration of the cells is $\Delta\theta = 0$ and $\Delta\phi = \pi/2$. In the simulation, the radii and lengths of the flagella are 0.25 µm and 60 µm, respectively. For each cell, the head is modeled as an ellipsoid, whose dimensions are 9 µm (length), 5 µm (width), and 1 µm (height), respectively. The head-to-head distance is 50 µm. The waveforms of the spermatozoa in the low-viscosity medium of 1.2 mPas are reconstructed with the wave variables, such that ${}^1K_0 = 24.6$ rad/mm, ${}^1A_0 = 11.4$ rad/mm, $\lambda_1 = 59.6$ µm, $\omega_1 = 98.2$ rad/s, ${}^2K_0 = -23.0$ rad/mm, ${}^2A_0 = 12.0$ rad/mm, $\lambda_2 = 57.5$ µm, and $\omega_2 = 98.2$ rad/s. The values of these wave variables are the averaged values over the far field–locking phase (see Table 2.1).

The difference results from the distinct flagellar wave patterns. In the high-viscosity medium, both the flagella have a positive mean flagellar curvature, while in the low-viscosity medium, cell 1 and cell 2 have a positive and negative mean flagellar curvature, respectively (Appendix, movies S1 and S2).

Moreover, we find that the fluid flow and hydrodynamic forces are affected by the separation distance between the cells and the viscosity of fluids. Because the sperm cell is a swimmer close to combined time-reversal and parity invariant, the average flow around the cell has a l^{-3} dependence, where l is the distance away from the cell [108]. Consequently, the cells in both viscosities generate increasingly greater attractive/repulsive force $\langle \Delta \boldsymbol{F}_y \rangle$ (dots with darker color in Figure 2.5) with the reduction of $\Delta\theta$ due to the closer distance between the flagella. Further, the fluid viscosity μ affects the time-averaged hydrodynamic force $\langle \Delta \boldsymbol{F}_y \rangle$ in two aspects. First, the hydrodynamic force $\langle \Delta \boldsymbol{F}_y \rangle$ scales linearly with the fluid viscosity μ (see Figure 2.A2). Second, the viscosity regulates the flagellar beat, thereby affecting the hydrodynamic forces [52]. Further, a series of calculation results for hydrodynamic force $\langle \Delta \boldsymbol{F}_y \rangle$ on the sperm cells at different distances from the bottom boundary are qualitatively consistent (Figure 2.A1). The hydrodynamic attractive/repulsive forces between the cells increase at almost every configuration when the cells are closer to the bottom surface. The sperm cells always induce maximum hydrodynamic attractive forces when the phase shift $\Delta\phi = \pi/2$, and maximum hydrodynamic repulsive forces at $\Delta\phi = 3\pi/2$, regardless of the distance sperm from the bottom surface.

2.4.3 Hydrodynamic Torque Balance during Rotational-Oscillation Phase

Besides hydrodynamic forces, sperm cells also experience hydrodynamic torque when their heads are attached and pivot around the axis ${}^{ij}\boldsymbol{e}$. Here, we only focus on the hydrodynamic force/torque in the swimming plane, as the hydrodynamic forces along the z-axis, $\boldsymbol{F}_z$, are very small compared with the forces along the x- and y-axis, $\boldsymbol{F}_x$ and $\boldsymbol{F}_y$ (Figure 2.4). The total torque on the ith cell must be zero and we have

$$ {}^{i}\boldsymbol{M}_{\mathrm{h}}(t) + \int_0^{L_i} {}^{i}\boldsymbol{f}_{xy}(s_i,t) \times {}^{i}\boldsymbol{r}(s_i,t)\mathrm{d}s_i + \kappa \sin(\Delta\theta)\, {}^{ij}\boldsymbol{e} = 0, \tag{2.1} $$

where ${}^{i}\boldsymbol{f}_{xy}(s_i,t)$ is the force along the ith flagellum in the swimming plane. The first and second terms of this equation are the hydrodynamic torque on the head and flagellum of the ith cell, respectively. The hydrodynamic torque in the swimming plane ${}^{i}\boldsymbol{M}_{\mathrm{h}}$ is computed by ${}^{i}\boldsymbol{M}_{\mathrm{h}} = 8\pi ab^2\mu C_1\boldsymbol{\Omega}_i(t)$, where $\boldsymbol{\Omega}_i(t)$ is the angular frequency of the rotating head, C_1 is the geometric coefficient for the rotation, and a and b are the semi-minor axis and semi-major axis of the projection of the head in the swimming plane, respectively [92]. The relative translational motion between the heads is negligible when they are attached, therefore we only consider the relative rotational motion. There exist adhesive/repulsive forces between the heads [164], [185], which are modeled as a linear spring torque with elastic constant κ, as shown in the third term in Equation (2.1). Therefore, the hydrodynamic torque balance on the sperm bundle is given by

$$ {}^{1}\boldsymbol{M}_{\mathrm{h}} - {}^{2}\boldsymbol{M}_{\mathrm{h}} + {}^{1}\boldsymbol{M}_{\mathrm{f}} - {}^{2}\boldsymbol{M}_{\mathrm{f}} + 2\kappa\sin(\Delta\theta)\,{}^{12}\boldsymbol{e} = 0, \tag{2.2} $$

where ${}^{1}\boldsymbol{M}_{\mathrm{f}}$ and ${}^{2}\boldsymbol{M}_{\mathrm{f}}$ are the hydrodynamic torque on the flagellum of cell 1 and cell 2, respectively. The flagellar beat is periodic/quasi-periodic, therefore we model the hydrodynamic torque on the flagellum in the swimming plane $\boldsymbol{M}_{\mathrm{f}}$ with a sinusoidal function $\boldsymbol{M}_{\mathrm{f}} = \boldsymbol{M}_{\mathrm{a}}\sin(\omega t + \phi_0)$, where ϕ_0 is the initial phase. The flagellar beat frequency ω and initial phase ϕ_0 are the results from our experimental measurements. $\boldsymbol{M}_{\mathrm{a}}$ is an averaged hydrodynamic torque on the flagellum derived from the regularized Stokeslets. Equation (2.2) is a first-order nonlinear ordinary differential equation with constant coefficients. The coefficients depend on the characteristics of the fluid, the morphology of the heads, and the head-to-head adhesion.

The solution to Equation (2.2) characterizes the rotational dynamics of the sperm cells, as shown in Figure 2.6. When the angle between the heads $\Delta\theta$ decreases to zero, the heads are aligned. The angle $\Delta\theta$ oscillates owing to the energy transfer between the distributed contractile and elastic elements of the active flagellum. The decaying $\Delta\theta$ results from the energy loss in the viscous medium, the friction between the heads, and the friction between the dynein motors of the flagellum [186].

It is common to observe sperm cells with different types of chirality in biological environments [133], [187]. When a sperm bundle is formed by two cells with the same chirality, the hydrodynamic torques on the cells are in the same direction, leading the angle $\Delta\theta$ to decrease to zero, as predicted by the theory described by Equation (2.2) (Figure 2.6*A*, *i*). When the cells

have opposite chirality, the hydrodynamic torques on the cells are in the opposite direction, leading to a possible scenario that the angle $\Delta\theta$ first increases to π and then declines to zero (Figure 2.6*A*, *ii*). Compared with the high-viscosity medium, the low-viscosity medium leads to a faster alignment of sperm bundles. This is a direct result of the faster beat frequency of sperm cells in the low-viscosity fluid. In contrast to the low-viscosity medium, the high-viscosity medium exerts a stronger suppression on the oscillation amplitude of the angle between the heads $\Delta\theta$ (Figure 2.6*B*). The lower viscosity causes faster alignment of the heads. The smaller amplitude of the oscillation of the angle $\Delta\theta$ results from the smaller oscillation of the heads of individual cells. Further, flagellar propagating waves vary among spermatozoa, therefore a non-zero phase shift is likely to be present between ${}^1\boldsymbol{M}_\mathrm{f}$ and ${}^2\boldsymbol{M}_\mathrm{f}$ during the RO phase. Our calculation shows that the larger phase shift $\Delta\phi$ fails to affect the relaxation time of $\Delta\theta$ but may increase the oscillation amplitude of $\Delta\theta$ (Figure 2.6*C*). Note that in the low-viscosity case, only the stage when $\Delta\theta$ decreases is shown in Figure 2.6*B*, *ii* and *C*, *ii*. The stage when $\Delta\theta$ increases has similar results.

In summary, the agreement between the experimental results and the calculation infers that the rotational dynamics of sperm bundles depend on the coupled hydro-mechanical cell-cell interactions. Our numerical results demonstrate that the heads of two sperm cells eventually align regardless of the initial angle (Figure 2.6*A*), chirality (Figure 2.6*A*), fluid viscosity (Figure 2.6*B*), and phase shift (Figure 2.6*C*). This conclusion is confirmed by our experiments (Figure 2.2) and can be drawn from the hydrodynamic torque balance on the sperm bundle, which predicts that $\Delta\theta = 0$ is the stable equilibrium point.

2.4.4 Thrust and Net Swimming Speed of Sperm Bundles during Steady-Swimming Phase

After spermatozoa form a bundle, their flagellar waveform is likely to be regulated, and thereby the sperm bundle obtains propulsive thrust and swimming speed that may be enhanced, reduced, or averaged. Thus, we calculate the time-averaged thrust of sperm bundle over one beat cycle $\langle \boldsymbol{F}_\mathrm{T} \rangle$ and the net swimming speed v_n for a range of K_0, A_0, and λ (Appendix 2.6.6). The net swimming speed characterizes the effective motion of spermatozoa. It is defined by $v_\mathrm{n} = \Delta S/T$, where T is the period of one flagellar

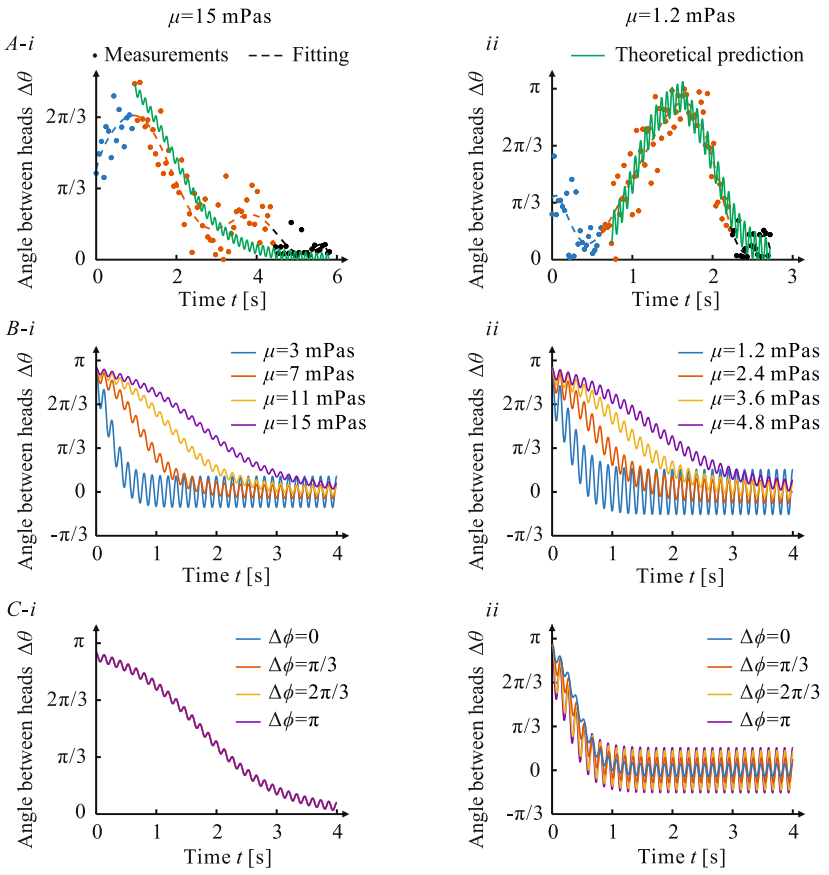

Figure 2.6: Time response of the angle between the heads $\Delta\theta$. (A) The blue, red, and black dots denote the measurements of $\Delta\theta$ during the far field–locking phase, rotational-oscillation phase, and steady-swimming phase, respectively. The calculation (green line) indicates that high viscosity exerts a stronger constraint on the oscillation amplitude of the $\Delta\theta$, which is consistent with the measurements where the norm of the residuals of the fitting is 125 for the high-viscosity case ($\mu = 15\,\mathrm{mPas}$) and 182 for the low-viscosity case ($\mu = 1.2\,\mathrm{mPas}$). The fitting lines (dashed lines) are nine-degree polynomial curves. Notice that only the absolute value of the angle is measured. (B) The time response of $\Delta\theta$ is computed for four representative viscosities of 3, 7, 11, 15 mPas for the high-viscosity case (i) and 1.2, 2.4, 3.6, 4.8 mPas for the low-viscosity case (ii). Here, the phase shift is π. (C) The time response of $\Delta\theta$ is calculated for four representative phase shifts $\Delta\phi$ of 0, $\pi/3$, $2\pi/3$, π for the high-viscosity case (i) and the low-viscosity case (ii). Due to very small differences between the values of $\Delta\theta$ at different $\Delta\phi$, the curves in $(C,\, i)$ are overlapped.

beat cycle, and ΔS is the displacement of the head during one beat cycle.

The calculation reveals that $\langle \boldsymbol{F}_{\mathrm{T}} \rangle$ and v_{n} are a complicated result of the wave variables (Figure 2.7). A sole increase in the amplitude cannot guarantee enhanced net swimming speed. Some abnormal flagellar wave patterns even generate a backward time-averaged propulsive force such that sperm bundles have a negative net displacement along the averaged swimming path (Figure 2.7*A*, *i* and *B*, *i*). In common cases in biological environments (e.g., some K_0-A_0-λ combinations in the range $K_0 < 30\,\mathrm{rad/mm}$, $A_0 < 20\,\mathrm{rad/mm}$, and $\lambda < 100\,\mu\mathrm{m}$), sperm bundles can increase their net swimming speed with a larger flagellar wave amplitude A_0 or wavelength λ, but cannot with reducing mean flagellar curvature K_0 (Figure 2.7*A*, *ii* and *B*, *ii*). For instance, for a sperm bundle with $A_0 = 10\,\mathrm{rad/mm}$, $K_0 = 13.3\,\mathrm{rad/mm}$, and $\lambda = 44.8\,\mu\mathrm{m}$, its net swimming speed v_{n} increases 24% when A_0 increases to $15\,\mathrm{rad/mm}$, 13% when λ increases to $60\,\mu\mathrm{m}$, and only 3% when K_0 decreases to $5\,\mathrm{rad/mm}$, provided A_0, λ, and K_0 are the only varying wave variables, respectively. However, on large time scales, smaller mean flagellar curvature leads to a straighter trajectory and thus a greater rectilinear speed [164].

Further, the flagellar beat frequency ω accelerates when flagellar beats are synchronized [14]. Our calculation shows that the net swimming speed v_{n} or the time-averaged thrust $\langle \boldsymbol{F}_{\mathrm{T}} \rangle$ is linear proportional to the flagellar beat frequency (Figure 2.A3). It is a direct result derived from the relation that the instantaneous swimming speed scales linearly as the beat frequency [97].

Furthermore, in biological environments, sperm bundles are formed with their heads attached (Figure 2.2). The attachment is thought to enable the sperm bundle of two cells to achieve a double bending force and a double elastic force, but experience a less-than-twofold viscous force, whereby its swimming speed is enhanced [14]. The impact of the attachment on the net swimming speed is yet unknown, so we evaluate the impact by simply modifying the friction coefficients with a correction factor C_{f}. The numerical results show that the relation between the net swimming speed and the correction factor is approximately linear proportion (Figure 2.A4).

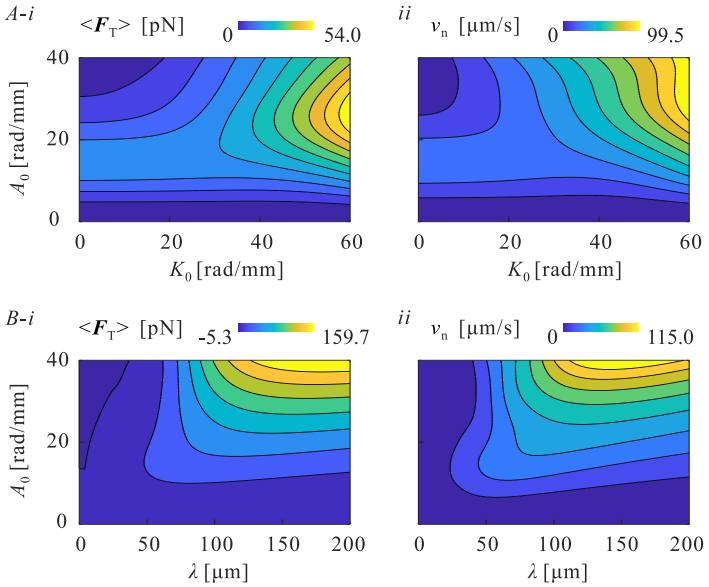

Figure 2.7: The influence of flagellar waveform on the time-averaged propulsive thrust $\langle \boldsymbol{F}_\mathrm{T} \rangle$ and net swimming speed v_n of the sperm bundle. (A) Time-averaged thrust $\langle \boldsymbol{F}_\mathrm{T} \rangle$ (i) and net swimming speed v_n (ii) are computed over the mean flagellar curvature K_0 in the range of 0–60 rad/mm and amplitude rise A_0 of 0–40 rad/mm. Here, the wavelength $\langle \lambda \rangle$ and angular frequency $\langle \omega \rangle$ are the average values over the three phases in the high-viscosity experiment, such that $\langle \lambda \rangle = 44.8 \pm 4.8\,\mu\mathrm{m}$ and $\langle \omega \rangle = 47.2 \pm 8.8\,\mathrm{rad/s}$ (mean ± SD). (B) Time-averaged propulsive thrust $\langle \boldsymbol{F}_\mathrm{T} \rangle$ (i) and net swimming speed v_n (ii) are computed over the wavelength λ in the range of 0–200 µm and amplitude rise A_0 of 0–40 rad/mm. Here, the mean flagellar curvature $\langle K_0 \rangle$ and angular frequency $\langle \omega \rangle$ are the average values over the three phases in the high-viscosity experiment, such that $\langle \lambda \rangle = 13.3 \pm 8.1\,\mathrm{rad/mm}$ and $\langle \omega \rangle = 47.2 \pm 8.8\,\mathrm{rad/s}$ (mean ± SD). A correction factor C_f of 0.8 for the hydrodynamic friction on sperm heads is used to characterize the impact of the head-to-head attachment on the net swimming speed. Note that only the module of the net swimming speed is considered.

2.4.5 Flagellar Beats during the Transition in High-Viscosity Medium

Without varying external forces, freely swimming spermatozoa usually exhibit regular flagellar beats according to the balance of bending forces, elastic forces, and viscous forces [80], [183]. The l^{-2} dependence of the force

dipole suggests that hydrodynamic cell-cell interactions between flagella are non-negligible when the cells are close [92], [188]. In the high-viscosity medium of $\mu = 15\,\mathrm{mPas}$, the time-dependent wave variables seem erratic due to hydrodynamic interactions, but significant changes in the wave variables can be seen from their trends (illustrated by the fitting curves in Figure 2.8), such that the frequency of cell 2 is declining significantly as the cells approach during the FFL phase (Figure 2.8*D*).

After the cells come into contact and adhere to each other, the cell-cell interactions can affect every wave variable significantly. However, the effect of the interactions on the wave variables is not always "equal". For instance, for cell 2 during the time 0.9–1.6 s, its mean flagellar curvature ${}^2K_0$ remains almost invariant, whereas its beat frequency ω_2 increases significantly. It means that only some aspects (e.g., the beat frequency) of the flagellar wave pattern are regulated significantly, rather than every aspect. Further, the effect of the interactions is not always "equal" for the sperm cells. For example, the ${}^1K_0$ increases, whereas the ${}^2K_0$ decreases during the RO phase. The differences in the interactions between the cells may result from the configuration of the sperm bundle where the position of the cells is not identical and interchangeable. An alternative possible cause is that the flagella have a different intrinsic bending stiffness, given the different flagellar wave patterns shown in the FFL phase.

In addition, cell-cell interactions during the RO phase cause more erratic flagellar wave patterns than those during the FFL phase, which is reflected in the standard deviations (SDs) of the time-dependent wave variables. For instance, the SDs of beat frequencies of the flagella over the RO phase are 6.0 rad/mm and 8.8 rad/mm, which are larger than that over the FFL phase, 2.5 rad/mm and 7.4 rad/mm (see Table 2.1).

During the RO phase, the flagellar waves of the cells repeatedly transition between synchronization and desynchronization (Appendix, movie S1). However, once the heads of the spermatozoa are firmly fixed together, flagellar beats are synchronized immediately by the mechanical coupling. Owing to the coupled hydro-mechanical interactions, the sperm cells resume steady flagellar beats. During this SS phase, the wave variables and net swimming speed of the cells converge, as shown in Figure 2.8. Further, the SDs of the wave variables during the SS phase in the high-viscosity experiment are smaller than those in the other phases, implying that the mechanical coupling between the heads can promote the stability of flagellar

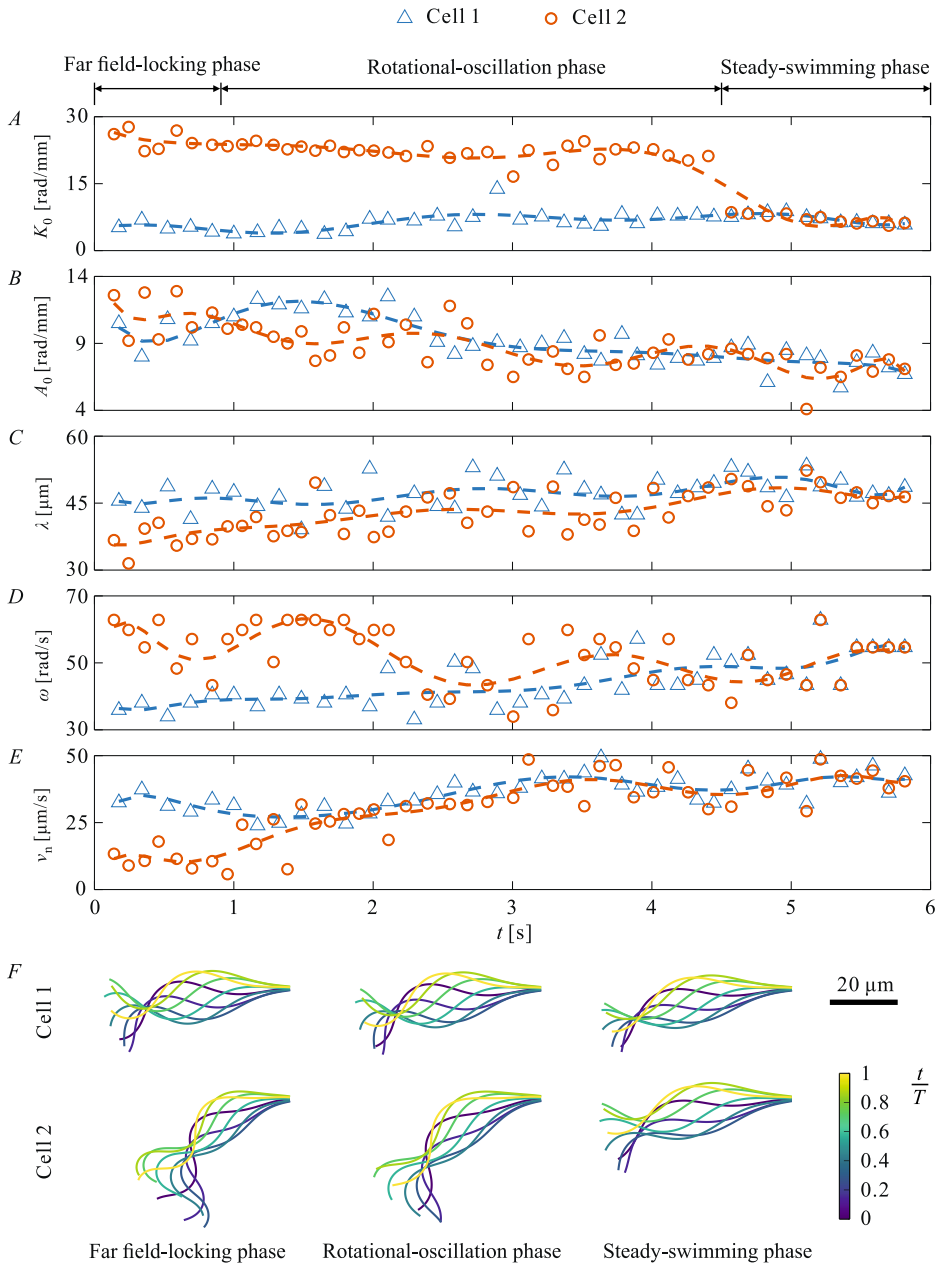

Figure 2.8: Time-dependent wave variables of the cells are measured across the bundle formation in a high-viscosity medium of 15 mPas.

wave patterns even in the presence of hydrodynamic interactions.

Comparing these averaged wave variables in Table 2.1 over the FFL phase and SS phase, we find that the in-phase synchronization of the flagella has an averaging effect on the mean flagellar curvature, while the amplitudes and wavelengths of both the cells decrease. Figure 2.8*F* shows the flagellar waveforms in each phase, which are reconstructed using the averaged wave variables over their respective phases. These waveforms during one beat cycle (t/T, 0–1) demonstrate the significant influence of the cell-cell interactions on the flagellar beats. Note that the net swimming speed of the sperm bundle is enhanced rather than averaged between the cells (Figure 2.8*E*). The average net swimming speeds of the cells over the FFL phase are $\langle {}^1v_\mathrm{n}\rangle_\mathrm{FFL} = 32.7 \pm 3.1\,\mu\mathrm{m/s}$, $\langle {}^2v_\mathrm{n}\rangle_\mathrm{FFL} = 11.6 \pm 3.3\,\mu\mathrm{m/s}$ (mean±SD), and the average net swimming speed of the sperm bundle over the SS phase is $\langle v_\mathrm{n}\rangle_\mathrm{SS} = 40.4 \pm 5.2\,\mu\mathrm{m/s}$ because the angular frequency ω_1 is enhanced greatly by cell 2, while there is only a slight variation in ω_2, ${}^1A_0$, ${}^2A_0$, ${}^1\lambda_0$ and ${}^2\lambda_0$.

2.4.6 Flagellar Beats during the Transition in Low-Viscosity Medium

Different from the sperm cells that beat their flagella from side to side in the high-viscosity medium of $\mu = 15\,\mathrm{mPas}$, the cells in the low-viscosity medium of $\mu = 1.2\,\mathrm{mPas}$ exhibit one-sided strokes due to weaker suppressing effect of low-viscosity media on the flagellar chirality [52], [64] and lateral head displacement [189] (Appendix, movie S2). Cell 1 beats its flagellum in the negative direction of ${}^1\boldsymbol{e}_2$, and cell 2 beats its flagellum in the positive direction of ${}^2\boldsymbol{e}_2$, leading the cells to swim clockwise and counterclockwise during the FFL phase, respectively (Appendix, movies S1 and S2). Facilitated by the cell-cell attraction, the spermatozoa approach. The hydrodynamic interaction leads cell 2 to achieve a longer wavelength and hence an enhanced net swimming speed during the time 0–0.5 s (Figure 2.9). However, cell 1 drastically decelerates its beating during a short time before and after the cells adhere (0.4–0.7 s) for unknown reasons, accounting for its declined net swimming speed.

After the cells assemble into a bundle, the swimming speed of cell 2 is immediately reduced by cell 1. But the wave variables of the cells change gradually. For both the cells, the amplitudes first decrease (0.6–1.2 s) and

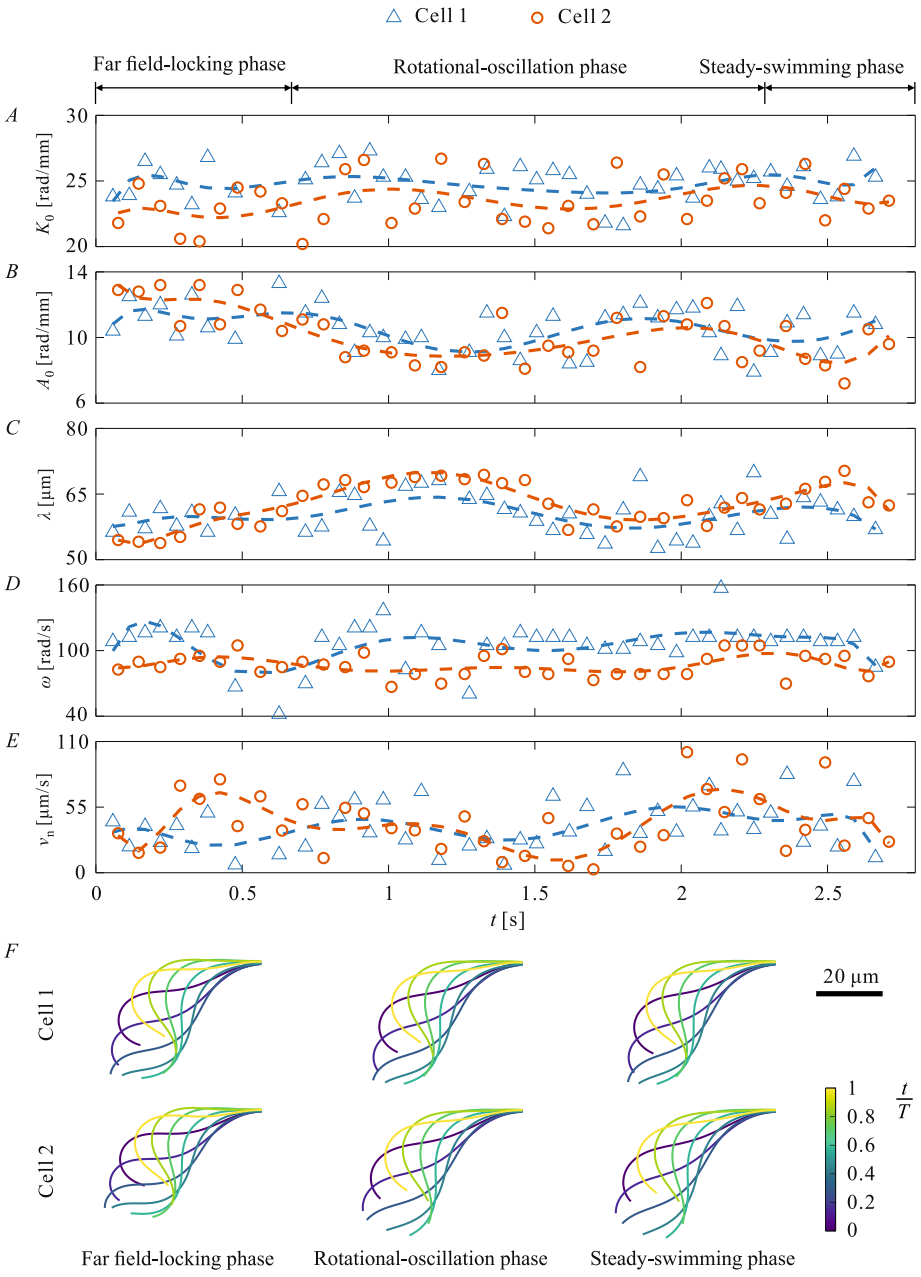

Figure 2.9: Time-dependent wave variables of the cells are measured across the bundle formation in a low-viscosity medium of 1.2 mPas.

then increase (1.2–1.9 s) (Figure 2.9*B*), while the wavelengths increase first (0.2–1.2 s) and then decrease (1.2–1.9 s) (Figure 2.9*C*). The suppressing effect on the amplitudes is attributed to the coupled hydro-mechanical interactions rather than only the hydrodynamic interactions. Because if the suppressing effect only resulted from the hydrodynamic interaction, the amplitudes would be most suppressed immediately after the heads come into contact, when the flagella are so close that they can induce significant hydrodynamic forces. Comparing the average wave variables over the SS phase and that over the FFL phase, we can find that the amplitudes of both cells decline (Table 2.1). This is likely to result from the physical constraint between the cells. A similar phenomenon has been reported when spermatozoa are confined in a microtube which resulted in a smaller bending amplitude of the cells [190].

However, unlike in the high-viscosity case, no significant changes in the mean flagellar curvature are found during the bundle formation. This is because the attachment of the heads is weak, allowing the heads to rotate relatively. The hydrodynamic interaction by itself is not sufficient to alter the mean flagellar curvature significantly, as reported previously [14]. Besides, the weak mechanical coupling between the heads causes the failure of in-phase flagellar synchronization. Consequently, the net swimming speed of the sperm bundle is not enhanced, and instead it is averaged between the two cells. The average net swimming speeds of the cells over the FFL phase are $\langle {}^1v_\mathrm{n}\rangle_\mathrm{FFL} = 34.2 \pm 11.5\,\mu\mathrm{m/s}$, $\langle {}^2v_\mathrm{n}\rangle_\mathrm{FFL} = 48.0 \pm 21.7\,\mu\mathrm{m/s}$, and the average net swimming speed of the sperm bundle over the SS phase is $\langle v_\mathrm{n}\rangle_\mathrm{SS} = 42.3 \pm 26.2\,\mu\mathrm{m/s}$. We also find the wavelength of cell 2 is elongated significantly from an average value of $\langle {}^2\lambda\rangle_\mathrm{FFL} = 57.5 \pm 3.3\,\mu\mathrm{m}$ to $\langle {}^2\lambda\rangle_\mathrm{SS} = 65.4 \pm 3.2\,\mu\mathrm{m}$. The elongated wavelength has also been observed previously in sperm bundles with in-phase flagellar synchronization [14].

2.5 Discussions

cell-cell interactions exist across the whole course of the bundle formation, therefore the motion of sperm bundles cannot be simply described as the locomotion of two individual spermatozoa. Spermatozoa were usually regarded as "pusher" swimmers, which repel fluid lengthwise and draw fluid laterally [31], [191]. The fluid repelled lengthwise provides thrust for the cells, while the fluid drawn laterally attracts the cells. The cell-surface

attraction has been observed in spermatozoa [192] and *Escherichia coli* bacteria [1], [139]. It seems that cell-cell attraction occurs certainly. However, unlike the hydrodynamic cell-surface interaction, the hydrodynamic cell-cell interaction involves two or more motile entities. A change in the relative orientation $\Delta\theta$, distance between two cells, the phase shift between flagellar waves $\Delta\phi$, or flagellar waveform may turn a pusher into a puller (Figures 2.3 to 2.5), which is in agreement with previous numerical studies [136], [157], [162]. Note that recent studies indicate that a microswimmer may oscillate between a pusher and a puller during its flagellar beat and behave as a puller on average [137], [138].

Further, both viscosity and elasticity of fluids can significantly influence the locomotion of sperm cells and hence the hydrodynamic interactions between cells when the storage modulus of the fluid is significant [52], [70]. Beyond the linearity limit, the storage modulus of the medium in our high-viscosity experiment is very small compared with the loss modulus, rendering it a highly viscous–weakly elastic fluid. Thus, it can be assumed that the elastic properties of the fluid are small compared to the viscous properties. The high-viscosity fluid is shear-thinning. In our calculation, we consider the viscosity of the high-viscosity fluid as a constant during one beat cycle for simplicity. Hydrodynamic forces scale linearly with the fluid viscosity. A sole increase/decrease in the fluid viscosity will lead to greater/weaker hydrodynamic attraction/repulsion (Figure 2.A2). However, a change in the fluid viscosity often leads sperm cells to exhibit different flagellar wave patterns, whereby sperm cells may behave as pullers at certain points during the beat cycle [138], [193].

Our results raise the question of whether sperm cells have evolved structures that are inclined to attract other cells to form sperm bundles. Further studies need to be conducted. However, assuming that they induce attractive flow fields, it is certain that not every sperm cell can form a bundle for at least two reasons. First, the attractive flow field is not always sufficient to overcome stochastic thermal fluctuations, especially when the cells are at a large distance [1], [157]. Additionally, the head-to-head attachment is impacted by adhesion proteins on the sperm surface [170] as well as the presence of calcium cations [194], heparin[195], or other membrane charge–changing components in fluids. Therefore, the heads of sperm do not always succeed in adhering when the heads come into contact, which can be confirmed by some cells observed in Appendix, movie S1.

Thus far, we know that the flagellar beat of sperm bundles is regulated by the coupled hydro-mechanical cell-cell interactions. Is the hydrodynamic interaction or the mechanical interaction dominant in inducing the in-phase flagellar synchronization? Our experiments support the latter. In the high-viscosity experiment, the flagella are in the transition between in-phase synchronization and desynchronization during the RO phase, and in-phase synchronized immediately when the sperm heads are attached rigidly. Another supporting example is the sperm bundle in the low-viscosity experiment, whose head-to-head attachment is weak, and flagellar beats are out of phase. Our observations are in agreement with the previous theory predictions [196] and experimental observations [14] that mechanical coupling is a dominant mechanism for in-phase flagellar synchronization in sperm bundles. Although previous investigation suggests that in-phase flagellar/ciliary synchronization can be achieved only through hydrodynamic interactions [157], [197], which is seemingly not observed experimentally.

In-phase flagellar synchronization highlights the temporal component of flagellar waves, whereas the waveform represents the spatial component of flagellar waves. Is the hydrodynamic interaction or the mechanical interaction dominant in regulating the waveform? Our experiments support the latter. In the high-viscosity experiment, a significant change in the mean flagellar curvature of cell 2 occurs immediately when the relative rotational motion of the heads is stopped by the mechanical coupling between the heads, after which the wave variables become less erratic even in the presence of hydrodynamic interactions (Figure 2.8*A*). Our observations infer the dominant role of mechanical interactions in the in-phase synchronization of sperm flagellar beats and the regulation of sperm flagellar waveform. However, because of the limited number of observations of sperm bundle formation, more observations are required to further investigate the correlation between the interactions and the flagellar waveform or synchronization.

Synchronized flagella not only enhance the swimming speed of sperm cells but also consume less energy than desynchronized flagella [70], [74], [125], [157]. This locomotion strategy of sperm cells can be further implemented into the design and development of multiflagellated soft microrobots that can generate increased propulsive thrust to overcome greater flow rates of bodily fluids [198]. Note also that our theoretical and experimental framework for the formation of the sperm bundle of two cells can be

generalized to investigate the formation of bundles of more than two cells. In the system of multiple cells, the formation course can also be divided into phases according to the experiment. The equations for a single cell in this study remain valid for any cell in the system of multiple cells.

In conclusion, the time-dependent wave variables are measured to characterize the collective locomotion of sperm cells during the transition from individual cells to bundles of two cells, which further reveal the dynamic mechanisms for bundle formation. We find that the cell-cell interactions can lead to the time-varying flagellar wave pattern as well as three consecutive collective behaviors: hydrodynamic attraction/repulsion, alignment, and in-phase synchronization. Further, the distinct wave variables during the three phases (i.e. the FFL, RO, and SS phase) infer that the rigid head-to-head attachment is necessary for the in-phase flagellar synchronization and hence the increased swimming speed.

2.6 Appendix

2.6.1 Sperm Cell Preparation

Cryopreserved bovine semen straws are obtained from Masterrind GmbH and stored in liquid nitrogen until use. Semen straws are thawed in 37°C water bath and suspended in 1 mL modified tyrode's albumin lactate medium (SP-TALP) (Caisson Labs), supplemented with 60 mg bovine serum albumin (Sigma Aldrich), 10 µL gentamicin sulfate (Caisson Labs), and 0.5 mL 100 mM sodium pyruvate (Thermofisher), resulting in 1.2 mPas viscosity. The sperm medium with increased viscosity of 15 mPas (shear rate 100 1/s) is prepared by adding 1% methyl cellulose to SP-TALP medium [199].

2.6.2 Image Acquisition

Five microliters of sperm suspension are pipetted into Leija slides with a chamber height of 20 micrometers. Videomicroscopy is performed in an inverted microscope with a heated stage (37°C) and a Phantom Miro high-speed camera and a 40× objective in phase contrast mode, obtaining video sequences with 200 and 500 frames per second for the high-viscosity experiment and the low-viscosity experiment, respectively. When acquiring the flagellar waveform, we track the flagella based on the customized script

in Matlab. The shapes of the sperm cells are extracted from the recorded images at a constant time interval (5 ms for the high-viscosity experiment and 2 ms for the low-viscosity experiment). Further, the end frame of one beat cycle is the frame wherein the flagellum first recovers to the position in the start frame. Because the period of the beat cycles always changes, the number of frames for the beat cycles is determined artificially.

2.6.3 Rheological Measurements

Oscillatory shear experiments for the high-viscosity fluid (1% methyl cellulose) are performed at 37°C, using a rheometer (MCR 92, Anton Paar) with a cone-plate geometry (CP-25-1, diameter: 25 mm, angle: 1°) (Figure 2.A5). The limit of the linear viscoelastic region is approximately 1%, beyond which the storage modulus G' decreases faster than the loss modulus G''. Beyond the linearity limit, storage modulus G' is very small compared with loss modulus G''. For the low-viscosity fluid (SP-TALP), the storage modulus G' is also small compared to loss modulus G'' [200].

2.6.4 Characterization of the Locomotion of Sperm Cells

The extracted shapes of the ith sperm cell at a time t can be represented in terms of the position vector of the centerline of the flagellum ${}^i\boldsymbol{r}(s_i,t)$ in the laboratory frame for each arc length s_i as follows [75](Figure 2.1B):

$$ {}^i\boldsymbol{r}(s_i,t) = {}^i\boldsymbol{r} - a\,{}^i\boldsymbol{e}_1 - \int_0^{s_i} \mathrm{d}s \cos {}^i\psi(s,t)\,{}^i\boldsymbol{e}_1 + \sin {}^i\psi(s,t)\,{}^i\boldsymbol{e}_2, \tag{2.3} $$

where a is the semi-major axis of the head, ${}^i\boldsymbol{r}$ is the position vector of the center of the sperm head, and ${}^i\psi(s_i,t)$ is the tangent angle enclosed between the local tangent vector at ${}^i\boldsymbol{r}(s_i,t)$ to the flagellar centerline and the unit vector ${}^i\boldsymbol{e}_1$. In the co-moving frame, the tangent angle ${}^i\psi(s_i,t)$ of the ith flagellum can be decomposed and approximated by the zeroth and first Fourier modes [80]

$$ {}^i\psi(s_i,t) \approx {}^i\psi_0(s_i) + {}^i\psi_1(s_i)\mathrm{e}^{j\omega_i t} + {}^i\psi_1^*(s_i)\mathrm{e}^{-j\omega_i t}. \tag{2.4} $$

The mean flagellar curvature ${}^iK_0$, bending amplitude ${}^iA_0$, and wavelength λ_i of the principal traveling wave along the flagellum at frequency ω_i can

be derived from the zeroth and first Fourier mode:

$$ {}^{i}K_0 = \frac{{}^{i}\psi_0(s_i)}{s_i}, \qquad {}^{i}A_0 = \frac{|{}^{i}\psi_1(s_i)|}{s_i}, \qquad \lambda_i = -\frac{2\pi s_i}{\arg {}^{i}\psi_1(s_i)}. \tag{2.5} $$

The wave variables (K_0, A_0, λ, and ω) complete the kinematics of the beating flagellum in the co-moving frame. After the time-varying wave variables are derived from the recorded images of the sperm cells, the position and velocity of every discretized element on the cells can be reconstructed [75], and used in the calculation of hydrodynamic forces on the sperm cells and flow fields.

2.6.5 Calculation of the Flow Fields and Hydrodynamic Forces on Sperm Cells

The flagellum is modeled as a tube with a radius of 0.25 µm and a length of 60 µm. The head of sperm is modeled as an ellipsoid, and the dimensions of the head are 9 µm (length), 5 µm (width), and 1 µm (height), respectively. The flagellum is discretized with cross sections along its length, and 6 regularized Stokeslets are used on the perimeter of each circular cross-section. The adjacent cross sections are equally separated by a distance equal to the radius of the flagellum. The head is discretized with cross sections along its long axis, and the adjacent cross sections of the head are also equally separated by a distance equal to the radius of the flagellum. On each of the cross sections, the distance between two adjacent regularized Stokeslets is equal to the distance between two adjacent regularized Stokeslets on the cross-section of the flagellum. Assume that there are N regularized Stokeslets on the surface of each cell. The fluid response $\boldsymbol{u}(\boldsymbol{x})$ at $\boldsymbol{x}_0$ to the hydrodynamic forces induced by two flagella is described by the regularized Stokeslets [149]:

$$ \boldsymbol{u}\left(\boldsymbol{x}_0\right) = \frac{1}{8\pi\mu} \sum_{k=1}^{2N} \sum_{i=1}^{3} S_{ij}^{\epsilon}\left(\boldsymbol{x}_k, \boldsymbol{x}_0\right) {}^{i}\boldsymbol{f}_k A_k, \tag{2.6} $$

where ${}^{i}\boldsymbol{f}_k$ is the ith component of the force on the fluid applied at $\boldsymbol{x}_0$ and A_k is the quadrature weight of the kth regularized Stokeslets. The regularized Green's function S_{ij}^{ϵ} is given by

$$ S_{ij}^{\epsilon}\left(\boldsymbol{x}, \boldsymbol{x}_0\right) = \delta_{ij} \frac{r^2 + 2\epsilon^2}{\left(r^2 + \epsilon^2\right)^{3/2}} + \frac{\left(x_i - x_{0,i}\right)\left(x_j - x_{0,j}\right)}{\left(r^2 + \epsilon^2\right)^{3/2}}, \tag{2.7} $$

where ϵ is the regularization parameter, and is set as a value to be half of the radius of the flagellum. Note that the index i in Equations (2.6) and (2.7) is used for Einstein summation convention, and does not represent the values for ith cell. Distance r is given by

$$r = |\boldsymbol{x} - \boldsymbol{x}_0| \tag{2.8}$$

Equation (2.6) shows that the fluid response $\boldsymbol{u}(\boldsymbol{x})$ is entirely dependent on the instantaneous motion and the configuration of sperm cells. In turn, the hydrodynamic force ${}^i\boldsymbol{f}_k$ is obtained using Equation (2.6), where the velocity $\boldsymbol{u}(\boldsymbol{x})$ is derived from the experimental measurements of the time-dependent locomotion of the sperm cells.

Over one beat cycle T (discretized into 32 time step), the time-averaged hydrodynamic force on the ith cell $\langle {}^i\boldsymbol{F} \rangle$ is given by

$$\langle {}^i\boldsymbol{F} \rangle = \frac{1}{32} \sum_{t=1}^{32} \sum_{k=1}^{N} {}^i\boldsymbol{f}_k\,(t). \tag{2.9}$$

The time-averaged hydrodynamic force is used to characterize the net displacement of sperm cells over one beat cycle.

2.6.6 Calculation of the Propulsive Thrust of Flagella

The propulsive thrust generated by the ith flagellum with length of L_i is computed using the resistive-force theory [97],

$${}^i\boldsymbol{F}_{\mathrm{T}} = \int_0^{L_i} \left[\xi_\perp {}^i\boldsymbol{v}_\perp(s,t) + \xi_\parallel {}^i\boldsymbol{v}_\parallel(s,t) \right] \mathrm{d}s, \tag{2.10}$$

where $\xi_\perp$ and $\xi_\parallel$ are the friction coefficients, and ${}^i\boldsymbol{v}_\perp$ and ${}^i\boldsymbol{v}_\parallel$ are the local normal and parallel velocity components along the ith flagellum, respectively. The velocity ${}^i\boldsymbol{v}_\perp$ and ${}^i\boldsymbol{v}_\parallel$ are obtained by the force balance on the head and the flagellum as well as the torque balance described in Equation (2.1) [92], [97]:

$$6\pi\mu a C_2 {}^iv_x = {}^i\boldsymbol{F}_{\mathrm{T}} \cdot {}^i\boldsymbol{e}_1, \qquad 6\pi\mu a C_3 {}^iv_y = {}^i\boldsymbol{F}_{\mathrm{T}} \cdot {}^i\boldsymbol{e}_2, \tag{2.11}$$

where C_2 and C_3 are the friction coefficients on the head, and ${}^iv_x$ and ${}^iv_y$ are the velocity of the head along the x-axis and y-axis, respectively.

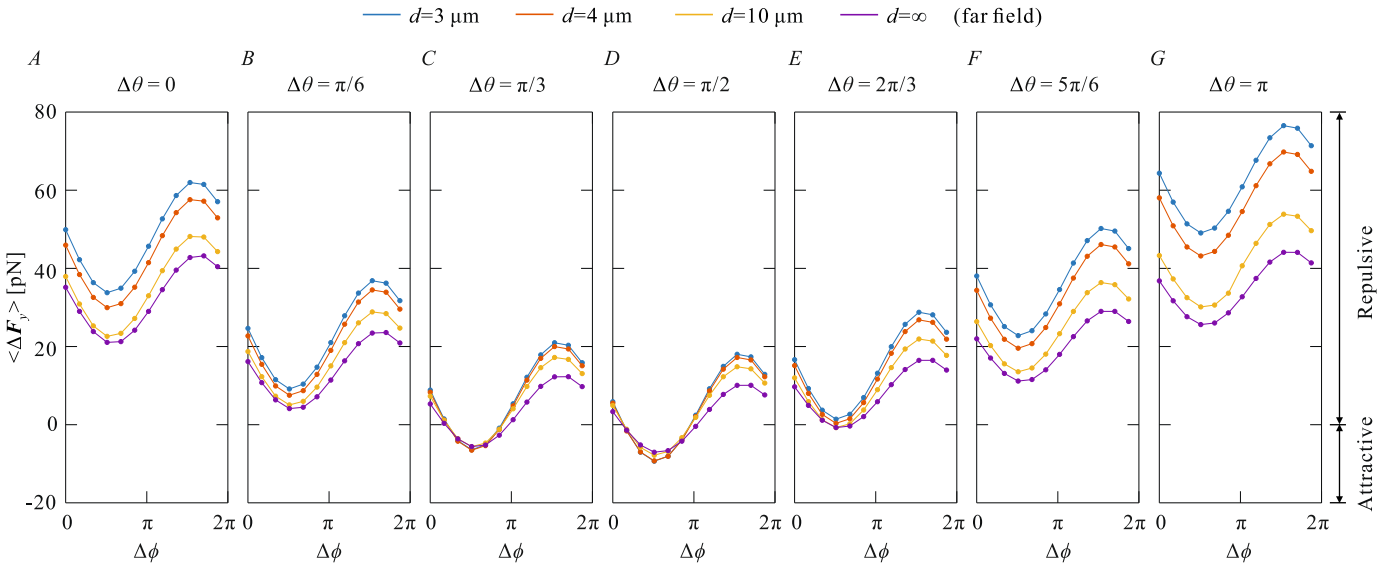

Figure 2.A1: The relation between $\langle \Delta \boldsymbol{F}_y \rangle$ and the distance sperm cells from the bottom surface d. $\langle \Delta \boldsymbol{F}_y \rangle$ denotes the difference between the hydrodynamic force on the cells along the y-axis. $\Delta\phi$ denotes the phase shift between the flagellar waves between the cells. $\Delta\theta$ denotes the angle between the cells. When the cells are closer to the bottom surface, the forces $\langle \Delta \boldsymbol{F}_y \rangle$ are greater in nearly all configurations of the cells. (A-G) are the case $\Delta\theta$ equals 0, $\pi/6$, $\pi/3$, $\pi/2$, $2\pi/3$, $5\pi/6$, and π, respectively. In each figure, $\langle \Delta \boldsymbol{F}_y \rangle$ is calculated for $\Delta\phi$ equals 0, $\pi/6$, $\pi/3$, $\pi/2$, $2\pi/3$, $5\pi/6$, π, $7\pi/6$, $4\pi/3$, $3\pi/2$, $5\pi/3$, and $11\pi/6$. The flagellar wave patterns are characterized by the wave variables ${}^1K_0$ =5.3 rad/mm, ${}^1A_0$ =9.8 rad/mm, λ_1 =45.6 μm, $\omega_1 = 45.5$ rad/s, ${}^2K_0$ =24.8 rad/mm, ${}^2A_0$ =11.2 rad/mm, λ_2 =36.8 μm, and $\omega_2 = 45.5$ rad/s. The values of these wave variables are the averaged values over the far field–locking phase.

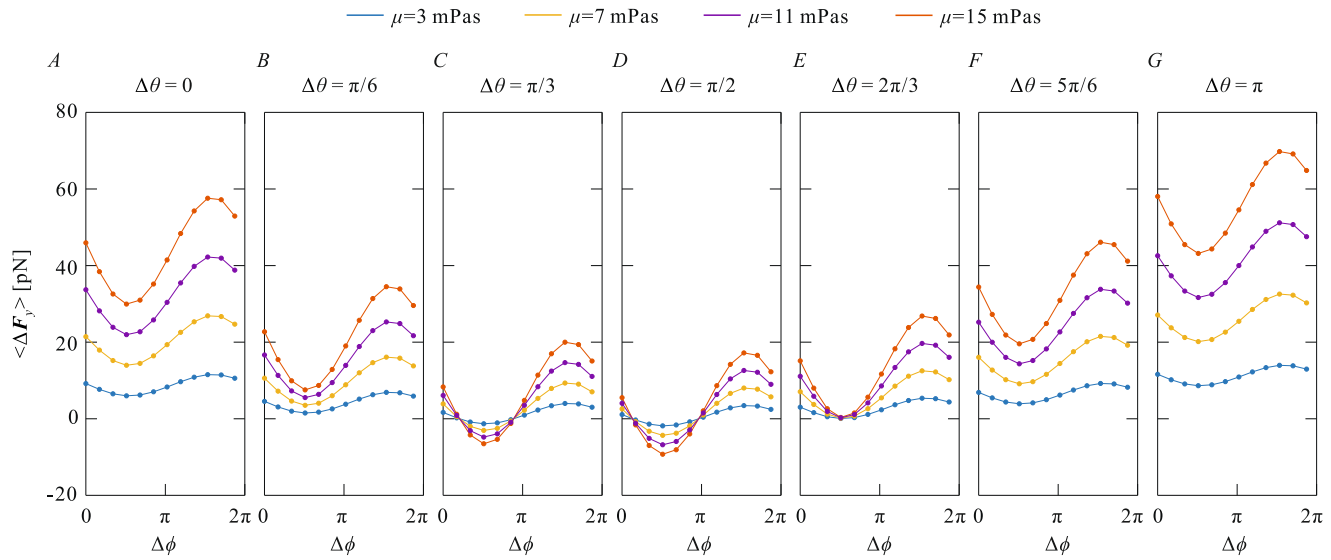

Figure 2.A2: The relation between $\langle \Delta \boldsymbol{F}_y \rangle$ and the fluid viscosity μ. $\langle \Delta \boldsymbol{F}_y \rangle$ denotes the difference between the hydrodynamic force on the cells along the y-axis. $\Delta\phi$ denotes the phase shift between the flagellar waves between the cells. $\Delta\theta$ denotes the angle between the cells. The forces $\langle \Delta \boldsymbol{F}_y \rangle$ are linear with the viscosity in all configurations of the cells, regardless of $\Delta\theta$ or $\Delta\phi$. (A-G) are the case $\Delta\theta$ equals 0, $\pi/6$, $\pi/3$, $\pi/2$, $2\pi/3$, $5\pi/6$, and π, respectively. In each figure, $\langle \Delta \boldsymbol{F}_y \rangle$ is calculated for $\Delta\phi$ equals 0, $\pi/6$, $\pi/3$, $\pi/2$, $2\pi/3$, $5\pi/6$, π, $7\pi/6$, $4\pi/3$, $3\pi/2$, $5\pi/3$, and $11\pi/6$. The flagellar wave patterns are characterized by the wave variables ${}^1K_0 = 5.3\,\mathrm{rad/mm}$, ${}^1A_0 = 9.8\,\mathrm{rad/mm}$, $\lambda_1 = 45.6\,\mu\mathrm{m}$, $\omega_1 = 45.5\,\mathrm{rad/s}$, ${}^2K_0 = 24.8\,\mathrm{rad/mm}$, ${}^2A_0 = 11.2\,\mathrm{rad/mm}$, $\lambda_2 = 36.8\,\mu\mathrm{m}$, and $\omega_2 = 45.5\,\mathrm{rad/s}$. The values of these wave variables are the averaged values over the far field–locking phase.

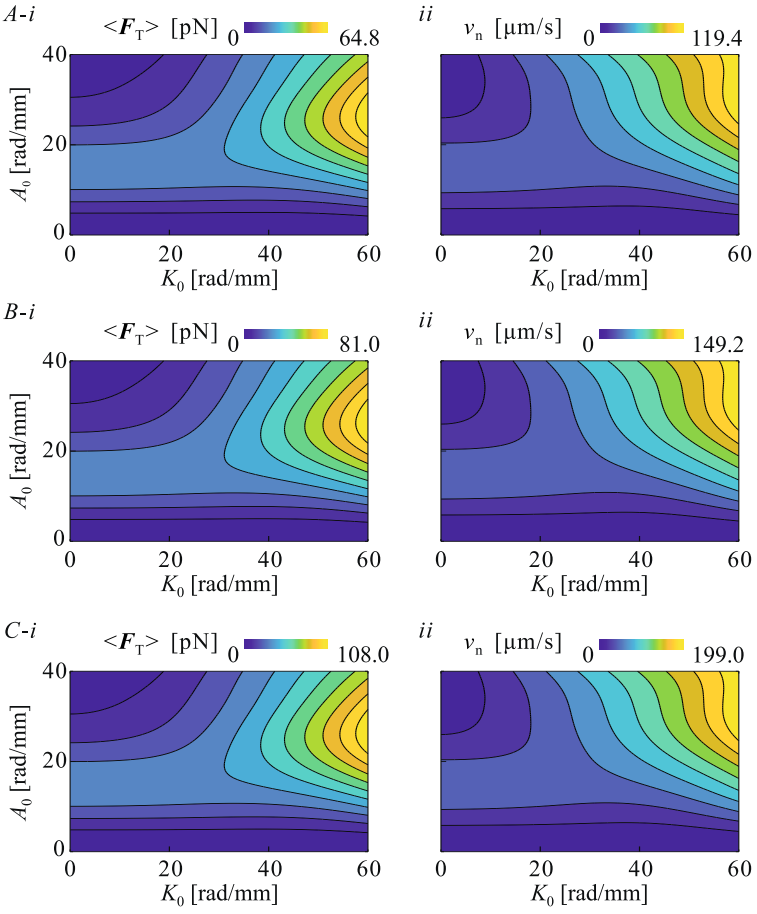

Figure 2.A3: Time-averaged propulsive thrust $\langle \boldsymbol{F}_\mathrm{T} \rangle$ and net swimming speed v_n of the sperm bundle are calculated over the mean flagellar curvature K_0 in the range of 0–60 rad/mm and amplitude rise A_0 of 0–40 rad/mm. Here, the wavelength $\langle \lambda \rangle = 44.8 \pm 4.8\,\mu\mathrm{m}$ is the average value over the three phases in the high-viscosity experiment. The only varying parameter in the calculation among (A), (B), and (C) is the flagellar beat frequency. The three different representative beat frequencies are (A) 56.6 rad/s, (B) 70.9 rad/s, (C) 94.4 rad/s, respectively. The results demonstrate that both the time-averaged propulsive thrust $\langle \boldsymbol{F}_\mathrm{T} \rangle$ and net swimming speed v_n scale linearly with the beat frequency.

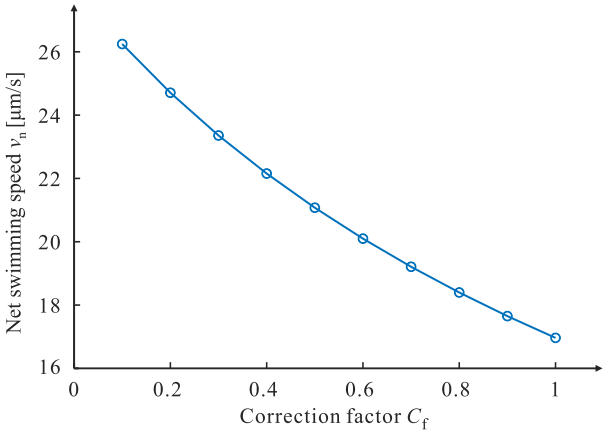

Figure 2.A4: Net swimming speed v_n of sperm bundles is dependent on the head-to-head attachment. The overlapped area of the heads is thought to give rise to the reduction in the hydrodynamic friction on the heads. We simply characterize the impact of the attachment on the net swimming speed v_n by multiplying the friction coefficients on the heads by a correction factor C_f. The calculations show that the head-to-head attachment significantly increases the net swimming speed of sperm cells.

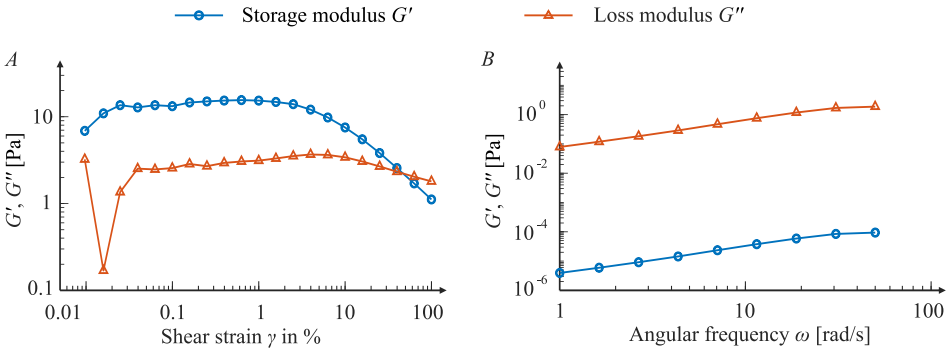

Figure 2.A5: Oscillatory shear experimental results. (A) The amplitude sweep test is performed at shear strain from 0.01% to 100%. The first three data for the storage modulus G' and loss modulus G'' are unreliable due to the limit of resolution of the rheometer, which are excluded from determining the linearity limit. (B) The frequency sweep test is performed at the deformation of 10 and frequencies from 1 to 50 rad/s.

3

Locomotion of Paired Spermatozoa during Flagellar Synchronization

Note: *This chapter is adapted from the article "Locomotion of paired spermatozoa during flagellar synchronisation" by* ***Kaixuan Zhang****, Aaron Lewis, Anke Klingner, Veronika Magdanz, Sarthak Misra, and Islam S.M. Khalil, published in "Journal of Fluid Mechanics", in press, January 2025.*

3.1 Abstract

Microorganisms, such as spermatozoa, exhibit rich behaviours when in close proximity to each other. However, their locomotion is not fully understood when coupled mechanically and hydrodynamically. In this study, we develop hydrodynamic models to investigate the locomotion of paired spermatozoa, predicting the fine structure of their swimming. Experimentally, sperm pairs are observed to transition between different modes of flagellar synchronization: in-phase, anti-phase, and lagged synchronization. Using our models, we assess their swimming performances in these synchronization modes in terms of average swimming speed, average power consumption, and swimming efficiency. The swimming performances of paired spermatozoa are shown to depend on their flagellar phase lag, flagellar waveforms, and the mechanical coupling between their heads.

3.2 Introduction

Flagella or cilia are ubiquitous organelles in eukaryotic cells. They play a crucial role in physiological processes in animals, such as cerebrospinal fluid flow [201], maintenance of the circadian clock [202], and mucociliary clearance in the respiratory system [203]. In the microscopic world, unicellular organisms use their flagella/cilia to efficiently forage and travel, employing diverse locomotion strategies [117], [204]. For instance, *Paramecium* is known to regulate its ciliary beating to swim forwards, backwards, and reorient [7], [205], [206]. *Escherichia coli* exhibits a run-and-tumble locomotion by bundling and unbundling its flagella [10]. The biflagellate alga *Chlamydomonas* transitions between two swimming gaits by modulating the synchronization of its two flagella [207]. Spermatozoa, however, adopt a distinct locomotion strategy by assembling into bundles with their heads attached. This cooperative behaviour has been found to increase their swimming speed [14], [155], providing potential advantages in sperm competition [166], [167].

The increased velocity along the average path of sperm bundles during one beat cycle has been attributed to either their straighter swimming trajectory [164], [171], or their synchronized flagellar beating when the difference between the flagellar beating phase $\Delta\phi$ is a constant for beat cycles [14], [208]. While it has been experimentally observed that in-phase flagellar synchronization ($\Delta\phi = 0$) can increase the swimming speed of paired sperm cells [14], [208], the computational investigation indicates that increased speed results only from anti-phase flagellar synchronization ($\Delta\phi = \pi$) or large flagellar phase lags ($\Delta\phi > \pi/4$) [74]. This discrepancy highlights the complexity of the collective dynamics of sperm bundles. Rich behaviours are also discovered in a simple system comprising two adjacent but separate microswimmers, e.g. hydrodynamic attraction/repulsion [136], [157], alignment [69], [162], oscillation [108], [136], and synchronization [209]–[211]. These behaviours depend on their waveforms and relative displacement, phase, and orientation [72], [108]. Furthermore, current models infer that the hydrodynamic synchronization of co-swimming cells requires geometrically asymmetric waveforms or the presence of a viscoelastic fluid environment [68], [70], [71]. Their swimming speed and efficiency would increase drastically if co-swimming cells mechanically adhere into pairs [125]. These factors also contribute to the rich dynamics observed in other microbial and

artificial swimming systems [1], [212], [213].

Despite many studies on the system of multiple separate microorganisms, the influence of flagellar beating on the locomotion of paired spermatozoa remains largely unexplored experimentally. A few challenges may account for the insufficiency of investigation. First, only a tiny proportion of sperm cells form pairs, restricting the sample size for experimental observation. Second, sperm locomotion is influenced by complex mechanical and hydrodynamic cell-cell and cell-environment interactions, which depend on their flagellar beat patterns and external factors, e.g. the geometry of surrounding environments [58], fluid viscoelasticity [52], [214], and chemoattractants [13], [43], [215]. As a result, it is difficult to control the flagellar beat pattern and experimentally investigate its influence on the locomotion of sperm pairs. Experimental studies of paired spermatozoa have been limited to comparing out-of-phase and in-phase flagellar beat patterns due to these challenges [14], [208].

In our experiments, bovine sperm pairs of two cells with their heads attached were observed in a chamber with a half-depth $h = 10\,\mu\text{m}$ (Figure 3.1*A*). They swam in a plane parallel to the boundary surface of the chamber with primarily planar flagellar beats, similar to the previous experimental observations [14], [77], [78]. The paired sperm cells were experimentally observed to transition between different modes of flagellar synchronization: in-phase ($\Delta\phi = 0$), anti-phase ($\Delta\phi = \pi$), and lagged synchronization ($\Delta\phi$ is a constant not equal to 0 or π). To investigate the influence of flagellar phase lag $\Delta\phi$ on the swimming of sperm pairs, we develop a three-dimensional (3D) hydrodynamic model, referred to as model 1. The attachment between the heads involves adhesion proteins on the head surface and is influenced by factors such as cyclic adenosine monophosphate (cAMP) and sperm antagglutin on the head surface [170], [194]. Considering the yet-fully-understood mechanical coupling due to the head-head attachment, in model 1, we simplify the mechanical head-head coupling as an adhesive force $\boldsymbol{F}_{ij}^{\text{a}}$ between the ith head and jth head. In model 1, the relative oscillation between the heads in a sperm pair is not constrained, such that their orientation difference $\Delta\theta = \theta_2 - \theta_1$ can be positive, zero, or negative (Figure 3.1*B*). In addition, we experimentally observed that the relative oscillation between the heads of paired sperm cells started and paused seemingly randomly, consistent with previous experimental observations [14], [208]. Their orientation difference $\Delta\theta$ was

always a positive value during swimming. Based on these experimental observations, we speculate that a steric force $\boldsymbol{F}_{ij}^{\mathrm{s}}$ may exist between the heads, besides the adhesive force. Therefore, based on model 1, we develop a second model, referred to as model 2, to explore this potential case where both adhesive and steric forces exist between the sperm heads. In model 2, the relative oscillation between the heads is constrained, such that their orientation difference is $\Delta\theta > 0$ during the whole course of swimming (Figure 3.1*C*). Both models 1 and 2 are used to investigate the phase-lag dependence of the swimming performances of paired spermatozoa regarding three parameters: average swimming speed, average power consumption, and swimming efficiency. For each specific flagellar phase lag $\Delta\phi$, its value is prescribed and fixed during the simulation. In models 1 and 2, the head angular velocities $\boldsymbol{\Omega}_i(t), i = 1, 2$, are determined based on force-balance and torque-balance conditions for sperm cells at the low Reynolds number. To further explore the influence of head oscillation on the swimming trajectory of sperm pairs, a third model (referred to as model 3) is developed by providing model 1 with experimentally measured head angular velocities $\boldsymbol{\Omega}_i(t), i = 1, 2$ (Figure 3.1*D*). For more realistic representations, flagellar waveforms are reconstructed from our experimental measurements and prescribed in all our models.

3.3 Tracking of Paired Spermatozoa in a Chamber

Cryopreserved bovine spermatozoa were obtained from Semex Inc (Guelph) and stored in liquid nitrogen. Semen straws were thawed in a 37°C water bath for 2 minutes, before suspending the cells in 2 mL high glucose Dulbecco's Modified Eagle's Medium (DMEM, D6546 Sigma Aldrich). Sperm cells were washed twice by centrifugation at 300 g for 5 minutes and resuspended in a 2 mL clean medium. Then 0.3% Methyl cellulose (M0512, Sigma Aldrich) was added to increase the viscosity of the medium. Five microliters of sperm suspension were pipetted into slides with a chamber depth of 20 µm for immediate videomicroscopy.

Videomicroscopy was performed in an inverted Nikon microscope with a FastCam SA1.1 high-speed camera and a 40× objective in phase contrast mode, obtaining video sequences with 500 frames per second. In our

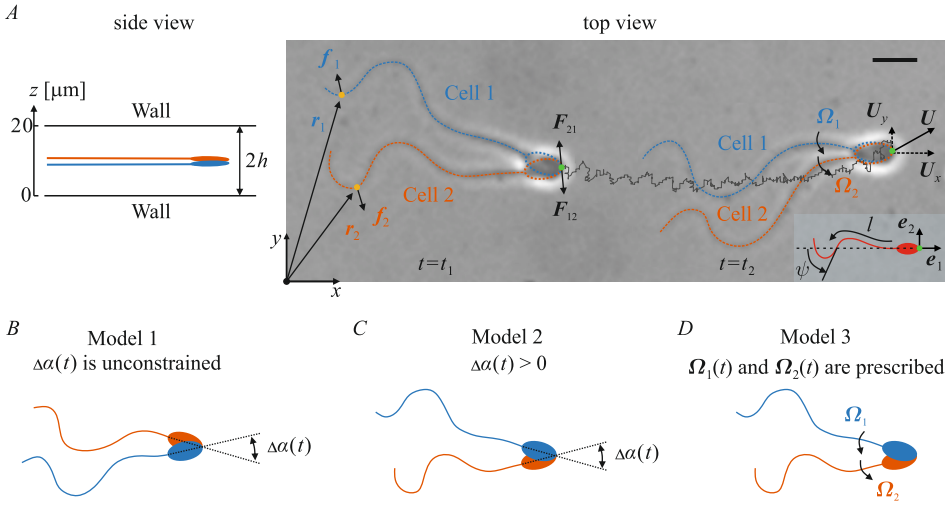

Figure 3.1: (a) Schematic of a pair of bovine spermatozoa swimming in a 20-μm-deep chamber with their heads attached. The paired sperm cells at two instants are overlaid at the same frame of reference. Any point on the ith cell can be described by the position vector $\boldsymbol{r}_i$ with respect to the laboratory frame. The ith cell experiences a hydrodynamic force $\boldsymbol{f}_i$ at an arbitrary point $\boldsymbol{r}_i$. The heads of the sperm pair are attached with no relative translational motion allowed. But they can oscillate relatively about the pivot point (head tip) with instantaneous angular velocities $\boldsymbol{\Omega}_i, i = 1, 2$. The instantaneous translational velocity of the sperm pair $\boldsymbol{U}$ is represented by that of the pivot point. Inset: the co-moving frame is spanned by the orthonormal unit vectors $\boldsymbol{e}_1$ and $\boldsymbol{e}_2$, and its origin overlaps with the pivot point. The flagellar shape in the co-moving frame can be described by the local tangent angle ψ. Forces, F_{ij}, exist between the ith head and the jth head, and are specified differently based on the simplification of the head-head attachment. Three models are developed to investigate the locomotion of paired spermatozoa. (B) In model 1, the head orientation difference $\Delta\theta$ is unconstrained, such that $\Delta\theta$ can be positive, zero or negative. (C) In model 2, $\Delta\theta$ is constrained such that $\Delta\theta > 0$. (D) Time-varying head angular velocities, $\boldsymbol{\Omega}_i, i = 1, 2$, are extracted from experiments and prescribed in model 3. Scale bar: 10 μm.

experiments, paired spermatozoa with their heads attached were observed (Appendix, movie S1). We track the flagella using the customized script in Matlab. The algorithm first detects the head tip and then the junction between the head and flagellum, from which the orientation of each cell is derived. Subsequently, the flagellum of each cell is tracked using the method

reported by Geyer et al. [81] and Riedel-Kruse et al. [80]. The tracked images need to be manually examined and modified when the detection sometimes fails due to, e.g. dirt particles and overlapped flagella. Along each flagellum, 45 points are tracked. These flagellum-points are off to both sides of the flagellum's centre line and are not equally spaced. A Savitzky-Golay filter with a degree of 3 and a span of 5 sequential flagellum-points is used to filter the flagellum-points. These filtered flagellum-points are then interpolated with splines. The arc length of the flagellum is determined by summing the lengths of the splines, and points at equal distances of 0.25 µm along the flagellum are then determined. These equidistant points along the ith flagellum of a sperm pair are time-varying and used to determine their velocity $\boldsymbol{v}_i$ relative to the ith head.

3.4 Characterization of the Locomotion of Paired Spermatozoa

Bovine spermatozoa are approximately 60 µm in length. Approximately 0.1–3% of them, depending on conditions, formed bundles, most of which were sperm pairs [15]. Considering their approximately planar kinematics, we can describe their projected locomotion on the two-dimensional (2D) plane where they swim, and neglect the out-of-plane component, as shown in Figure 3.1. The ith sperm head of a sperm pair can be described by its orientation $\theta_i(t)$ and the position of its head tip $\boldsymbol{r}_\mathrm{p}(t)$ with respect to the laboratory frame. The flagellar shape can be described by the tangent angle ψ with respect to the co-moving frame spanned by the orthonormal unit vectors $\boldsymbol{e}_1$ and $\boldsymbol{e}_2$. Here, $\boldsymbol{e}_1$ and $\boldsymbol{e}_2$ are oriented along the long and short axes of the projection of the ellipsoidal head on the swimming plane, respectively, as illustrated in Figure 3.1 (inset). The tangent angle $\psi(l,t), 0 \leq l \leq 2L$, is enclosed between $\boldsymbol{e}_1$ and the local tangent vector to the flagellar centreline, where L is the half-length of the flagellum. The flagellar shape with respect to the laboratory frame at a time t can be characterized by

$$\boldsymbol{r}_\mathrm{f}(l,t) = \boldsymbol{r}_\mathrm{p}(t) - a\boldsymbol{e}_1 - \int_0^l \mathrm{d}l' \left[\cos\psi(l',t)\boldsymbol{e}_1 + \sin\psi(l',t)\boldsymbol{e}_2\right], \tag{3.1}$$

where a is the major axis of the projection of the head on the swimming plane [75]. Here, $\boldsymbol{r}_\mathrm{f}(0,t)$ corresponds to the head-flagellum junction, and

$\boldsymbol{r}_{\mathrm{f}}(2L,t)$ corresponds to the distal end of the flagellum. This description can be applied to the two flagella of a sperm pair. Any point on the ith cell with respect to the laboratory frame is represented by $\boldsymbol{r}_i(s,t)$, where s is the coordinate of this point.

3.5 Mechanical and Hydrodynamic Cell-Cell Interactions

In our experiments, paired bovine sperm cells, one head on top of the other, oscillated their heads during swimming. From the top view, a portion of the heads, e.g. the head tips, remained overlapping during the whole course of swimming (Figure 3.1). The head tips were the pivot point about which the heads oscillated. The attachment between the heads allowed their relative oscillation within the swimming plane, but constrained their relative translational motion. Similar experimental observations have been reported previously [14], [208]. The head of a bovine spermatozoon resembles an approximately flattened ellipsoid, with detailed cellular morphologies [99], [216]. In our models, we ignore the detailed morphologies of the bovine sperm head and only consider its three principal dimensions—length, width, and height. Thus, the sperm head is simplified as an ellipsoid with dimensions of $9{\times}5{\times}0.4\,\mu\mathrm{m}$ (length×width×height) in our models, based on previous experimental measurements [99], [216]. The flagellum is approximately a tube with a half-length $L = 25\,\mu\mathrm{m}$ and a radius ρ of $0.25\,\mu\mathrm{m}$ [99], [216]. These dimensions for the flagellum are used in our models.

Previous computational studies have shown that the hydrodynamic interaction between two adjacent but separate flagella may lead them to swim away from each other in the 3D space [73], [136]. However, compared with hydrodynamic forces, the mechanical head-head coupling is strong so that paired sperm cells continue to swim together [14], [208]. Therefore, the mechanical head-head coupling and its influence on the swimming of paired spermatozoa cannot be ignored. We simplify the yet-fully-understood head-head coupling as a pair of adhesive forces on the pivot point $\boldsymbol{F}_{ij}^{\mathrm{a}}, i = 1,2$, elaborated in Section 3.5.1. Here, the force on the ith head $\boldsymbol{F}_{ij}^{\mathrm{a}}$ results from the interaction with the jth head, such that $F_{12}^{\mathrm{a}} = -F_{21}^{\mathrm{a}}$. For the second potential case where both adhesive and steric forces exist between the heads, we develop model 2 based on model 1, detailed in Section 3.5.2.

3.5.1 Model of Paired Spermatozoa with Adhesive Forces between Their Heads

Let $\boldsymbol{\Omega}_i(t), i = 1, 2$, denote the instantaneous angular velocity of the ith head about the pivot point, and let $\boldsymbol{U}(t)$ denote the instantaneous translational velocity of the pivot point, with respect to the laboratory frame. The velocity $\boldsymbol{v}_i(s,t)$ at an arbitrary point on the ith flagellum with respect to the co-moving frame is obtained from our experimentally observed time-varying flagellar shapes. Given $\boldsymbol{v}_i(s,t)$, the velocity $\boldsymbol{u}_i(s,t)$ at this point in the laboratory frame is

$$\boldsymbol{u}_i(s,t) = \boldsymbol{v}_i(s,t) + \boldsymbol{U}(t) + \boldsymbol{\Omega}_i(t) \times \boldsymbol{r}_i'(s,t), \tag{3.2}$$

where $\boldsymbol{r}_i'(s,t)$ is the position vector of this point in the co-moving frame [217]. For the velocity of any point on the head, Equation (3.2) is also applicable, where the first term on the right-hand side vanishes. The sperm cells are spatially discretized, as detailed in Section 3.8.1. For the planar locomotion, the velocity ${}^k\boldsymbol{u}_i(t)$ at the kth point on the ith cell in the laboratory frame can be represented by

$${}^k\boldsymbol{u}_i(t) = {}^k\boldsymbol{v}_i(t) + {}^k\boldsymbol{B}_i(t)\mathcal{U}(t), \tag{3.3}$$

where

$$\mathcal{U} = \begin{bmatrix} U_x \\ U_y \\ \Omega_1 \\ \Omega_2 \\ F^{\mathrm{a}}_{21x} \\ F^{\mathrm{a}}_{21y} \end{bmatrix}, \qquad {}^k\boldsymbol{B}_i = \begin{cases} \begin{bmatrix} 1 & 0 & -{}^k r'_{1y} & 0 & 0 & 0 \\ 0 & 1 & {}^k r'_{1x} & 0 & 0 & 0 \\ 0 & 0 & 0 & 0 & 0 & 0 \end{bmatrix}, & i = 1 \\ \begin{bmatrix} 1 & 0 & 0 & -{}^k r'_{2y} & 0 & 0 \\ 0 & 1 & 0 & {}^k r'_{2x} & 0 & 0 \\ 0 & 0 & 0 & 0 & 0 & 0 \end{bmatrix}, & i = 2. \end{cases} \tag{3.4}$$

Here, the subscripts x and y in the variables represent their components along the x- and y-axes, respectively. The angular speeds Ω_1 and Ω_2 are defined such that $\boldsymbol{\Omega}_1 = \Omega_1 \boldsymbol{e}_3$ and $\boldsymbol{\Omega}_2 = \Omega_2 \boldsymbol{e}_3$, where $\boldsymbol{e}_3 = \boldsymbol{e}_1 \times \boldsymbol{e}_2$.

The microscale geometry and swimming speed of spermatozoa render them low-Reynolds-number swimmers. They are generally deemed neutrally buoyant, as their swimming speed dominates their sedimentation speed [218]. Consequently, the swimming paired sperm cells are force-free

and torque-free [31]. The ith cell in a sperm pair satisfies

$$\int_s \boldsymbol{f}_i(s,t)\mathrm{d}s + \boldsymbol{F}_{ij}^{\mathrm{a}}(t) = \boldsymbol{0}, \quad \int_s \boldsymbol{r}_i(s,t) \times \boldsymbol{f}_i(s,t)\mathrm{d}s + \boldsymbol{T}_{ij}^{\mathrm{a}}(t) = \boldsymbol{0}, \tag{3.5}$$

where $\boldsymbol{f}_i(s,t)$ is the hydrodynamic force at point $\boldsymbol{r}_i(s,t)$, as illustrated in Figure 3.1. The adhesive torque on the ith head about the origin of the laboratory frame is $\boldsymbol{T}_{ij}^{\mathrm{a}} = \boldsymbol{r}_{\mathrm{p}} \times \boldsymbol{F}_{ij}^{\mathrm{a}}$. The total torque balances about any point.

The loss modulus of the fluid in our experiments dominates the storage modulus [15], [208]. Consequently, we can neglect the elasticity of the fluid and calculate the hydrodynamic force $\boldsymbol{f}_i(s,t)$ using Stokes equations. To incorporate the wall effect due to the top and bottom slides of the chamber, we introduce two walls in our models, which are at $z = 0\,\mu\mathrm{m}$ and $z = 20\,\mu\mathrm{m}$, respectively, parallel with the x-y plane. According to previous studies, most spermatozoa are within 0.2 times their body length from the bottom surface [77], [184]. We therefore assume that the sperm cells are in the middle between the walls in our models. In the experiments, the sperm heads are physically attached. In the models, they need to be prevented from concurrently occupying the same space. Therefore, a pair of sperm cells is positioned on two parallel 2D planes, respectively, with a minimum distance of $0.25\,\mu\mathrm{m}$ between their heads. Given that the height of the head is $0.4\,\mu\mathrm{m}$, the two swimming planes are set at $z = 9.675\,\mu\mathrm{m}$ and $z = 10.325\,\mu\mathrm{m}$, respectively. This arrangement ensures that the two cells remain in close proximity without overlapping in space.

To determine the hydrodynamic force $\boldsymbol{f}_i$ on the ith cell, we use the regularized Stokeslets method, which is an effective approximation of the low-Reynolds-number flow. We discretize the ith cell into n_i points and the walls into n_{w} points, as detailed in Section 3.8.1. Thus, a total of $n = n_1 + n_2 + n_{\mathrm{w}}$ points are included in our models. The relationship between the force $\boldsymbol{f}_i$ and the velocity $\boldsymbol{u}_i$ can be expressed in a vector form

$$\begin{bmatrix}\boldsymbol{u}_1^T & \boldsymbol{u}_2^T & \boldsymbol{u}_{\mathrm{w}}^T\end{bmatrix}^T = -\boldsymbol{A}\begin{bmatrix}\boldsymbol{f}_1^T & \boldsymbol{f}_2^T & \boldsymbol{f}_{\mathrm{w}}^T\end{bmatrix}^T, \tag{3.6}$$

where $\boldsymbol{f}_{\mathrm{w}}$ is the hydrodynamic force on the stationary wall surfaces, and $\boldsymbol{A}$ is a $3n \times 3n$ matrix (Appendix 3.8.2). The velocity of the n_{w} points on the wall surfaces $\boldsymbol{u}_{\mathrm{w}}$ can be specified by a $3n_{\mathrm{w}} \times 1$ zero matrix, $\boldsymbol{u}_{\mathrm{w}} = \boldsymbol{0}_{3n_{\mathrm{w}}\times 1}$. Combining Equations (3.3–3.6), we derive a linear system to describe the

dynamics of paired sperm cells,

$$\begin{bmatrix} \boldsymbol{v} \\ 0 \\ 0 \\ 0 \\ 0 \\ 0 \\ 0 \end{bmatrix} = - \begin{bmatrix} \boldsymbol{A} & \boldsymbol{B} \\ \boldsymbol{C} & \boldsymbol{D} \\ \boldsymbol{E} & \boldsymbol{F} \\ \boldsymbol{G} & \boldsymbol{H} \\ \boldsymbol{I} & \boldsymbol{J} \\ \boldsymbol{K} & \boldsymbol{L} \\ \boldsymbol{M} & \boldsymbol{N} \end{bmatrix} \begin{bmatrix} \boldsymbol{f} \\ \mathcal{U} \end{bmatrix}, \tag{3.7}$$

where $\boldsymbol{B} = \begin{bmatrix} {}^1\boldsymbol{B}_1^T & {}^2\boldsymbol{B}_1^T & \cdots & {}^{n_1}\boldsymbol{B}_1^T & {}^1\boldsymbol{B}_2^T & {}^2\boldsymbol{B}_2^T & \cdots & {}^{n_2}\boldsymbol{B}_2^T & \boldsymbol{0}_{6\times 3n_\mathrm{w}} \end{bmatrix}^T$, the velocity $\boldsymbol{v} = \begin{bmatrix} \boldsymbol{v}_1^T & \boldsymbol{v}_2^T & \boldsymbol{0}_{1\times 3n_\mathrm{w}} \end{bmatrix}^T$, and the force $\boldsymbol{f} = \begin{bmatrix} \boldsymbol{f}_1^T & \boldsymbol{f}_2^T & \boldsymbol{f}_\mathrm{w}^T \end{bmatrix}^T$. The last six equations in Equation (3.7) represent the force balance along the x- and y-axes, and the torque balance along the z-axis, respectively, for each pair of sperm cells. According to the force-balance and torque-balance conditions, the blocks $\boldsymbol{C}, \boldsymbol{D}, \cdots, \boldsymbol{N}$ of this linear system can be derived (Appendix 3.8.3). In Equation (3.7), velocity $\boldsymbol{v}$ at any time is known, which is provided from experimental observations, but $\boldsymbol{f}$ and all the variables in $\mathcal{U}$ are unknown and need to be determined from Equation (3.7). The velocity $\boldsymbol{u}_i$ at any point on the ith sperm pair with respect to the laboratory frame can be further calculated from Equation (3.3) after $\mathcal{U}$ is determined.

3.5.2 Model of Paired Spermatozoa with Adhesive and Steric Forces between Their Heads

To prevent sperm cells from unrealistically passing through each other, a steric force has been introduced and modelled as an elastic spring with a specific form [74], [125]. The steric force in their model acts only over a very short range to avoid significantly influencing sperm swimming. Likewise, instead of focusing on the specific value of steric force, we expect that the steric force in our model 2 can effectively repel the heads when they approach a total overlap, while having a minimum influence on their relative oscillation when their orientation difference $\Delta\theta > 0$. To this end, we develop model 2 based on model 1. We first consider a scenario in which both heads have the same angular velocity, i.e., $\boldsymbol{\Omega}_1 = \boldsymbol{\Omega}_2 = \boldsymbol{\Omega}$. The velocity ${}^k\boldsymbol{u}_i(t)$ at the kth point on the ith cell in the laboratory frame can continue to be represented by Equation (3.3), but the matrices $\mathcal{U}$ and ${}^k\boldsymbol{B}_i$

need to be modified to

$$\mathcal{U}' = \begin{bmatrix} U_x \\ U_y \\ \Omega \end{bmatrix}, \quad {}^{k}\boldsymbol{B}'_i = \begin{bmatrix} 1 & 0 & -{}^{k}r'_{iy} \\ 0 & 1 & {}^{k}r'_{ix} \\ 0 & 0 & 0 \end{bmatrix}, \; i = 1, 2, \tag{3.8}$$

respectively. As $\boldsymbol{F}_{12}^{\mathrm{a}} = -\boldsymbol{F}_{21}^{\mathrm{a}}$ and $\boldsymbol{F}_{12}^{\mathrm{s}} = -\boldsymbol{F}_{21}^{\mathrm{s}}$, the force-balance and torque-balance conditions on the whole sperm pair are

$$\sum_{i=1}^{2} \int_s \boldsymbol{f}_i(s,t)\mathrm{d}s = \boldsymbol{0}, \quad \sum_{i=1}^{2} \int_s \boldsymbol{r}_i(s,t) \times \boldsymbol{f}_i(s,t)\mathrm{d}s = \boldsymbol{0}. \tag{3.9}$$

Combining Equations (3.3), (3.6), (3.8) and (3.9), we derive a linear system to describe the dynamics of paired sperm cells with the same head angular velocity $\boldsymbol{\Omega}$,

$$\begin{bmatrix} \boldsymbol{v} \\ 0 \\ 0 \\ 0 \end{bmatrix} = - \begin{bmatrix} \boldsymbol{A} & \boldsymbol{B}' \\ \boldsymbol{C}' & \boldsymbol{D}' \\ \boldsymbol{E}' & \boldsymbol{F}' \\ \boldsymbol{G}' & \boldsymbol{H}' \end{bmatrix} \begin{bmatrix} \boldsymbol{f} \\ \mathcal{U}' \end{bmatrix}, \tag{3.10}$$

where $\boldsymbol{B}' = \begin{bmatrix} {}^{1}\boldsymbol{B}_1'^{T} & {}^{2}\boldsymbol{B}_1'^{T} & \cdots & {}^{n_1}\boldsymbol{B}_1'^{T} & {}^{1}\boldsymbol{B}_2'^{T} & {}^{2}\boldsymbol{B}_2'^{T} & \cdots & {}^{n_2}\boldsymbol{B}_2'^{T} & \boldsymbol{0}_{3\times 3n_{\mathrm{w}}} \end{bmatrix}^T$, the velocity $\boldsymbol{v} = \begin{bmatrix} \boldsymbol{v}_1^T & \boldsymbol{v}_2^T & \boldsymbol{0}_{1\times 3n_{\mathrm{w}}} \end{bmatrix}^T$, and the force $\boldsymbol{f} = \begin{bmatrix} \boldsymbol{f}_1^T & \boldsymbol{f}_2^T & \boldsymbol{f}_{\mathrm{w}}^T \end{bmatrix}^T$. The last three equations in Equation (3.10) represent the force balance along the x- and y-axes, and the torque balance along the z-axis for the sperm pair, respectively. According to the force-balance and torque balance conditions, the blocks $\boldsymbol{C}', \boldsymbol{D}', \cdots, \boldsymbol{H}'$ of this linear system can be derived (Appendix 3.8.4). In Equation (3.10), velocity $\boldsymbol{v}$ at any time is known, which is provided from experimental observations, but $\boldsymbol{f}$ and all the variables in $\mathcal{U}'$ are unknown and need to be determined from Equation (3.10). The velocity $\boldsymbol{u}_i$ at any point on the ith sperm pair with respect to the laboratory frame can be further calculated from Equation (3.3) after $\mathcal{U}'$ is determined.

Our simulation consists of n_{t} discrete time steps. If at the beginning of the jth time step, the position $\boldsymbol{r}(t_j)$ of any point on the surface of the sperm cells and the velocity $\boldsymbol{v}(t_j)$ are known, then $\boldsymbol{r}(t_{j+1})$, $\Delta\theta(t_{j+1})$, $\boldsymbol{f}(t_{j+1})$, $\boldsymbol{U}(t_{j+1})$, $\boldsymbol{\Omega}_1(t_{j+1})$, and $\boldsymbol{\Omega}_2(t_{j+1})$ at the beginning of the $(j+1)$th time step can be determined by solving Equations (3.7) or (3.10). In our simulations, the initial position $\boldsymbol{r}(t_1)$ is given, and the velocity $\boldsymbol{v}$ at any

Algorithm 1: Model 2

Input: $\boldsymbol{v}$, $\boldsymbol{r}(t_1)$, $\Delta\theta(t_1)$
Output: $\boldsymbol{r}(t_j)$, $\Delta\theta(t_j)$, $\boldsymbol{f}(t_j)$, $\boldsymbol{U}(t_j)$, $\boldsymbol{\Omega}_1(t_j)$, $\boldsymbol{\Omega}_2(t_j)$

```
j ← 1;
while j ≤ n_t do
    j ← j + 1;
    Get r(t_j), Δθ(t_j), f(t_j), U(t_j), Ω_1(t_j), Ω_2(t_j) from
     Equation (3.7);
    if Δθ(t_j) ≤ 0 then
        Get r(t_j), Δθ(t_j), f(t_j), U(t_j), Ω_1(t_j), Ω_2(t_j) from
         Equation (3.10);
    end
end
```

time step is provided from experimental observations. Assuming that the initial orientation difference between the heads is $\Delta\theta(t_1) \geq 0$, now we can formulate model 2 by combining Equations (3.7) and (3.10) following the method described in Algorithm 1.

In model 2 (i.e., Algorithm 1), sperm heads are fused with zero relative angular velocity, $\Delta\boldsymbol{\Omega} = \boldsymbol{\Omega}_2 - \boldsymbol{\Omega}_1 = \mathbf{0}$, when $\Delta\theta$ is within a very small range close to zero. This range depends on the variation of $\Delta\theta$ over one discrete time step. Note that both adhesive and steric forces between the heads are intrinsically included in model 2, constraining the relative oscillation of the heads such that $\Delta\boldsymbol{\Omega} = \mathbf{0}$ when $\Delta\theta$ is within the range, despite the specific values of the forces and where they are applied being unknown. Only an adhesive force between the heads is included in model 2 when $\Delta\theta$ is out of the range. Thereby, we finish developing model 2, in which sperm heads are effectively prevented from totally overlapping, while having a minimum influence on their relative oscillation when $\Delta\theta > 0$.

3.5.3 Validation of the Models

Model 3 can be developed based on model 1 (i.e., Equation (3.7)) by reducing the vector $\mathcal{U}$ in model 1 to $\mathcal{U} = \begin{bmatrix} U_x & U_y & F^{\mathrm{a}}_{21x} & F^{\mathrm{a}}_{21y} \end{bmatrix}^T$ and removing the two equations associated with the torque-balance condition from Equa-

tion (3.7). Our models build on regularized Stokeslets method, involving a choice of regularized parameter ϵ and spatial discretization of the sperm cells and walls. To validate our discretization of the head and flagellum, following the approach of Cortez et al. [149] and Gillies et al. [86], we compare our predicted resistive force on an isolated head and an isolated flagellum translating in an unbounded fluid with their exact solution. The non-dimensional force error is $e_{\mathrm{f}} < 2.4 \times 10^{-4}$ (Section 3.8.5). In addition, we compute the cumulative distribution of velocity error for a sphere translating in an unbounded fluid with velocity $U_z = 1\,\mathrm{m/s}$. All the points on the surface of the sphere have a velocity error $e_{\mathrm{v}} = |U_z - 1| < 0.018\,\mathrm{m/s}$ (Section 3.8.5). To regularize the walls in our models, the regularized parameter ϵ is chosen in the form, $\epsilon = \xi\rho^m$ [86], [150]. In our test cases, $\xi = 0.5$ and $m = 0.9$ are chosen, which yields predictions that closely match the published results (Section 3.8.6). Therefore, these values of ξ and m are used in our models for all subsequent simulations. The walls in our models are square. The simulations in the test cases are insensitive to the wall size when the side length of the walls ranges from 60 to 160 µm, as shown in Section 3.8.6. Therefore, the side length of each wall is set to 80 µm in our models, which is fixed in all our subsequent simulations.

3.5.3.1 Force and Torque Errors

We use our models to simulate the locomotion of a sperm pair. In the simulations, the viscosity is chosen as $\mu = 1\,\mathrm{Pa\,s}$, and the flagellar beat patterns are prescribed based on the experimental measurements. For model 3, prescribed head angular velocities $\boldsymbol{\Omega}_i(t), i = 1, 2$ are further required.

Regarding models 1 and 2, force-balance conditions along the x- and y-axes and torque-balance conditions along the z-axis are applied. As the mechanical coupling between the heads is a pair of internal forces, the total hydrodynamic force on the whole sperm pair along the x- and y-axes should satisfy $F_x = \sum_{i=1}^{2} F_{ix} = 0$ and $F_y = \sum_{i=1}^{2} F_{iy} = 0$, where F_{ix} and F_{iy} are the x- and y-components of the total hydrodynamic force on the ith cell, respectively. Likewise, the total hydrodynamic torque on the whole sperm pair along the z-axis should satisfy $T_z = \sum_{i=1}^{2} T_{iz} = 0$, where T_{iz} is the z-component of the total hydrodynamic torque on the ith cell. As shown in Figure 3.2, the absolute values, $|F_x|$, $|F_y|$, and $|T_z|$ are minimal. The minimal values result from the numerical error. The absolute value

of the total hydrodynamic force on the sperm pair along the z-axis, $|F_z|$, is also very small. We take the total hydrodynamic force on cell 1, $|F_1|$, as the benchmark, and $|F_z|$ is three orders of magnitude lower than $|F_1|$, despite no force-balance condition along the z-axis applied to the sperm cells. Likewise, taking $|T_1|$ as the benchmark, the absolute values of the total hydrodynamic torque on the sperm pair along the x- and y-axes, $|T_x|$ and $|T_y|$, are three orders of magnitude lower than $|T_1|$, despite no torque-balance conditions along the x- and y-axes applied to the sperm cells.

Regarding model 3, force-balance conditions along the x- and y-axes are applied to the sperm cells. The absolute values, $|F_x|$ and $|F_y|$, are minimal due to the numerical error, as shown in Figure 3.2(A,*iii*). In addition, $|F_z|$ is three orders of magnitude lower than $|F_1|$, and $|T_x|$, $|T_y|$, and $|T_z|$ are three orders of magnitude lower than $|T_1|$, despite no force-balance condition along the z-axis and no torque-balance conditions along the x-, y-, and z-axes applied to the sperm pair.

3.5.3.2 Comparison of the Predicted and Experimentally Observed Trajectories of Sperm Pairs

Following previous studies [86], [219], we assess our models by comparing the predicted and experimentally observed swimming trajectories. Three sperm pairs are simulated using our models. The trajectory of each sperm pair is the time-varying position of their pivot point, as shown in Figure 3.3. We calculate the displacement d and traveling distance S of the pivot point during one flagellar beat cycle T. The displacement during the jth flagellar beat cycle d is defined as

$$d = \frac{1}{n_\mathrm{t}} \sum_{i=1}^{n_\mathrm{t}} \left| \boldsymbol{r}_\mathrm{p}(t_i + T) - \boldsymbol{r}_\mathrm{p}(t_i) \right|, \tag{3.11}$$

where n_t is the number of the time steps during one flagellar beat cycle T. The displacement, $|\boldsymbol{r}_\mathrm{p}(t_i + T) - \boldsymbol{r}_\mathrm{p}(t_i)|$, depends on the initial time t_i during one beat cycle. We thus define d by averaging $|\boldsymbol{r}_\mathrm{p}(t_i + T) - \boldsymbol{r}_\mathrm{p}(t_i)|$ over one beat cycle using Equation (3.11). The traveling distance of the pivot point during the jth flagellar beat cycle S is defined as $S = \sum_{i=1}^{n_\mathrm{t}} |\boldsymbol{r}_\mathrm{p}(t_i) - \boldsymbol{r}_\mathrm{p}(t_{i-1})|$. Taking sperm pair 3, for example (Figure 3.3E), there are 40 flagellar beat cycles. Compared with the experimentally observed displacement averaged over 40 flagellar beat cycles, $\langle d_\mathrm{obse} \rangle$, the predicted one, $\langle d_\mathrm{theo} \rangle$, in models

Figure 3.2: (*A*) The absolute values of the x-, y-, and z-components of the total hydrodynamic force on a sperm pair in models 1 (*i*), 2 (*ii*), and 3 (*iii*) are minimal compared to the absolute value of the total hydrodynamic force on cell 1 of this sperm pair, $|F_1|$. (*B*) The absolute values of the x-, y-, and z-components of the total hydrodynamic torque on the sperm pair in models 1 (*i*), 2 (*ii*), and 3 (*iii*) are minimal compared to the absolute value of the total hydrodynamic torque on cell 1 of this sperm pair, $|T_1|$. The force and torque components during a shorter time range, 0–0.1 s, are shown in the insets.

1, 2, and 3, is 0.2% shorter, 7.8% longer, and 11.7% longer, respectively. The predicted traveling distances of the pivot point averaged over the 40 beat cycles, $\langle S_{\text{theo}} \rangle$, in models 1, 2, and 3, are 32.1%, 29.4%, and 25.1%, respectively, shorter than the experimentally observed one, $\langle S_{\text{obse}} \rangle$.

In our experiments, the trajectory of the pivot point wiggles around its average path, resulting in the time-varying longitudinal and lateral displacement within one flagellar beat cycle. Our models predict the fine structure of the locomotion of the sperm pairs such as the wiggling. However, the agreement between the predicted and experimentally observed swimming trajectories varies significantly between the models. We quantify the agreement between the predicted and experimentally observed trajectories using Fréchet distance d_{Fr}, a lower value of which indicates a higher similarity [220]. Taking sperm pair 3, for example, compared with the experimentally observed swimming trajectory, d_{Fr} is 45.6, 56.6, and 21.1 µm for the predicted trajectory in models 1, 2, and 3, respectively. As shown in Figure 3.3*C*, compared with models 1 and 2, model 3 predicts a trajectory with higher similarity to the experimentally observed one, revealing the significant role of head oscillation in the swimming trajectory of sperm pairs. The improved prediction accuracy results from the available correct information, i.e., the head angular velocities.

3.6 Swimming Performances of Paired Spermatozoa

In our experiments, paired sperm cells beat their two flagella with the same period, exhibiting different modes of flagellar synchronization, as shown in Figure 3.4(*A*). To formalize the locomotion of the paired spermatozoa, the high-dimensional description of flagellar beating by Equation (3.1) can be further mapped to a low-dimensional space spanned by the first two shape scores β_1 and β_2 using principal component analysis [76], [81]. The points in the (β_1, β_2) space represent a series of flagellar shapes and form a closed loop (Figure 3.4*B*). We define a limit cycle of the beating of the ith flagellum by fitting the closed loop parametrized by a phase ϕ_i (Appendix 3.8.7). The flagellar phase ϕ_i is defined according to flagellar shape similarity such that it is independent of its time derivative, whereby a unique phase is assigned for each tracked flagellar shape [81]. Accordingly, a swimming

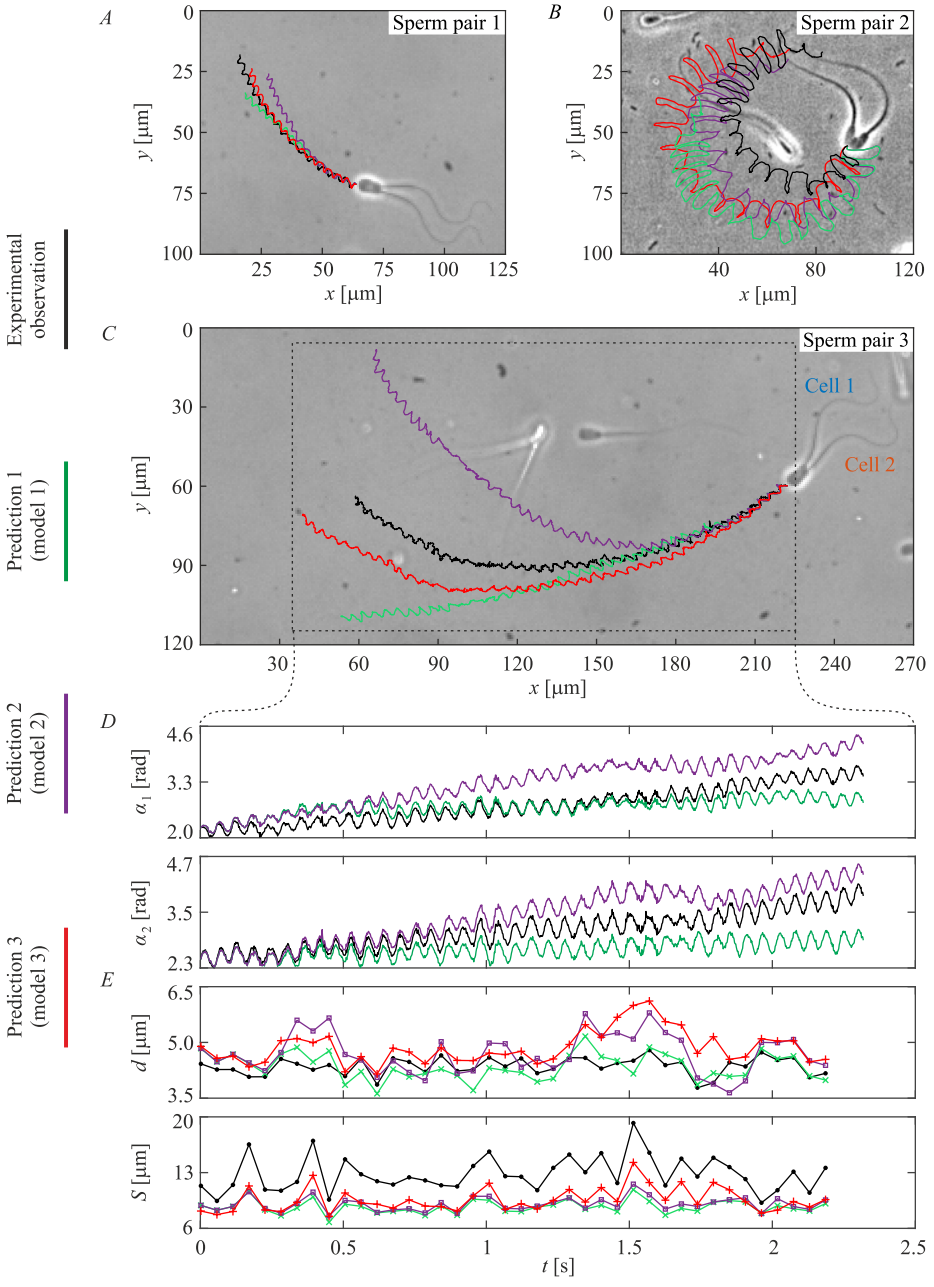

Figure 3.3: Experimentally observed and theoretically predicted locomotion of three sperm pairs.

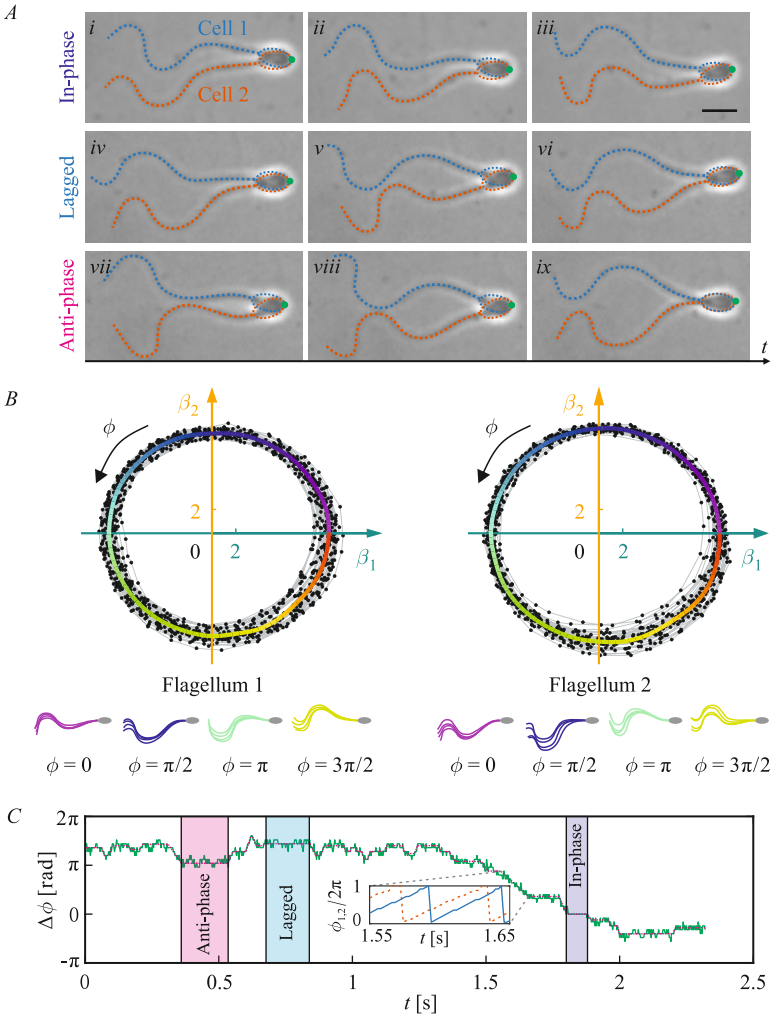

Figure 3.4: A swimming sperm pair was experimentally observed to exhibit three different modes of flagellar synchronization: in-phase, anti-phase, and lagged synchronization. (*A*) Interrupted by phase slips, the sperm pair transitioned between the modes of flagellar synchronization. Scale bar: 10 µm. (*B*) To characterize the flagellar beating, their shapes are mapped into a 2D space spanned by the first two shape scores β_1 and β_2. The phase of the flagellar beating is obtained through binning tracked flagellar shapes according to shape similarity. (*C*) The phase lag between the flagella of the sperm pair $\Delta\phi$ is unwrapped and clearly shows the phase lags, slips, and synchronization. Inset: the flagellar phases ϕ_1 and ϕ_2 during a time interval when phase slips occur.

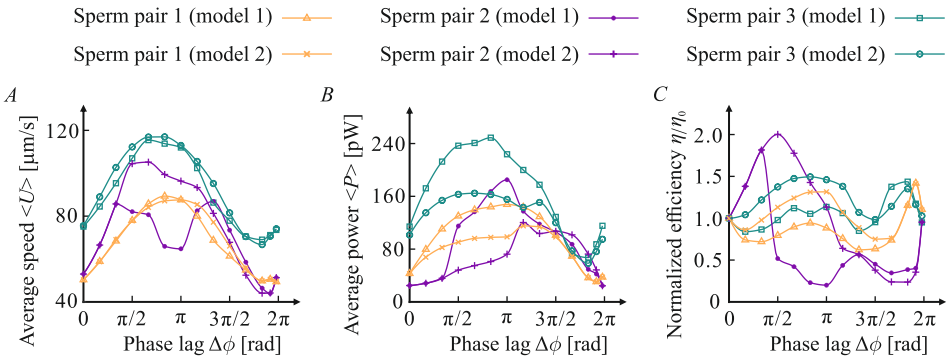

Figure 3.5: Three distinct sperm pairs respond differently to the flagellar phase lag $\Delta\phi$ in the average swimming speed $\langle U\rangle$ (A), swimming power $\langle P\rangle$ (B), and normalized swimming efficiency η/η_0 (C). Here, η_0 is the efficiency when $\Delta\phi = 0$. Models 1 and 2 are used to calculate $\langle U\rangle$, $\langle P\rangle$, and η/η_0 for each sperm pair. Each simulation includes 14 different values of flagellar phase lag $\Delta\phi$: 0, $\pi/6$, $\pi/3$, $\pi/2$, $2\pi/3$, $5\pi/6$, π, $7\pi/6$, $4\pi/3$, $3\pi/2$, $5\pi/3$, $11\pi/6$, $23\pi/12$, and $95\pi/48$.

sperm pair can be completely characterized with the position of the pivot point $\boldsymbol{r}_\mathrm{p}$, the orientation of the heads θ_i, and the phase of flagellar beating ϕ_i. The flagellar synchronization of paired cells is achieved when the phase lag between their flagellar beating $\Delta\phi = \phi_2 - \phi_1$ remains unchanged over one beat cycle. The sperm pairs were experimentally observed to maintain a constant flagellar phase lag $\Delta\phi$ for several beat cycles, followed by phase slips, and then establish another constant flagellar phase lag, as shown in Figure 3.4(C). This repeated process allowed the flagellar synchronization to transition between in-phase, anti-phase, and lagged synchronization.

Inspired by the experimental observations, we further numerically investigate the influence of the flagellar phase lag $\Delta\phi$ on the swimming of paired cells. Both models 1 and 2 are used in our simulations. In our simulations, the flagellar beat patterns are reconstructed from their limit cycles (Appendix 3.8.7). The phase-lag dependence of flagellar waveforms is neglected. We assess the swimming performances of sperm pairs regarding three parameters: average swimming speed $\langle U\rangle$, average power consumption $\langle P\rangle$, and swimming efficiency η. In our simulations, the three parameters are determined after the sperm pair has established regular beating, when its displacement during one flagellar beat cycle, d, stops varying between beat cycles. The average swimming speed over one beat cycle is determined by

$\langle U \rangle = d/T$, representing the swimming speed along the average path. Here, d is calculated using Equation (3.11). The average power consumption per cell $\langle P \rangle$ for a sperm pair is determined by averaging the instantaneous power of cells 1 and 2 over one beat cycle (Appendix 3.8.8). Compared to speed, swimming efficiency η may be more critical for spermatozoa due to their limited energy reserves. We define $\eta = \langle U \rangle^2 / \langle P \rangle$. This means that a longer swimming displacement per unit of energy consumption leads to higher efficiency. Given other conditions (e.g. the flagellar waveform due to the viscosity) unchanged, $\langle U \rangle$ is independent of fluid viscosity μ, whereas the average power $\langle P \rangle$ depends linearly on it, and η has an inverse dependence on it. To compare $\langle P \rangle$ and η at different fluid viscosities and various flagellar phase lags, we use $\mu = 1\,\mathrm{Pa\,s}$ in all our simulations for swimming performances, and normalize η with its value at $\Delta\phi = 0$, denoted by η_0.

In all our simulations for swimming performances, the period of flagellar beating is the same for the cells within a sperm pair, but distinct among the pairs. The flagellar waveform varies between the pairs. Therefore, sperm pairs with the same flagellar phase lag exhibit distinct swimming performances, as shown in Figure 3.5. In addition, a small variation in $\Delta\phi$ may lead the swimming performances to change significantly, especially for η/η_0 when the value of $\langle P \rangle$ is small. For instance, the value of η/η_0 for sperm pair 2 in model 1 significantly increases from 0.40 to 0.95 as $\Delta\phi$ increases from $23\pi/12$ to $95\pi/48$ (Figure 3.5*C*). In all our simulations for swimming performances, compared with the small flagellar phase lags (approximately 0 radians), large flagellar phase lags (approximately π radians) lead to a higher $\langle P \rangle$, which aligns with previous studies [72], [74]. However, a high swimming speed or efficiency does not necessarily result from flagellar phase lags close to π radians. For instance, in model 2, sperm pair 2 achieves its highest $\langle U \rangle$ and η/η_0 when its flagellar phase lag $\Delta\phi$ is close to $\pi/2$ radians. In addition, the swimming performances are influenced significantly by the mechanical head-head coupling. For the same sperm pair with the same $\Delta\phi$ but different head-head coupling, it may have a large difference in $\langle U \rangle$, $\langle P \rangle$, or η/η_0, as shown in Figure 3.5. Taking sperm pair 2, for example, when $\Delta\phi = \pi/3$, the value of $\langle U \rangle$ in model 1 is equal to that in model 2. But when $\Delta\phi = \pi/2$, the value of $\langle U \rangle$ for sperm pair 2 in model 1 diverges significantly from that in model 2. One reason is that the orientation difference between the heads $\Delta\theta(t)$ is constrained in model 2 such that $\Delta\theta(t) \geq 0$ for the whole course of swimming, whereas no such

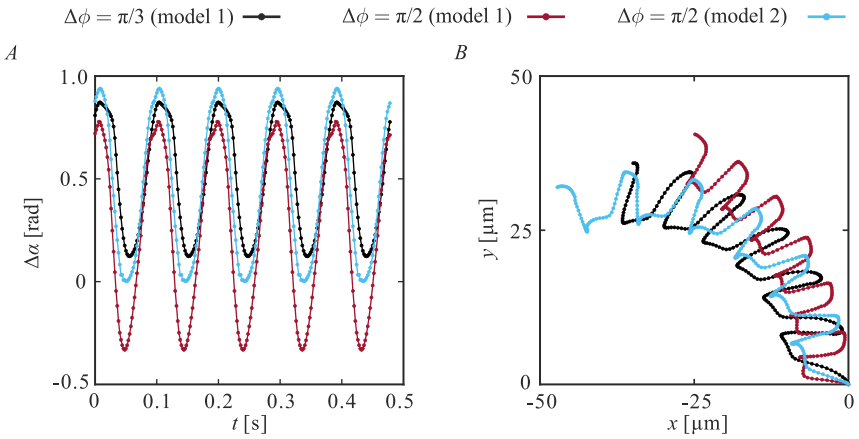

Figure 3.6: For sperm pair 2, its head orientation difference $\Delta\theta(t)$ (A) and its swimming trajectories (B) during five flagellar beat cycles are shown. When $\Delta\phi = \pi/3$, sperm pair 2 in models 1 and 2 has the same time-varying $\Delta\theta(t)$. When $\Delta\phi = \pi/2$, the head orientation difference $\Delta\theta(t)$ for sperm pair 2 in model 1 can be a negative value within a time interval, during which the relative oscillation of the heads of sperm pair 2 in model 2 are fused such that their relative angular speed is $\Delta\Omega = 0$.

constraint exists in model 1, as shown in Figure 3.6(A). This constraint in the relative head oscillation leads to different swimming trajectories, as shown in Figure 3.6(B). However, in our experiments, we did not observe the sperm pairs with their head orientation difference at $\Delta\theta(t) < 0$ during swimming. Therefore, steric force probably exists between the heads of the sperm pairs in the experiments, repelling each other.

Furthermore, the flagellar waveform also varies between the cells in the same sperm pair, resulting in a difference in the power $\langle P_1 \rangle$ and $\langle P_2 \rangle$, as shown in Figure 3.7. In our simulations, $\langle P \rangle$ for each sperm pair is always a positive value. But for sperm pair 2 in model 1, the average power for cell 1 is $\langle P_1 \rangle = -5.5\,\mathrm{pW}$ when $\Delta\phi = 23\pi/12$, as shown in Figure 3.7(B).

3.7 Discussions

The collective behaviours of mechanically and hydrodynamically coupled flagellated cells are complex and not fully understood. Here, using paired

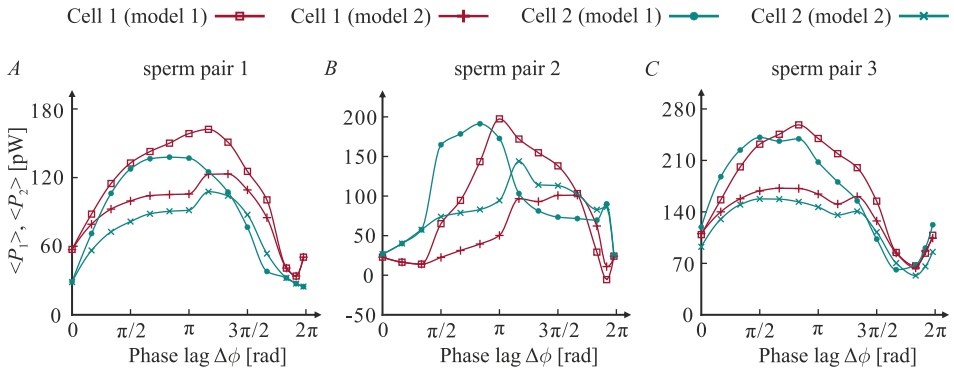

Figure 3.7: Sperm pair 1 (A), 2 (B), and 3 (C) are shown. Models 1 and 2 are used to calculate the average power consumption for cell 1 ($\langle P_1 \rangle$) and cell 2 ($\langle P_2 \rangle$) in each sperm pair. Each simulation includes 14 different values of flagellar phase lag $\Delta\phi$: 0, $\pi/6$, $\pi/3$, $\pi/2$, $2\pi/3$, $5\pi/6$, π, $7\pi/6$, $4\pi/3$, $3\pi/2$, $5\pi/3$, $11\pi/6$, $23\pi/12$, and $95\pi/48$.

bovine spermatozoa as an example, we develop hydrodynamic models to unveil more nuanced aspects of their locomotion. Compared to current theoretical models, our models offer some advantages for accurate predictions. First, our models include sperm heads, which are often missing in current models for attached or detached sperm cells [74], [125], [136]. In addition, we consider both the mechanical and hydrodynamic cell-cell interactions, whereas only one type of the interactions has typically been incorporated in current theoretical models [136], [164].

Our simulations show that the mechanical head-head coupling significantly affects the swimming trajectory of sperm pairs (Figures 3.3 and 3.6). The head orientations θ_1 and θ_2 are history-dependent, while the displacement d and traveling distance S are not. The time-dependent trajectory of paired spermatozoa is sensitive to the initial values of their head orientation, angular velocity, and translational velocity. A small variation in the initial values would lead to a significant cumulative error in the predicted trajectory. Comparing the predictions in the displacement during one beat cycle d with the experimentally observed ones, we find that both underpredictions and overpredictions appear in our simulations, depending on models and sperm pairs (Figure 3.3). In a previous computational study for single sperm cells, only underpredictions in d were found [86]. In our

simulations, the discrepancy in the displacement d between the predictions and experimental observations likely results from the missing information in the environment and flagella. For instance, we postulate that the sperm pairs swim in the middle plane between the walls, which may not align with reality. Closer proximity of sperm cells to the wall surface results in higher swimming speed [135]. Additionally, although our mathematical models treat flagellar beating as planar, it is not strictly planar in reality, particularly at the distal end of the flagellum. A slight tilt of the planar motion out of the swimming plane may contribute to the discrepancy. Another potential contributor is the missing information on whether sperm pairs come into contact with the chamber walls transiently.

Correct information, e.g. the time-varying angular velocities of heads, improves the accuracy in predicting the trajectory of sperm pairs. However, the underlying mechanism of the mechanical head-head coupling is not fully understood, limiting our prediction accuracy. The trajectory of each sperm pair during one beat cycle differs from that during another beat cycle. Such seemingly stochastic swimming has also been experimentally observed in individual sperm cells and is attributed to the active phase and amplitude fluctuations of flagellar beating [82]. In the case of paired spermatozoa, cell-cell interactions are another contributor. The combined effects of flagellar fluctuations and cell-cell interactions are also reflected in the radial distribution of the points around the closed loop (Figure 3.4B).

Three different modes of flagellar synchronization were observed in our experiments, reminiscent of the similar flagellar beat patterns found in *Chlamydomonas* [83], [221]–[223] and model microfilaments [224], [225]. Current models primarily focus on flagellar synchronization at a rigid/elastic base, using either low-order representations of flagella as oscillators [226]–[229] or more realistic representations as elastic beams [80], [204], [225], [230], [231]. In theoretical models for swimming flagella, their waveforms were typically prescribed as sinusoidal waves [70], [74]. In our models, flagellar waveforms are prescribed based on experimental observations, which is a more realistic representation but brings in some drawbacks, such as the exclusion of the phase-lag dependence of flagellar waveforms and the necessity for *a priori* information in flagellar beating.

The view prevails since Taylor [66] that co-swimming sperm cells tend to form in-phase synchronization to minimize the energy dissipation in the fluid. However, our results do not fully support this perspective. While in-

phase synchronization leads to relatively low power consumption, the minimum power can occur at a small flagellar phase lag due to the mechanical and hydrodynamic interactions (Figure 3.5). Similarly, a recent computational study on 2D co-swimming sheets has demonstrated that minimum power can occur at any flagellar phase lag, depending on the specific kinematics of the sheets [232]. Moreover, a recent study on swimming paired flagella has indicated that the anti-phase synchronization can induce the highest swimming speed and efficiency [74], which is also found in our calculations. However, our simulations show that the highest swimming speed and efficiency of paired spermatozoa can result from flagellar phase lags besides π radians. To further confirm the existence of a statistical relationship between the swimming performances of paired spermatozoa and their flagellar beat patterns, a larger sample size is required.

3.8 Appendix

3.8.1 Spatial Discretization of a Sperm Cell

In our models, the flagellum is discretized with cross-sections equally spaced along its length with a distance equal to its radius ρ. The cross-section is a circle. Six regularized Stokeslets are equally spaced along each circular cross-section, as illustrated in Figure 3.A1(A). The unit vectors $\boldsymbol{e}_1$ and $\boldsymbol{e}_2$ respectively align with the two principal axes of the ellipsoidal head, as illustrated in Figure 3.1. Let $\boldsymbol{e}_3$ denote the unit vector aligned with the third principal axis of the ellipsoidal head, where $\boldsymbol{e}_3 = \boldsymbol{e}_1 \times \boldsymbol{e}_2$, as illustrated in Figure 3.A1(B). The sperm head is discretized with n_h cross-sections along its long axis (i.e., the axis aligned with vector $\boldsymbol{e}_1$). These n_h cross-sections are perpendicular to $\boldsymbol{e}_1$ and divide the elliptical cross-section of the ellipsoid at the $(\boldsymbol{e}_1, \boldsymbol{e}_3)$ plane into arcs. These arcs have the same arc length of approximate ρ by adjusting the distance between the n_h cross-sections. In each of the n_h cross-sections, regularized Stokeslets are equally spaced at a distance of approximately ρ. To discretize the walls, regularized Stokeslets are distributed on each wall in a square pattern with a side length of 10ρ, as illustrated in Figure 3.A1(C).

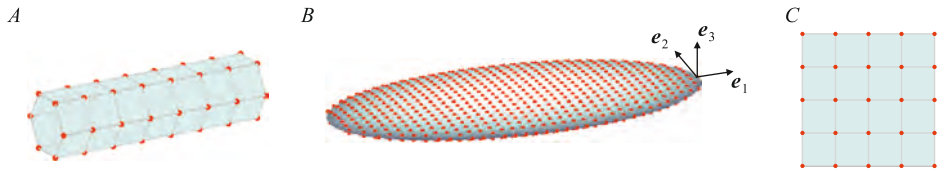

Figure 3.A1: Spatial discretization of the sperm flagellum (A), head (B), and wall (C). A portion of the flagellum and wall is shown.

3.8.2 Calculation of Hydrodynamic Forces on Paired Sperm Cells

For the total $n = n_1 + n_2 + n_\mathrm{w}$ regularized Stokeslets, the fluid response $\boldsymbol{u}$ at ${}^m\boldsymbol{r}$ to the hydrodynamic forces ${}^k\boldsymbol{f}$ is calculated by

$$\boldsymbol{u}\left({}^m\boldsymbol{r}\right) = -\frac{1}{8\pi\mu}\sum_{k=1}^{n}\sum_{p=1}^{3} S_{pq}^{\epsilon}\left({}^k\boldsymbol{r}, {}^m\boldsymbol{r}\right) {}^kT\, {}^k_p\boldsymbol{f}, \quad m = 1, 2, \cdots, n, \tag{3.12}$$

where ${}^kT$ is the quadrature weight of the kth regularized Stokeslets, ϵ is the regularization parameter, and ${}^k_p\boldsymbol{f}$ is the pth component of the force on the cells by the fluid [149].

3.8.3 Force Balance and Torque Balance on Each of the Paired Sperm Cells

As the adhesive force and hydrodynamic forces on cell 1 are balanced, we have

$$\begin{aligned}
\boldsymbol{C} &= \begin{bmatrix} {}^1\boldsymbol{C}_1 & {}^2\boldsymbol{C}_1 & \cdots & {}^{n_1}\boldsymbol{C}_1 & \boldsymbol{0}_{1\times 3(n_2+n_\mathrm{w})} \end{bmatrix}, \quad \boldsymbol{D} = \begin{bmatrix} 0 & 0 & 0 & 0 & -1 & 0 \end{bmatrix}, \\
\boldsymbol{E} &= \begin{bmatrix} {}^1\boldsymbol{E}_1 & {}^2\boldsymbol{E}_1 & \cdots & {}^{n_1}\boldsymbol{E}_1 & \boldsymbol{0}_{1\times 3(n_2+n_\mathrm{w})} \end{bmatrix}, \quad \boldsymbol{F} = \begin{bmatrix} 0 & 0 & 0 & 0 & 0 & -1 \end{bmatrix},
\end{aligned} \tag{3.13}$$

where ${}^k\boldsymbol{C}_1 = \begin{bmatrix} 1 & 0 & 0 \end{bmatrix}$, and ${}^k\boldsymbol{E}_1 = \begin{bmatrix} 0 & 1 & 0 \end{bmatrix}$, $k = 1, 2, \cdots, n_1$. The torques due to these forces on cell 1 are balanced about the origin of the laboratory frame, so we have

$$\begin{aligned}
\boldsymbol{G} &= \begin{bmatrix} {}^1\boldsymbol{G}_1 & {}^2\boldsymbol{G}_1 & \cdots & {}^{n_1}\boldsymbol{G}_1 & \boldsymbol{0}_{1\times 3(n_2+n_\mathrm{w})} \end{bmatrix}, \\
\boldsymbol{H} &= \begin{bmatrix} 0 & 0 & 0 & 0 & r_{\mathrm{p}y} & -r_{\mathrm{p}x} \end{bmatrix},
\end{aligned} \tag{3.14}$$

where ${}^k\boldsymbol{G}_1 = \begin{bmatrix} -{}^kr_{1y} & {}^kr_{1x} & 0 \end{bmatrix}$, $k = 1, 2, \cdots, n_1$. Here, ${}^kr_{1x}$ and ${}^kr_{1y}$ are the components of the position vector of the kth point on cell 1 along the

x- and y-axes of the laboratory frame, respectively. Likewise, $r_{\mathrm{p}x}$ and $r_{\mathrm{p}y}$ are the x- and y-components of $\boldsymbol{r}_{\mathrm{p}}$. Based on the force balance on cell 2, we have

$$\begin{aligned}\boldsymbol{I} &= \begin{bmatrix}\boldsymbol{0}_{1\times 3n_1} & {}^1\boldsymbol{I}_2 & {}^2\boldsymbol{I}_2 & \cdots & {}^{n_2}\boldsymbol{I}_2 & \boldsymbol{0}_{1\times 3n_{\mathrm{w}}}\end{bmatrix}, \qquad \boldsymbol{J} = \begin{bmatrix}0 & 0 & 0 & 0 & 1 & 0\end{bmatrix},\\ \boldsymbol{K} &= \begin{bmatrix}\boldsymbol{0}_{1\times 3n_1} & {}^1\boldsymbol{K}_2 & {}^2\boldsymbol{K}_2 & \cdots & {}^{n_2}\boldsymbol{K}_2 & \boldsymbol{0}_{1\times 3n_{\mathrm{w}}}\end{bmatrix}, \quad \boldsymbol{L} = \begin{bmatrix}0 & 0 & 0 & 0 & 0 & 1\end{bmatrix},\end{aligned} \tag{3.15}$$

where ${}^k\boldsymbol{I}_2 = \begin{bmatrix}1 & 0 & 0\end{bmatrix}$, and ${}^k\boldsymbol{K}_2 = \begin{bmatrix}0 & 1 & 0\end{bmatrix}$, $k = 1, 2, \cdots, n_2$. Based on the torque balance on cell 2 about the origin of the laboratory frame, we have

$$\begin{aligned}\boldsymbol{M} &= \begin{bmatrix}\boldsymbol{0}_{1\times 3n_1} & {}^1\boldsymbol{M}_2 & {}^2\boldsymbol{M}_2 & \cdots & {}^{n_2}\boldsymbol{M}_2 & \boldsymbol{0}_{1\times 3n_{\mathrm{w}}}\end{bmatrix},\\ \boldsymbol{N} &= \begin{bmatrix}0 & 0 & 0 & 0 & -r_{\mathrm{p}y} & r_{\mathrm{p}x}\end{bmatrix},\end{aligned} \tag{3.16}$$

where ${}^k\boldsymbol{M}_2 = \begin{bmatrix}-{}^kr_{2y} & {}^kr_{2x} & 0\end{bmatrix}$, $k = 1, 2, \cdots, n_2$. Here, ${}^kr_{2x}$ and ${}^kr_{2y}$ are the x- and y-components of the position vector of the kth point on cell 2, respectively.

3.8.4 Force Balance and Torque Balance on a Sperm Pair

As the forces on a sperm pair are balanced, we have

$$\begin{aligned}\boldsymbol{C}' &= \begin{bmatrix}{}^1\boldsymbol{C}'_1 & {}^2\boldsymbol{C}'_1 & \cdots & {}^{n_1}\boldsymbol{C}'_1 & {}^1\boldsymbol{C}'_2 & {}^2\boldsymbol{C}'_2 & \cdots & {}^{n_2}\boldsymbol{C}'_2 & \boldsymbol{0}_{1\times 3n_{\mathrm{w}}}\end{bmatrix}, \boldsymbol{D}' = \boldsymbol{0}_{1\times 3},\\ \boldsymbol{E}' &= \begin{bmatrix}{}^1\boldsymbol{E}'_1 & {}^2\boldsymbol{E}'_1 & \cdots & {}^{n_1}\boldsymbol{E}'_1 & {}^1\boldsymbol{E}'_2 & {}^2\boldsymbol{E}'_2 & \cdots & {}^{n_2}\boldsymbol{E}'_2 & \boldsymbol{0}_{1\times 3n_{\mathrm{w}}}\end{bmatrix}, \quad \boldsymbol{F}' = \boldsymbol{0}_{1\times 3},\end{aligned} \tag{3.17}$$

where ${}^k\boldsymbol{C}'_1 = \begin{bmatrix}1 & 0 & 0\end{bmatrix}$, and ${}^k\boldsymbol{E}'_1 = \begin{bmatrix}0 & 1 & 0\end{bmatrix}$, $k = 1, 2, \cdots, n_1$, with blocks ${}^k\boldsymbol{C}'_2 = \begin{bmatrix}1 & 0 & 0\end{bmatrix}$ and ${}^k\boldsymbol{E}'_2 = \begin{bmatrix}0 & 1 & 0\end{bmatrix}$, $k = 1, 2, \cdots, n_2$. The torques due to these forces on the sperm pair are balanced about the origin of the laboratory frame, so we have

$$\boldsymbol{G}' = \begin{bmatrix}{}^1\boldsymbol{G}'_1 & {}^2\boldsymbol{G}'_1 & \cdots & {}^{n_1}\boldsymbol{G}'_1 & {}^1\boldsymbol{G}'_2 & {}^2\boldsymbol{G}'_2 & \cdots & {}^{n_2}\boldsymbol{G}'_2 & \boldsymbol{0}_{1\times 3n_{\mathrm{w}}}\end{bmatrix}, \boldsymbol{H}' = \boldsymbol{0}_{1\times 3}, \tag{3.18}$$

where ${}^k\boldsymbol{G}'_1 = \begin{bmatrix}-{}^kr_{1y} & {}^kr_{1x} & 0\end{bmatrix}$, $k = 1, 2, \cdots, n_1$. Here, ${}^kr_{1x}$ and ${}^kr_{1y}$ are the components of the position vector of the kth point on cell 1 along the x- and y-axes of the laboratory frame, respectively, with blocks ${}^k\boldsymbol{G}'_2 = \begin{bmatrix}-{}^kr_{2y} & {}^kr_{2x} & 0\end{bmatrix}$, $k = 1, 2, \cdots, n_2$, where ${}^kr_{2x}$ and ${}^kr_{2y}$ are the components of the position vector of the kth point on cell 2 along the x- and y-axes of the laboratory frame, respectively.

3.8.5 Verification of the Spatial Discretization of Spermatozoa

Following the approach of Cortez et al. [149] and Gillies et al. [86], we choose an optimal regularized parameter ϵ by comparing our predictions of the resistive force on two isolated ellipsoids translating in the x- and y-directions in an unbounded fluid with their exact solution. The first ellipsoid has the same dimensions as the sperm head ($9\times5\times0.4\,\mu m$), and is discretized using the same method as for the sperm head. The resistive force on a tube is often approximated using the slender body theory [102], [233]. We represent the sperm flagellum with the second ellipsoid with an elongated needle-like geometry of $50\times0.25\times0.25\,\mu m$. The second ellipsoid is discretized using the same method as for the sperm flagellum. The non-dimensional resistive force error e_f is defined as

$$e_f = \sqrt{\frac{1}{n_c \zeta_{max}^2} \sum_{i=1}^{n_c} \zeta_i^2}, \tag{3.19}$$

with $\zeta_i = \zeta_{exact} - \zeta_{pred}$, where ζ_{exact} is the exact resistive force on the ellipsoids [104], and ζ_{pred} is our predicted resistive force on the ellipsoids. The number of the separate simulations $n_c = 4$, i.e., the two ellipsoids translating in the x- and y-directions. Here, ζ_{max} is the maximum value of $\zeta_i, i = 1, 2, 3, 4$. The force error is minimized when $\epsilon = 0.36\rho$, as illustrated in Figure 3.A2(A). Using $\epsilon = 0.36\rho$, we further calculate the velocity U_z of the points on an isolated sphere moving with a unit velocity along the z-axis in an unbounded fluid. This sphere has a volume equivalent to that of the sperm head, and is discretized into 682 points in the same manner as for the sperm head. Cumulative distribution of velocity error for the points $e_v = |U_z - 1|$ shows that all the points have a velocity error less than $0.018\,m/s$ (Figure 3.A2B). Note that the regularized parameter $\epsilon = 0.36\rho$ used here is to minimize the numerical error for the sperm head and flagellum moving in an unbounded fluid. Its value needs to be changed if walls are included.

3.8.6 Verification of the Regularized Parameter

In our test cases, $\xi = 0.5$ and $m = 0.9$ are chosen, which work well. Due to the lack of established convergence analysis for the regularized Stokeslets

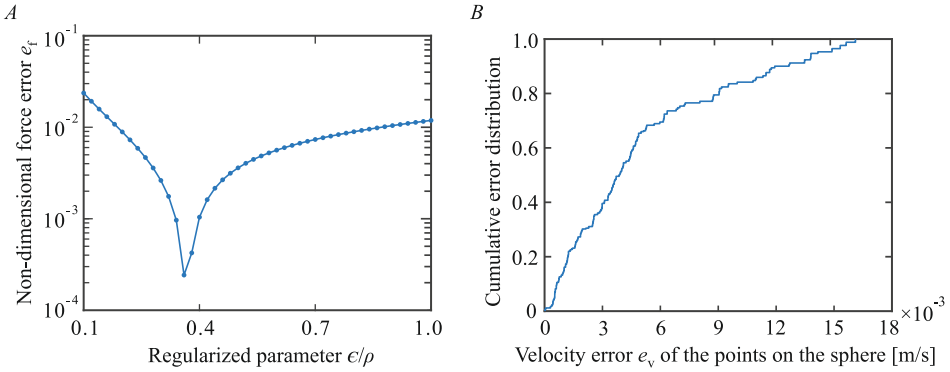

Figure 3.A2: (A) Resistive force error e_f for two isolated ellipsoids is dependent on the regularized paratmeter ϵ. (B) Cumulative distribution of the velocity error e_v for the points on the sphere.

method [150], we follow the approach of Ainley et al. [150] and Gillies et al. [86] and compare the predicted results in our test cases with published ones, as shown in Figure 3.A3. In our test cases, we calculate the resistive force $\boldsymbol{F}_\mathrm{s}$ on a sphere translating in the x- and y-directions between the walls with a velocity $\boldsymbol{U}_\mathrm{s}$. This sphere has a volume equivalent to that of the sperm head. The walls are perpendicular to the z-axis. The resistive force $\boldsymbol{F}$ on the sphere translating in an unbounded fluid with the same velocity $\boldsymbol{U}_\mathrm{s}$ is $\boldsymbol{F}_{\mathrm{s}\infty} = 6\pi\mu r_\mathrm{s}\boldsymbol{U}_\mathrm{s}$, where μ is the viscosity of the fluid. The ratio $F_\mathrm{s}/F_{\mathrm{s}\infty}$ depends on the ratio h/r_s. As shown in Figure 3.A3(A), our theoretical results agree with those of Ramia et al. [147] and Gillies et al. [86].

In addition, we calculate the normal resistance coefficient C_n and tangential resistance coefficient C_t of an isolated tube translating in the radial and longitudinal directions between the walls. The tube is parallel to the walls. The tube has dimensions identical to those of the sperm flagellum, and is discretized in the same manner as for the flagellum. The ratios $C_\mathrm{n}/C_\mathrm{t}$ and $C_\mathrm{t}/C_{\mathrm{t}\infty}$ depends on the ratio h/L, where $C_{\mathrm{t}\infty}$ is the tangential resistance coefficient of an isolated tube translating in an unbounded fluid, as shown in Figure 3.A3(B). Our theoretical results agree with those of Ramia et al. [147] and Gillies et al. [86]. Furthermore, as illustrated in Figure 3.A3(C,D), the wall size has only a slight impact on these ratios as long as the sphere and tube are covered by the walls. When the side

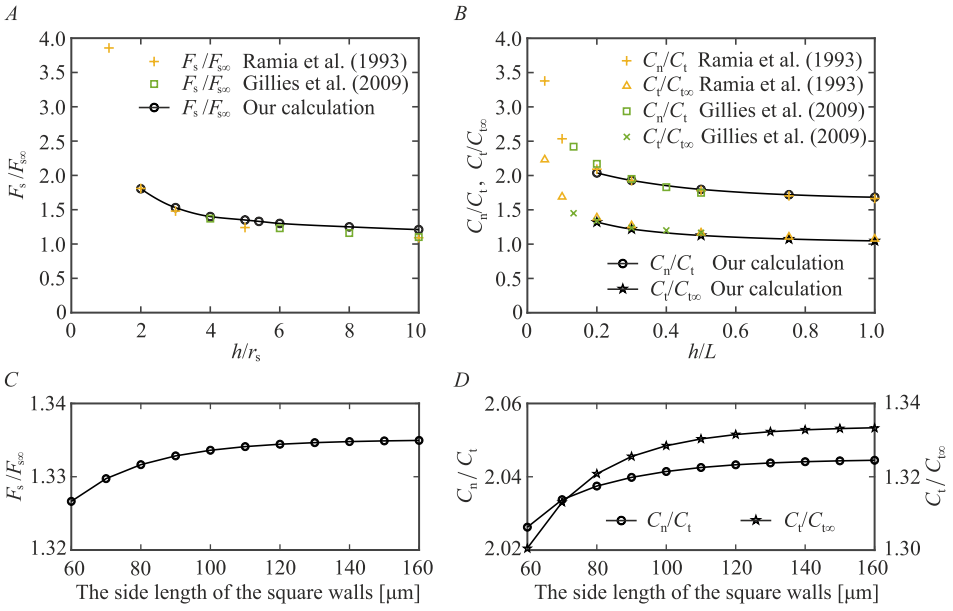

Figure 3.A3: (A) Compared to the resistive force $F_{s\infty}$ on the sphere translating in an unbounded fluid, it experiences a larger resistive force F_s when translating between the walls with the same velocity. (B) For the isolated tube parallel to the walls, its normal resistance coefficient C_n is larger than its tangential resistance coefficient C_t. The tube translating in an unbounded fluid has a smaller tangential resistance coefficient $C_{t\infty}$ than that when translating between the walls. Our predictions for $F_s/F_{s\infty}$ for the sphere (C) and C_n/C_t and $C_t/C_{t\infty}$ for the tube (D) are insensitive to the wall size.

length of the walls ranges from 60 to 160 μm, the maximum variations in $F_s/F_{s\infty}$ of the sphere are 0.6%, and the maximum variation in C_n/C_t and $C_t/C_{t\infty}$ of the tube are 0.9% and 2.5%, respectively. Note that several different values of the wall half-depth h are included in our test cases, but $h = 10\,\mu m$ is kept fixed for all our further simulations, as the depth of the chamber that we used is 20 μm.

3.8.7 Reconstruction of Flagellar Shapes and Their Limit Cycles

Using principal component analysis, we can approximate the tangent angle along each flagellum $\psi(l,t)$ as

$$\psi(l,t) \approx {}^0\psi(l) + \beta_1(t)\boldsymbol{V}_1(l) + \beta_2(t)\boldsymbol{V}_2(l) \tag{3.20}$$

where ${}^0\psi(l)$ is the mean tangent angle [76], [81]. Here, $\boldsymbol{V}_1$ and $\boldsymbol{V}_2$ are the first two flagellar shape modes, and β_1 and β_2 are their respective scores. This approximation accounts for 95% of the variance of the tangent angles. To reduce the noise of the tangent angles, we approximated the flagellar shapes using smoothing splines before calculating the shape modes.

The flagellar shapes at different times were thereby mapped to the (β_1, β_2) space, represented by the points in the space (Figure 3.4*B*). By fitting the points, we obtained the limit cycle. Flagellar phases were defined by binning flagellar shapes according to shape similarity. We then reconstructed flagellar tangent angles from the limit cycle. Finally, flagellar beat patterns with various phase lags were reconstructed from the tangent angles using Equation (3.1).

3.8.8 Calculation of Power Consumption

After a sperm pair has established regular beating in our simulations, the instantaneous power dissipated in the fluid by the ith sperm cell at a time t_j is determined by

$$P_i(t_j) = \sum_{k=1}^{n_i} \left({}^k\boldsymbol{f}_i(t_j) \cdot {}^k\boldsymbol{u}_i(t_j) \right), \tag{3.21}$$

where n_i is the number of the regularized Stokeslets points on the ith sperm cell. The force ${}^k\boldsymbol{f}_i$ and the velocity ${}^k\boldsymbol{u}_i$ are determined from Equations (3.7) or (3.10), depending on which model is used. The average power over one beat cycle for the ith cell is $\langle P_i \rangle = \sum_{j=1}^{n_t} P_i(t_j)/n_t$, where n_t is the number of time steps in this beat cycle. The average power per cell for the sperm pair is $\langle P \rangle = \sum_{i=1}^{2} \langle P_i \rangle /2$.

4

Conclusions and Outlook

Spermatozoa swimming behaviors and the associated dynamics are rich and complex. The preceding chapters in this doctoral thesis have revealed the sperm cooperative behavior, i.e. sperm pairing, from different perspectives. Specifically, **Chapters 2** and **3** have answered the research questions (**RQs. 1-4**) posed in **Chapter 1**. This last chapter of the doctoral thesis provides a summary of the preceding chapters and explores potential prospects for future research.

4.1 Conclusions

Chapter 2 experimentally observes the whole course of the transition from individual cells to bundles, providing us with details of the impact of sperm pairing on sperm swimming behaviors (**RQ. 1**) and the underlying dynamics during the transition (**RQ. 2**). Therefore, we can directly compare sperm cells in the far field–locking phase when the separate-but-close cells are influenced by hydrodynamic interactions, and in the steady-swimming phase when they are attached into a pair showing a regular flagellar beat pattern. The impact of sperm pairing differs between the low- and high-viscosity fluids. Nonetheless, smaller flagellar amplitude A_0 and longer wavelength λ due to sperm pairing are found in both fluids. We calculate the hydrodynamic forces of two sperm cells in the far field–locking phase using flagellar wave patterns reconstructed from experimental measurements. Similar to the predictions from some existing theoretical studies [69], [73], [108], [136], [157], [162], hydrodynamic attraction/repulsion

between the two cells is found, which depends on their flagellar wave patterns (characterized by mean flagellar curvature K_0, bending amplitude A_0, wavelength λ, and beat frequency ω), flagellar phase lag $\Delta\phi$, relative orientation between the sperm heads $\Delta\theta$. We find that closer proximity to the bottom boundary surface leads to greater hydrodynamic forces. In-phase flagellar synchronization and enhanced swimming speed are experimentally observed in the high-viscosity experiment, while neither in-phase flagellar synchronization nor enhanced swimming speed occurs in the low-viscosity experiment. The experimental results indicate that sperm pairing does not necessarily lead to enhanced swimming speed, consistent with Woolley's experimental observations [14]. Instead, enhanced swimming speed arises from an increased flagellar beat frequency induced by in-phase flagellar synchronization. In addition, the hydrodynamic and mechanical interactions between the sperm cells lead to fluctuations in the flagellar waveform (K_0, A_0 and λ), flagellar beat frequency ω, net swimming speed v_{n}, and the angle between the two heads of paired sperm cells $\Delta\theta$ across the transition course. Between the far field–locking phase and steady-swimming phase lies the rotational-oscillation phase, during which the heads of two sperm cells gradually align so that the angle between the heads $\Delta\theta$ approaches zero. Combining experimental and theoretical results, we find that the rotational dynamics of the sperm cells are influenced by fluid viscosity μ, flagellar phase lag $\Delta\phi$, and the initial angle between the heads $\Delta\theta_0$. Regardless of μ, $\Delta\phi$ or $\Delta\theta_0$, the angle between the heads $\Delta\theta$ approaches zero, indicating $\Delta\theta = 0$ is the stable equilibrium point.

The heads of a sperm pair are experimentally observed to oscillate relatively and pause for a while. The start and pause of the relative oscillation seem random. One interesting experimental finding in **Chapter 2** is that in-phase flagellar synchronization does not occur until the heads of a sperm pair stop rotating relatively. This behavior underscores the critical role of head-head attachment in sperm swimming. **Chapter 3** examines how head-head attachment and flagellar phase lag affect the swimming performances of paired spermatozoa, addressing **RQs. 3** and **4**. As the details of head-head coupling remain unknown, we consider two hypothetical head-head coupling cases. For the first case, we develop a 3D model (referred to as model 1), in which only adhesive forces exist between the heads so that the heads are attached and can relatively oscillate freely without any constraint. For the second case (i.e., model 2), both adhesive and steric

forces exist between the heads, so that the heads are attached and can relatively oscillate freely when $\Delta\theta > 0$, but are fused together without relatively oscillating when $\Delta\theta$ is near zero. To verify our models, we develop model 3 based on model 1 and compare the predicted swimming trajectories of sperm pairs with experimentally observed trajectories. The predictions agree with our experimental observations. The predicted trajectories in the three models clearly show the significant influence of the head-head coupling on the swimming trajectory of paired spermatozoa. Further, using models 1 and 2, we determine the swimming performances at various flagellar phase lags regarding average swimming speed $\langle U \rangle$, average power consumption $\langle P \rangle$, and swimming efficiency η. Our calculations suggest that the swimming performances are dependent on flagellar phase lag, flagellar waveforms, and the head-head coupling. One novel finding is the jumps in the values of $\langle U \rangle$, $\langle P \rangle$, or η induced by a slight variation in flagellar phase lag $\Delta\theta$, demonstrating the nonlinearity of the dynamics of paired spermatozoa.

4.2 Outlook

As stated at the beginning of the introduction of this doctoral thesis, spermatozoa have been an important discussion topic since at least ancient Greece, albeit those philosophers, such as Pythagoras and Aristotle, had only a primitive idea about spermatozoa in their times, which is apparently incorrect nowadays. During the past centuries, spermatozoa have been studied from various levels and perspectives by biologists, physicists, and engineers. Compared with individual sperm cells, sperm pairs receive much less investigation. Hitherto, this doctoral thesis has theoretically and experimentally unveiled the swimming behaviors of paired spermatozoa and their underlying dynamics, adding another piece to the jigsaw puzzle of spermatology. I believe that this thesis has uncovered just the tip of the iceberg of the underlying dynamics of sperm pairs/bundles. There remain some research challenges and vast unexplored areas. In this final section of the thesis, I would like to discuss the research challenges and the potential directions for further research.

4.2.1 Detection and Tracking of Bundled Spermatozoa

The automatic detection and tracking of paired spermatozoa remains a significant challenge, which has not been addressed completely in this thesis, where I developed a semi-automatic algorithm to do the detection and tracking. The typical flagellar beating frequency is 10 Hz. A minimum frame rate of approximately 200 Hz is required to obtain sufficiently accurate flagellar waveforms. For a 5 s long videomicroscopy of one sperm pair with a frame rate of 200 Hz, 2000 sperm images need to be processed. The data size is overwhelming for manual detection and tracking if more sperm pairs are involved, not to mention sperm bundles of multiple cells. An algorithm for automatically estimating sperm motility, CASA, was developed, which detects sperm heads, tracks them for a period, and then outputs their swimming trajectories [87]–[89]. However, CASA cannot detect time-varying flagellar shapes. Algorithms for automatically detecting flagellar shapes of individual sperm cells have been developed in recent years [80], [172]–[175], [234]. Automatic detection and tracking of the biflagellated *Chlamydomonas* was also reported [81]. Nevertheless, no reliable algorithms for detecting sperm pairs/bundles have been reported. For sperm pairs/bundles, their flagella overlap each other quite often, and their heads are stacked, disabling the aforementioned algorithms, which are based on detecting the features of sperm images.

Artificial intelligence (AI) has shown its huge power in image processing. Deep-learning models have shown good accuracy in tracking the position of the heads of individual sperm cells, based on open datasets such as Sperm Videos and Images Analysis (SVIA) [235], Multi-Species Dataset (MSD) [236], VISEM [237], and VISEM-Tracking [238]. Deep-learning models have also been developed for the morphological classification of individual sperm cells, using open datasets such as Human Sperm Morphology Analysis DataSet (HSMA-DS) [239], Modified Human Sperm Morphology Analysis (MHSMA) [240], Human Sperm Head Morphology (HuSHeM) [241], Sperm Morphology Image Data Set (SMIDS) [242], and SCIANLab's Gold-Standard for Morphological Sperm Analysis (SCIAN-MorphoSpermGS) [243]. Despite no AI models released yet for detecting and tracking the flagella or heads of sperm pairs/bundles, deep-learning models show great promise for this task. The lack of datasets is the first problem in developing such deep-learning models.

The aforementioned sperm imaging methods are usually based on 2D bright-field microscopy. Improving the imaging quality would certainly increase the accuracy of the detection and tracking of paired sperm cells, regardless of whether conventional image analysis methods or AI models are used. Among various cell imaging methods, techniques such as tomographic phase microscopy [101] and holographic phase microscopy [244] offer more 3D spatial information about sperm cells, perhaps making them better at imaging sperm pairs/bundles. Other potentially suitable imaging methods include the use of a rapidly oscillating objective [245], [246], as well as combining event cameras and an unsupervised learning model [247].

4.2.2 Flagellar Synchronization

Flagellar synchronization has been observed in many microorganisms and cells, such as spermatozoa [14], *Chlamydomonas* [248], *Paramecium* [249], epithelia of vertebrate [250]. Despite many studies, flagellar synchronization offers vast space to explore. In **Chapter 2**, we experimentally observe in-phase flagella synchronization. In **Chapter 3**, we further experimentally observe in-phase, anti-phase, and lagged flagellar synchronization, and the transition between the three modes. We have investigated the influence of phase lag on the swimming performances. Nonetheless, we neglect the phase-lag dependence of flagellar waveforms, and do not delve into the underlying mechanisms of the emergence of the different modes of sperm flagellar synchronization and the transition between the modes, which perhaps need to be interpreted from the molecular mechanisms of flagellar beating.

The fine structures of sperm flagella have been clearly revealed by cryo-electron tomography [251], whereas their interactions are not fully understood. The dynamic models for flagella are often based on hypothesized molecular mechanisms, such as the geometric clutch [252], [253], curvature control [254]–[258], and sliding control models [80], [124], [126], [183], [259]–[262]. The results from these three mechanisms often contradict, necessitating a deeper understanding of the mechanism of the coordinated activity of dyneins and their interactions with other passive components, e.g. axonemal nexins and radial spokes.

4.2.3 A Comprehensive Dynamic Model of Sperm Bundles

Thigmotaxis, a sperm swimming behavior characterized by the tendency of sperm cells to accumulate near solid boundaries, is observed in our experiments and allows us to consider only the planar sperm kinematics in the 3D space, simplifying our experiments and the development of dynamic models of sperm pairs. Nevertheless, sperm cells are not always inclined to accumulate near solid boundaries, particularly when hyperactivated to show helical flagellar beats and 3D swimming trajectories. Previous models for multiple separate sperm cells have uncovered their hydrodynamic interactions [73], [136]. Nonetheless, a fully 3D dynamic model for sperm pairs/bundles is lacking, and is challenging to develop. Taking our models in **Chapter 3** for example, the models can be adapted to account for fully 3D locomotion of sperm pairs; however, the linear equation systems would turn non-linear, as the pitch, yaw, and roll motions of a sperm cell/pair in the 3D space are coupled, leaving the equations quite difficult to solve. Not only modeling but also imaging and image analysis face challenges due to the 3D locomotion of sperm cells.

The head-head coupling is largely uninvestigated. In **Chapter 3**, we hypothesize two potential cases of head-head coupling, which simplifies the real situation and may be incorrect. However, no matter Woolley's experimental observations [14], Simons' numerical simulations [125], our experimental observations in **Chapter 2**, or our simulations in **Chapter 3** suggest the essential role of head-head coupling in sperm swimming. Hence, the head-head coupling should be further investigated from both biological and physical perspectives. Moreover, the underlying mechanisms of the occurrence of head-head attachment remain elusive, which is also a challenging research project.

The mammal female reproductive tract is filled with physiological fluids, like cervical mucus and oviductal fluids. Compared with the Newtonian media in our *in vitro* experiments, the physiological fluids usually are non-Newtonian, showing distinct properties. For instance, Purcell's scallop theorem does not hold for shear-thickening or shear-thinning fluids due to the nonlinear relationship between stress and strain rate [263], [264]. The swimming speed of Taylor's sheet depends nonlinearly on the wave frequency in a viscoelastic fluid [265]. The non-Newtonian properties of fluids have been incorporated into some simple models of 2D swimming sheets

[70], [266], but not yet for sperm pairs or bundles.

In a nutshell, accurately simulating the dynamics of sperm pairs/bundles requires a comprehensive model that incorporates the 3D kinematics of sperm pairs/bundles, the flagellar elastodynamics, the hydrodynamic interactions between the cells, the mechanical interaction between the heads, and properties of physiological fluids, although there is a long way to achieve this objective.

4.2.4 Applications to Microrobots

As mentioned in the introduction of this thesis, one of the motivations of my research is to facilitate the development of biomedical technologies, such as microrobots for drug delivery. There are several actuation methods for microrobots. One of the most promising methods is the magnetic field, whose advantages over other methods include high controllability, non-toxicity and large penetration depth to biological tissues. In this section, I specifically focus on sperm-like magnetic microrobots and give some general suggestions on their development. The suggestions are general and do not entail technical details.

Sperm-template [24], sperm-hybrid [267], [268], sperm-inspired microrobots [269], [270] actuated by magnetic fields have been developed. These microrobots have flexible tails and are easier to pass through confined environments with adaptive locomotion. However, their propulsive force and maximum swimming speed are sometimes too low to overcome the fluid flow. **Chapter 2** infers that the propulsive force and maximum swimming speed would probably increase if the sperm-like microrobots adhere to bundles due to the disproportionate increase in viscous and propulsive forces. To actuate a pair of attached sperm-like microrobots with faster swimming speed, anti-phase propagating waveforms may be favored over in-phase propagating waveforms, as inferred from **Chapter 3**. Additionally, effective therapy requires a minimum drug dose, necessitating the actuation and control of microrobot swarms. One technical challenge is the selective control of the sperm-like microrobot swarms in a uniform magnetic field so they can have different swimming trajectories. To address this technical problem, two potential strategies can be inferred from **Chapters 2** and **3**. First, the sperm-like microrobots with different propagating waveforms would exhibit distinct swimming trajectories. By switching between being

attached and detached, the sperm-like microrobots could also exhibit distinct swimming trajectories in a uniform magnetic field. Of course, there are some other methods to realize selective control of microrobots, such as using the magnetic gradient field and using local magnetic fields [271]. Microrobotics has advanced rapidly over the past decades and encompasses substantial technical details, so that a task may be realized through various technical solutions. The preceding suggestions are not limited to sperm-like microrobots but may also be applied to bio-inspired microrobot swarms for functions such as drug delivery and assisted reproduction.

Nevertheless, applying the suggestions to microrobots also probably gives rise to more engineering problems. The results presented in **Chapters 2** and **3** are derived from active flagellar waveforms and thus may be inapplicable to the sperm-like microrobots, which are typically propelled by passively propagating waves. But, one of the charms of engineering is that when working on it, unforeseen problems always arise. So I would like to stop envisioning the technical details and conclude this thesis here, and leave the exploration of the engineering challenges to prospective readers or my future self.

Bibliography

[1] K. Drescher, J. Dunkel, L. H. Cisneros, S. Ganguly, and R. E. Goldstein, "Fluid dynamics and noise in bacterial cell-cell and cell-surface scattering," *Proceedings of the National Academy of Sciences*, vol. 108, no. 27, pp. 10940–10945, 2011.

[2] K. Bente, S. Mohammadinejad, M. A. Charsooghi, F. Bachmann, A. Codutti, C. T. Lefèvre, S. Klumpp, and D. Faivre, "High-speed motility originates from cooperatively pushing and pulling flagella bundles in bilophotrichous bacteria," *eLife*, vol. 9, p. e47551, 2020.

[3] J. Najafi, M. R. Shaebani, T. John, F. Altegoer, G. Bange, and C. Wagner, "Flagellar number governs bacterial spreading and transport efficiency," *Science Advances*, vol. 4, no. 9, p. eaar6425, 2018.

[4] A. G. Prabhune, A. S. García-Gordillo, I. S. Aranson, T. R. Powers, and N. Figueroa-Morales, "Bacteria navigate anisotropic media using a flagellar tug-of-oars," *PRX Life*, vol. 2, no. 3, p. 033004, 2024.

[5] K. Wan, "Biophysics of protist behaviour," *Current Biology*, vol. 34, pp. R981–R986, 2024.

[6] T. Kiørboe, "Predation in a microbial world: Mechanisms and trade-offs of flagellate foraging," *Annual Review of Marine Science*, vol. 16, pp. 361–381, 2024.

[7] H. Machemer and R. Eckert, "Electrophysiological Control of Reversed Ciliary Beating in Paramecium ," *Journal of General Physiology*, vol. 61, no. 5, pp. 572–587, 1973.

[8] A. Hamel, C. Fisch, L. Combettes, P. Dupuis-Williams, and C. N. Baroud, "Transitions between three swimming gaits in paramecium escape," *Proceedings of the National Academy of Sciences*, vol. 108, no. 18, pp. 7290–7295, 2011.

[9] R. Brette, "Integrative neuroscience of paramecium, a 'swimming neuron'," *eNeuro*, vol. 8, no. 3, 2021.

[10] H. C. Berg and D. A. Brown, "Chemotaxis in escherichia coli analysed by three-dimensional tracking," *Nature*, vol. 239, no. 5374, pp. 500–504, 1972.

[11] D. Ralt, M. Manor, A. Cohen-Dayag, I. Tur-Kaspa, I. Ben-Shlomo, A. Makler, I. Yuli, J. Dor, S. Blumberg, S. Mashiach, and M. Eisenbach, "Chemotaxis and chemokinesis of human spermatozoa to follicular factors1," *Biology of Reproduction*, vol. 50, no. 4, pp. 774–785, 1994.

[12] M. V. Inamdar, T. Kim, Y.-K. Chung, A. M. Was, X. Xiang, C.-W. Wang, S. Takayama, C. M. Lastoskie, F. I. M. Thomas, and A. M. Sastry, "Assessment of sperm chemokinesis with exposure to jelly coats of sea urchin eggs and resact: a microfluidic experiment and numerical study," *Journal of Experimental Biology*, vol. 210, no. 21, pp. 3805–3820, 2007.

[13] M. Zaferani and A. Abbaspourrad, "Biphasic chemokinesis of mammalian sperm," *Physical Review Letter*, vol. 130, no. 24, p. 248401, 2023.

[14] D. M. Woolley, R. F. Crockett, W. D. I. Groom, and S. G. Revell, "A study of synchronisation between the flagella of bull spermatozoa, with related observations," *Journal of Experimental Biology*, vol. 212, no. 14, pp. 2215–2223, 2009.

[15] P. Morcillo i Soler, C. Hidalgo, Z. Fekete, L. Zalanyi, I. Khalil, M. Yeste, and V. Magdanz, "Bundle formation of sperm: Influence of environmental factors," *Frontiers in Endocrinology*, vol. 13, p. 957684, 2022.

[16] S. Xiao, J. Riordon, A. Lagunov, M. Ghaffarzadeh, T. Hannam, R. Nosrati, and D. Sinton, "Human sperm cooperate to transit highly viscous regions on the competitive pathway to fertilization," *Communications Biology*, vol. 6, p. 495, 2023.

[17] D. J. Funk, J. E. Parrillo, and A. Kumar, "Sepsis and septic shock: A history," *Critical Care Clinics*, vol. 25, no. 1, pp. 83–101, 2009. Historical Aspects of Critical Care Illness and Critical Care Medicine.

[18] A. Bahat, I. Tur-Kaspa, A. Gakamsky, L. Giojalas, H. Breitbart, and M. Eisenbach, "Thermotaxis of mammalian sperm cells: A potential navigation mechanism in the female genital tract," *Nature Medicine*, vol. 9, pp. 149–150, 2003.

[19] S. Boryshpolets, S. Pérez-Cerezales, and M. Eisenbach, "Behavioral mechanism of human sperm in thermotaxis: a role for hyperactivation," *Human Reproduction*, vol. 30, no. 4, pp. 884–892, 2015.

[20] T.-K. Huang, C.-H. Huang, P.-A. Chen, C. H. Chen, F. Lu, W.-J. Yang, J. Y. J. Huang, and B.-R. Li, "Development of a thermotaxis and rheotaxis microfluidic device for motile spermatozoa sorting," *Biosensors and Bioelectronics*, vol. 258, p. 116353, 2024.

[21] J. Gai, E. Dervisevic, C. Devendran, V. J. Cadarso, M. K. O'Bryan, R. Nosrati, and A. Neild, "High-frequency ultrasound boosts bull and human sperm motility," *Advanced Science*, vol. 9, no. 11, p. 2104362, 2022.

[22] N. A. P. Mariani, J. V. Silva, M. Fardilha, and E. J. R. Silva, "Advances in non-hormonal male contraception targeting sperm motility," *Human Reproduction Update*, vol. 29, no. 5, pp. 545–569, 2023.

[23] A. Vafaie, M. R. Raveshi, C. Devendran, R. Nosrati, and A. Neild, "Making immotile sperm motile using high-frequency ultrasound," *Science Advances*, vol. 10, no. 7, p. eadk2864, 2024.

[24] V. Magdanz, I. S. Khalil, J. Simmchen, G. P. Furtado, S. Mohanty, J. Gebauer, H. Xu, A. Klingner, A. Aziz, M. Medina-Sánchez, *et al.*, "IRONSperm: Sperm-templated soft magnetic microrobots," *Science Advances*, vol. 6, no. 28, p. eaba5855, 2020.

[25] C. Schmidt, M. Medina-Sánchez, R. Edmondson, and O. Schmidt, "Engineering microrobots for targeted cancer therapies from a medical perspective," *Nature Communications*, vol. 11, p. 5618, 2020.

[26] B. J. Nelson and S. Pané, "Delivering drugs with microrobots," *Science*, vol. 382, no. 6675, pp. 1120–1122, 2023.

[27] Q. Wang, Q. Wang, Z. Ning, K. F. Chan, J. Jiang, Y. Wang, L. Su, S. Jiang, B. Wang, B. Y. M. Ip, H. Ko, T. W. H. Leung, P. W. Y.

Chiu, S. C. H. Yu, and L. Zhang, "Tracking and navigation of a microswarm under laser speckle contrast imaging for targeted delivery," *Science Robotics*, vol. 9, no. 87, p. eadh1978, 2024.

[28] Z. Carvalho-Santos, J. Azimzadeh, J. B. Pereira-Leal, and M. Bettencourt-Dias, "Tracing the origins of centrioles, cilia, and flagella," *Journal of Cell Biology*, vol. 194, no. 2, pp. 165–175, 2011.

[29] E. Gaino and M. Mazzini, "Aflagellate sperm in three species of leptophlebiidae (ephemeroptera)," *International Journal of Insect Morphology and Embryology*, vol. 20, no. 3, pp. 119–125, 1991.

[30] A. Darszon, T. Nishigaki, I. López-González, P. E. Visconti, and C. L. Treviño, "Differences and similarities: The richness of comparative sperm physiology," *Physiology*, vol. 35, no. 3, pp. 196–208, 2020. PMID: 32293232.

[31] E. Lauga and T. R. Powers, "The hydrodynamics of swimming microorganisms," *Reports on Progress in Physics*, vol. 72, no. 9, p. 096601, 2009.

[32] E. M. Purcell, "Life at low Reynolds number," *American Journal of Physics*, vol. 45, no. 1, pp. 3–11, 1977.

[33] Z. Qu, F. Z. Temel, R. Henderikx, and K. S. Breuer, "Changes in the flagellar bundling time account for variations in swimming behavior of flagellated bacteria in viscous media," *Proceedings of the National Academy of Sciences*, vol. 115, no. 8, pp. 1707–1712, 2018.

[34] R. R. Bennett and R. Golestanian, "Emergent run-and-tumble behavior in a simple model of chlamydomonas with intrinsic noise," *Physical Review Letter*, vol. 110, no. 14, p. 148102, 2013.

[35] A. Marumo, M. Yamagishi, and J. Yajima, "Three-dimensional tracking of the ciliate tetrahymena reveals the mechanism of ciliary stroke-driven helical swimming," *Communications Biology*, vol. 4, p. 1209, 2021.

[36] G. Lott, *Zur anatomie und physiologie des cervix uteri.* Stuttgart, Germany: Ferdinand Enke, 1872.

[37] K. Miki and D. Clapham, "Rheotaxis guides mammalian sperm," *Current Biology*, vol. 23, no. 6, pp. 443–452, 2013.

[38] V. Kantsler, J. Dunkel, M. Blayney, and R. E. Goldstein, "Rheotaxis facilitates upstream navigation of mammalian sperm cells," *eLife*, vol. 3, p. e02403, 2014.

[39] T. Hyakutake, D. Higashiyama, and T. Tsuchiya, "Prediction of sperm motion behavior in microfluidic channel using sperm swimming model," *Journal of Biomechanics*, vol. 176, p. 112336, 2024.

[40] S. Pérez-Cerezales, S. Boryshpolets, and M. Eisenbach, "Behavioral mechanisms of mammalian sperm guidance," *Asian Journal of Andrology*, vol. 17, no. 4, pp. 628–632, 2015.

[41] M. Eisenbach and L. Giojalas, "Sperm guidance in mammals — an unpaved road to the egg," *Nature Reviews Molecular Cell Biology*, vol. 7, pp. 276–285, 2006.

[42] U. B. Kaupp, N. D. Kashikar, and I. Weyand, "Mechanisms of sperm chemotaxis," *Annual Review of Physiology*, vol. 70, pp. 93–117, 2008.

[43] B. M. Friedrich and F. Jülicher, "Chemotaxis of sperm cells," *Proceedings of the National Academy of Sciences*, vol. 104, no. 33, pp. 13256–13261, 2007.

[44] J. Jikeli, L. Alvarez, B. Friedrich, L. Wilson, R. Pascal, R. Colin, M. Pichlo, A. Rennhack, C. Brenker, and U. Kaupp, "Sperm navigation along helical paths in 3d chemoattractant landscapes," *Nature Communications*, vol. 6, p. 7985, 2015.

[45] H. V. Ramírez-Gómez, I. Tuval, A. Guerrero, and A. Darszon, "Chapter 21 - analysis of sperm chemotaxis," in *Echinoderms, Part B* (A. Hamdoun and K. R. Foltz, eds.), vol. 151 of *Methods in Cell Biology*, pp. 473–486, Academic Press, 2019.

[46] H. V. Ramírez-Gómez, V. Jimenez Sabinina, M. Velázquez Pérez, C. Beltran, J. Carneiro, C. D. Wood, I. Tuval, A. Darszon, and A. Guerrero, "Sperm chemotaxis is driven by the slope of the chemoattractant concentration field," *eLife*, vol. 9, p. e50532, 2020.

[47] H. Guidobaldi, M. Cubilla, A. Moreno, M. Molino, L. Bahamondes, and L. Giojalas, "Sperm chemorepulsion, a supplementary mechanism to regulate fertilization," *Human Reproduction*, vol. 32, no. 8, pp. 1560–1573, 2017.

[48] R. Lottero-Leconte, C. A. I. Alonso, L. Castellano, and S. P. Martinez, "Mechanisms of the sperm guidance, an essential aid for meeting the oocyte," *Translational Cancer Research*, vol. 6, no. Suppl 2, 2017.

[49] P. Denissenko, V. Kantsler, D. J. Smith, and J. Kirkman-Brown, "Human spermatozoa migration in microchannels reveals boundary-following navigation," *Proceedings of the National Academy of Sciences*, vol. 109, no. 21, pp. 8007–8010, 2012.

[50] A. Li, Y.-X. Luo, Y. Liu, Y.-q. Xu, F.-B. Tian, and Y. Wang, "Hydrodynamic behaviors of self-propelled sperms in confined spaces," *Engineering Applications of Computational Fluid Mechanics*, vol. 16, pp. 141–160, 2022.

[51] N. Ahmadkhani, M. Saadatmand, S. Kazemnejad, and M. Abdekhodaie, "Qualified sperm selection based on the rheotaxis and thigmotaxis in a microfluidic system," *Biomedical Engineering Letters*, vol. 13, pp. 671–680, 2023.

[52] C.-K. Tung, C. Lin, B. Harvey, A. Fiore, F. Ardón, M. Wu, and S. Suarez, "Fluid viscoelasticity promotes collective swimming of sperm," *Scientific Reports*, vol. 7, p. 3152, 2017.

[53] T. Hyakutake, K. Sato, and K. Sugita, "Study of bovine sperm motility in shear-thinning viscoelastic fluids," *Journal of Biomechanics*, vol. 88, pp. 130–137, 2019.

[54] M. Zaferani, S. H. Cheong, and A. Abbaspourrad, "Rheotaxis-based separation of sperm with progressive motility using a microfluidic corral system," *Proceedings of the National Academy of Sciences*, vol. 115, no. 33, pp. 8272–8277, 2018.

[55] A. Heydari, M. Zabetian, I. Halvaei, and R. Nosrati, "A novel microfluidic device with parallel channels for sperm separation using

spermatozoa intrinsic behaviors," *Scientific Reports*, vol. 13, p. 1185, 2023.

[56] L. C. Giojalas and H. A. Guidobaldi, "Getting to and away from the egg, an interplay between several sperm transport mechanisms and a complex oviduct physiology," *Molecular and Cellular Endocrinology*, vol. 518, p. 110954, 2020.

[57] R. Nosrati, P. Graham, Q. Liu, and D. Sinton, "Predominance of sperm motion in corners," *Scientific Reports*, vol. 6, p. 26669, 2016.

[58] M. Raveshi, M. S. Abdul Halim, S. Agnihotri, M. O'Bryan, A. Neild, and R. Nosrati, "Curvature in the reproductive tract alters sperm-surface interactions," *Nature Communications*, vol. 12, p. 3446, 2021.

[59] H. Ho and S. Suarez, "Hyperactivation of mammalian spermatozoa: function and regulation," *Reproduction*, vol. 122, no. 4, pp. 519–526, 2001.

[60] S. Suarez and H.-C. Ho, "Hyperactivated motility in sperm," *Reproduction in Domestic Animals*, vol. 38, no. 2, pp. 119–124, 2003.

[61] S. G. Goodson, Z. Zhang, J. K. Tsuruta, W. Wang, and D. A. O'Brien, "Classification of mouse sperm motility patterns using an automated multiclass support vector machines model1," *Biology of Reproduction*, vol. 84, no. 6, pp. 1207–1215, 2011.

[62] E. H. Ooi, D. J. Smith, H. Gadêlha, E. A. Gaffney, and J. Kirkman-Brown, "The mechanics of hyperactivation in adhered human sperm," *Royal Society Open Science*, vol. 1, no. 2, p. 140230, 2014.

[63] S. S. Suarez, "Control of hyperactivation in sperm," *Human Reproduction Update*, vol. 14, no. 6, pp. 647–657, 2008.

[64] T.-W. Su, L. Xue, and A. Ozcan, "High-throughput lensfree 3D tracking of human sperms reveals rare statistics of helical trajectories," *Proceedings of the National Academy of Sciences*, vol. 109, no. 40, pp. 16018–16022, 2012.

[65] R. Nosrati, A. Driouchi, C. Yip, and D. Sinton, "Two-dimensional slither swimming of sperm within a micrometre of a surface," *Nature Communications*, vol. 6, p. 8703, 2015.

[66] G. I. Taylor, "Analysis of the swimming of microscopic organisms," *Proceedings of the Royal Society of London. Series A. Mathematical and Physical Sciences*, vol. 209, no. 1099, pp. 447–461, 1951.

[67] E. Lauga, "Propulsion in a viscoelastic fluid," *Physics of Fluids*, vol. 19, no. 8, p. 083104, 2007.

[68] G. J. Elfring and E. Lauga, "Hydrodynamic phase locking of swimming microorganisms," *Physical Review Letter*, vol. 103, no. 8, p. 088101, 2009.

[69] S. D. Olson and L. J. Fauci, "Hydrodynamic interactions of sheets vs filaments: Synchronization, attraction, and alignment," *Physics of Fluids*, vol. 27, no. 12, p. 121901, 2015.

[70] G. J. Elfring, O. S. Pak, and E. Lauga, "Two-dimensional flagellar synchronization in viscoelastic fluids," *Journal of Fluid Mechanics*, vol. 646, pp. 505–515, 2010.

[71] G. J. Elfring and E. Lauga, "Synchronization of flexible sheets," *Journal of Fluid Mechanics*, vol. 674, pp. 163–173, 2011.

[72] G. J. Elfring and E. Lauga, "Passive hydrodynamic synchronization of two-dimensional swimming cells," *Physics of Fluids*, vol. 23, no. 1, p. 011902, 2011.

[73] J. Simons, L. Fauci, and R. Cortez, "A fully three-dimensional model of the interaction of driven elastic filaments in a stokes flow with applications to sperm motility," *Journal of Biomechanics*, vol. 48, no. 9, pp. 1639–1651, 2015. Reproductive Biomechanics.

[74] P. Cripe, O. Richfield, and J. Simons, "Sperm pairing and measures of efficiency in planar swimming models," *Spora: A Journal of Biomathematics*, vol. 2, no. 1, p. 5, 2016.

[75] B. M. Friedrich, I. H. Riedel-Kruse, J. Howard, and F. Jülicher, "High-precision tracking of sperm swimming fine structure provides strong test of resistive force theory," *Journal of Experimental Biology*, vol. 213, no. 8, pp. 1226–1234, 2010.

[76] S. Werner, J. C. Rink, I. H. Riedel-Kruse, and B. M. Friedrich, "Shape mode analysis exposes movement patterns in biology: Flagella and flatworms as case studies," *PLoS One*, vol. 9, p. e113083, 2014.

[77] H. Winet, G. S. Bernstein, and J. Head, "Observations on the response of human spermatozoa to gravity, boundaries and fluid shear," *Reproduction*, vol. 70, no. 2, pp. 511–523, 1984.

[78] D. Woolley, "Motility of spermatozoa at surfaces," *Reproduction*, vol. 126, no. 2, pp. 259–270, 2003.

[79] T. Hyakutake, D. Higashiyama, and T. Tsuchiya, "Prediction of sperm motion behavior in microfluidic channel using sperm swimming model," *Journal of Biomechanics*, vol. 176, p. 112336, 2024.

[80] I. Riedel-Kruse, A. Hilfinger, J. Howard, and F. Jülicher, "How molecular motors shape the flagellar beat," *HFSP Journal*, vol. 1, no. 3, pp. 192–208, 2007.

[81] V. F. Geyer, F. Jülicher, J. Howard, and B. M. Friedrich, "Cell-body rocking is a dominant mechanism for flagellar synchronization in a swimming alga," *Proceedings of the National Academy of Sciences*, vol. 110, no. 45, pp. 18058–18063, 2013.

[82] R. Ma, G. S. Klindt, I. H. Riedel-Kruse, F. Jülicher, and B. M. Friedrich, "Active phase and amplitude fluctuations of flagellar beating," *Physical Review Letter*, vol. 113, no. 4, p. 048101, 2014.

[83] K. Y. Wan, K. C. Leptos, and R. E. Goldstein, "Lag, lock, sync, slip: the many 'phases' of coupled flagella," *Journal of The Royal Society Interface*, vol. 11, no. 94, p. 20131160, 2014.

[84] B. Kralemann, L. Cimponeriu, M. Rosenblum, A. Pikovsky, and R. Mrowka, "Uncovering interaction of coupled oscillators from data," *Physical Review E*, vol. 76, no. 5, p. 055201, 2007.

[85] B. Kralemann, L. Cimponeriu, M. Rosenblum, A. Pikovsky, and R. Mrowka, "Phase dynamics of coupled oscillators reconstructed from data," *Physical Review E*, vol. 77, no. 6, p. 066205, 2008.

[86] E. A. Gillies, R. M. Cannon, R. B. Green, and A. A. Pacey, "Hydrodynamic propulsion of human sperm," *Journal of Fluid Mechanics*, vol. 625, pp. 445–474, 2009.

[87] R. P. Amann and D. Waberski, "Computer-assisted sperm analysis (CASA): Capabilities and potential developments," *Theriogenology*, vol. 81, no. 1, pp. 5–17.e3, 2014.

[88] J.-w. Choi, L. Alkhoury, L. Urbano, P. Masson, and M. VerMilyea, "An assessment tool for computer-assisted semen analysis (CASA) algorithms," *Scientific Reports*, vol. 12, p. 16830, 2022.

[89] N. Lustgarten Guahmich, E. Borini, and N. Zaninovic, "Improving outcomes of assisted reproductive technologies using artificial intelligence for sperm selection," *Fertility and Sterility*, vol. 120, no. 4, pp. 729–734, 2023.

[90] World Health Organization, *WHO laboratory manual for the examination and processing of human semen*. Geneva: World Health Organization, 6th ed., 2021.

[91] D. Mortimer, "Laboratory standards in routine clinical andrology," *Reproductive Medicine Review*, vol. 3, no. 2, pp. 97–111, 1994.

[92] A. T. Chwang and T. Y.-T. Wu, "Hydromechanics of low-Reynolds-number flow. part 2. singularity method for stokes flows," *Journal of Fluid Mechanics*, vol. 67, no. 4, pp. 787–815, 1975.

[93] S. Kim and S. Karrila, *Microhydrodynamics: Principles and Selected Applications*. Butterworth - Heinemann series in chemical engineering, Dover Publications, 2005.

[94] E. Lauga, *The Fluid Dynamics of Cell Motility*. Cambridge Texts in Applied Mathematics, Cambridge University Press, 2020.

[95] J. Lighthill, "Flagellar hydrodynamics," *SIAM Review*, vol. 18, no. 2, pp. 161–230, 1976.

[96] G. J. Hancock and M. H. A. Newman, "The self-propulsion of microscopic organisms through liquids," *Proceedings of the Royal Society of London. Series A. Mathematical and Physical Sciences*, vol. 217, no. 1128, pp. 96–121, 1953.

[97] J. Gray and G. J. Hancock, "The propulsion of sea-urchin spermatozoa," *Journal of Experimental Biology*, vol. 32, no. 4, pp. 802–814, 1955.

[98] C. Brennen and H. Winet, "Fluid mechanics of propulsion by cilia and flagella," *Annual Review of Fluid Mechanics*, vol. 9, pp. 339–398, 1977.

[99] S. Pesch and M. Bergmann, "Structure of mammalian spermatozoa in respect to viability, fertility and cryopreservation," *Micron*, vol. 37, no. 7, pp. 597–612, 2006.

[100] C. B. Lindemann and K. A. Lesich, "Functional anatomy of the mammalian sperm flagellum," *Cytoskeleton*, vol. 73, no. 11, pp. 652–669, 2016.

[101] H. Jiang, J.-w. Kwon, S. Lee, Y.-J. Jo, S. Namgoong, X.-r. Yao, B. Yuan, J.-b. Zhang, Y.-K. Park, and N.-H. Kim, "Reconstruction of bovine spermatozoa substances distribution and morphological differences between holstein and korean native cattle using three-dimensional refractive index tomography," *Scientific Reports*, vol. 9, p. 8774, 2019.

[102] B. Rodenborn, C.-H. Chen, H. L. Swinney, B. Liu, and H. P. Zhang, "Propulsion of microorganisms by a helical flagellum," *Proceedings of the National Academy of Sciences*, vol. 110, no. 5, pp. E338–E347, 2013.

[103] Z. Wang, A. Klingner, V. Magdanz, M. W. Hoppenreijs, S. Misra, and I. S. M. Khalil, "Flagellar propulsion of sperm cells against a time-periodic interaction force," *Advanced Biology*, vol. 7, no. 1, p. 2200210, 2023.

[104] S. Kim, "Singularity solutions for ellipsoids in low-Reynolds-number flows: With applications to the calculation of hydrodynamic interactions in suspensions of ellipsoids," *International Journal of Multiphase Flow*, vol. 12, no. 3, pp. 469–491, 1986.

[105] E. Lauga, W. R. DiLuzio, G. M. Whitesides, and H. A. Stone, "Swimming in circles: Motion of bacteria near solid boundaries," *Biophysical Journal*, vol. 90, no. 2, pp. 400–412, 2006.

[106] T. Ishikawa, "Fluid dynamics of squirmers and ciliated microorganisms," *Annual Review of Fluid Mechanics*, vol. 56, pp. 119–145, 2024.

[107] A. Vilfan, "Optimal shapes of surface slip driven self-propelled microswimmers," *Physical Review Letter*, vol. 109, no. 12, p. 128105, 2012.

[108] C. M. Pooley, G. P. Alexander, and J. M. Yeomans, "Hydrodynamic interaction between two swimmers at low Reynolds number," *Physical Review Letter*, vol. 99, no. 22, p. 228103, 2007.

[109] J. E. Avron, O. Gat, and O. Kenneth, "Optimal swimming at low Reynolds numbers," *Physical Review Letter*, vol. 93, no. 18, p. 186001, 2004.

[110] D. Tam and A. E. Hosoi, "Optimal stroke patterns for purcell's three-link swimmer," *Physical Review Letter*, vol. 98, no. 6, p. 068105, 2007.

[111] L. Giraldi, P. Martinon, and M. Zoppello, "Controllability and optimal strokes for N-link microswimmer," in *52nd IEEE Conference on Decision and Control*, pp. 3870–3875, 2013.

[112] F. Alouges, A. DeSimone, L. Giraldi, and M. Zoppello, "Self-propulsion of slender micro-swimmers by curvature control: N-link swimmers," *International Journal of Non-Linear Mechanics*, vol. 56, pp. 132–141, 2013. Soft Matter: a nonlinear continuum mechanics perspective.

[113] S. E. Spagnolie and E. Lauga, "The optimal elastic flagellum," *Physics of Fluids*, vol. 22, no. 3, p. 031901, 2010.

[114] B. Liu, K. S. Breuer, and T. R. Powers, "Propulsion by a helical flagellum in a capillary tube," *Physics of Fluids*, vol. 26, no. 1, p. 011701, 2014.

[115] P. H. Htet, D. Das, and E. Lauga, "Hydrodynamic hovering of swimming bacteria above surfaces," *Physical Review Research*, vol. 6, p. L032070, Sep 2024.

[116] H. Ito, T. Omori, and T. Ishikawa, "Swimming mediated by ciliary beating: comparison with a squirmer model," *Journal of Fluid Mechanics*, vol. 874, pp. 774–796, 2019.

[117] T. Omori, H. Ito, and T. Ishikawa, "Swimming microorganisms acquire optimal efficiency with multiple cilia," *Proceedings of the National Academy of Sciences*, vol. 117, no. 48, pp. 30201–30207, 2020.

[118] M. J. Lighthill, "On the squirming motion of nearly spherical deformable bodies through liquids at very small Reynolds numbers," *Communications on Pure and Applied Mathematics*, vol. 5, no. 2, pp. 109–118, 1952.

[119] S. Michelin and E. Lauga, "Efficiency optimization and symmetry-breaking in a model of ciliary locomotion," *Physics of Fluids*, vol. 22, no. 11, p. 111901, 2010.

[120] T. J. Pedley, "Spherical squirmers: models for swimming microorganisms," *IMA Journal of Applied Mathematics*, vol. 81, no. 3, pp. 488–521, 2016.

[121] F. Alouges, A. Desimone, and A. Lefebvre-Lepot, "Optimal strokes for axisymmetric microswimmers," *The European Physical Journal E*, vol. 28, pp. 279–84, 2009.

[122] D. Klotsa, K. A. Baldwin, R. J. A. Hill, R. M. Bowley, and M. R. Swift, "Propulsion of a two-sphere swimmer," *Physical Review Letter*, vol. 115, no. 24, p. 248102, 2015.

[123] C. Datt, B. Nasouri, and G. J. Elfring, "Two-sphere swimmers in viscoelastic fluids," *Physical Review Fluids*, vol. 3, no. 12, p. 123301, 2018.

[124] H. Gadêlha, E. A. Gaffney, D. J. Smith, and J. C. Kirkman-Brown, "Nonlinear instability in flagellar dynamics: a novel modulation mechanism in sperm migration?," *Journal of The Royal Society Interface*, vol. 7, no. 53, pp. 1689–1697, 2010.

[125] J. Simons and A. Rosenberger, "Flagellar cooperativity and collective motion in sperm," *Fluids*, vol. 6, no. 10, p. 353, 2021.

[126] H. Gadêlha and E. A. Gaffney, "Flagellar ultrastructure suppresses buckling instabilities and enables mammalian sperm navigation in high-viscosity media," *Journal of The Royal Society Interface*, vol. 16, no. 152, p. 20180668, 2019.

[127] S. Wang, J. Burton, R. Behringer, and I. Larina, "In vivo micro-scale tomography of ciliary behavior in the mammalian oviduct," *Scientific Reports*, vol. 5, p. 13216, 2015.

[128] S. Yuan, Z. Wang, H. Peng, S. M. Ward, G. W. Hennig, H. Zheng, and W. Yan, "Oviductal motile cilia are essential for oocyte pickup but dispensable for sperm and embryo transport," *Proceedings of the National Academy of Sciences*, vol. 118, no. 22, p. e2102940118, 2021.

[129] R. Trouilloud, T. S. Yu, A. E. Hosoi, and E. Lauga, "Soft swimming: Exploiting deformable interfaces for low Reynolds number locomotion," *Physical Review Letter*, vol. 101, no. 4, p. 048102, 2008.

[130] E. Lauga and D. Bartolo, "No many-scallop theorem: Collective locomotion of reciprocal swimmers," *Physical Review E*, vol. 78, no. 3, p. 030901, 2008.

[131] A. Daddi-Moussa-Ider, B. Rallabandi, S. Gekle, and H. A. Stone, "Reciprocal theorem for the prediction of the normal force induced on a particle translating parallel to an elastic membrane," *Physical Review Fluids*, vol. 3, no. 8, p. 084101, 2018.

[132] A. Poddar, A. Bandopadhyay, and S. Chakraborty, "Near-wall hydrodynamic slip triggers swimming state transition of micro-organisms," *Journal of Fluid Mechanics*, vol. 894, p. A11, 2020.

[133] J. Elgeti, U. Kaupp, and G. Gompper, "Hydrodynamics of sperm cells near surfaces," *Biophysical Journal*, vol. 99, pp. 1018–1026, 2010.

[134] J. Simons, S. Olson, R. Cortez, and L. Fauci, "The dynamics of sperm detachment from epithelium in a coupled fluid-biochemical model of hyperactivated motility," *Journal of Theoretical Biology*, vol. 354, pp. 81–94, 2014.

[135] D. J. Smith, E. A. Gaffney, J. R. Blake, and J. C. Kirkman-brown, "Human sperm accumulation near surfaces: a simulation study," *Journal of Fluid Mechanics*, vol. 621, pp. 289–320, 2009.

[136] L. Carichino, D. Drumm, and S. D. Olson, "A computational study of hydrodynamic interactions between pairs of sperm with planar

and quasi-planar beat forms," *Frontiers in Physics*, vol. 9, p. 735438, 2021.

[137] G. S. Klindt and B. M. Friedrich, "Flagellar swimmers oscillate between pusher- and puller-type swimming," *Physical Review E*, vol. 92, no. 6, p. 063019, 2015.

[138] K. Ishimoto, H. Gadêlha, E. A. Gaffney, D. J. Smith, and J. Kirkman-Brown, "Coarse-graining the fluid flow around a human sperm," *Physical Review Letter*, vol. 118, no. 12, p. 124501, 2017.

[139] A. P. Berke, L. Turner, H. C. Berg, and E. Lauga, "Hydrodynamic attraction of swimming microorganisms by surfaces," *Physical Review Letter*, vol. 101, no. 3, p. 038102, 2008.

[140] S. Gluzman, D. A. Karpeev, and L. V. Berlyand, "Effective viscosity of puller-like microswimmers: a renormalization approach," *Journal of The Royal Society Interface*, vol. 10, no. 89, p. 20130720, 2013.

[141] G.-J. Li and A. M. Ardekani, "Hydrodynamic interaction of microswimmers near a wall," *Physical Review E*, vol. 90, no. 1, p. 013010, 2014.

[142] E. Lushi, V. Kantsler, and R. E. Goldstein, "Scattering of biflagellate microswimmers from surfaces," *Physical Review E*, vol. 96, no. 2, p. 023102, 2017.

[143] A.-J. Buchner, K. Muller, J. Mehmood, and D. Tam, "Hopping trajectories due to long-range interactions determine surface accumulation of microalgae," *Proceedings of the National Academy of Sciences*, vol. 118, no. 20, p. e2102095118, 2021.

[144] B. Pérez-Estay, M. L. Cordero, N. Sepúlveda, and R. Soto, "Accumulation and depletion of e. coli in surfaces mediated by curvature," *Physical Review E*, vol. 109, no. 5, p. 054601, 2024.

[145] J. R. Blake, "A note on the image system for a stokeslet in a no-slip boundary," *Mathematical Proceedings of the Cambridge Philosophical Society*, vol. 70, no. 2, pp. 303–310, 1971.

[146] J. R. Blake and A. T. Chwang, "Fundamental singularities of viscous flow," *Journal of Engineering Mathematics*, vol. 8, pp. 23–29, 1974.

[147] M. Ramia, D. Tullock, and N. Phan-Thien, "The role of hydrodynamic interaction in the locomotion of microorganisms," *Biophysical Journal*, vol. 65, no. 2, pp. 755–778, 1993.

[148] R. Cortez, "The method of regularized stokeslets," *SIAM Journal on Scientific Computing*, vol. 23, no. 4, pp. 1204–1225, 2001.

[149] R. Cortez, L. Fauci, and A. Medovikov, "The method of regularized stokeslets in three dimensions: Analysis, validation, and application to helical swimming," *Physics of Fluids*, vol. 17, no. 3, p. 031504, 2005.

[150] J. Ainley, S. Durkin, R. Embid, P. Boindala, and R. Cortez, "The method of images for regularized stokeslets," *Journal of Computational Physics*, vol. 227, no. 9, pp. 4600–4616, 2008.

[151] R. Cortez and D. Varela, "A general system of images for regularized stokeslets and other elements near a plane wall," *Journal of Computational Physics*, vol. 285, pp. 41–54, 2015.

[152] T. Vicsek and A. Zafeiris, "Collective motion," *Physics Reports*, vol. 517, no. 3, pp. 71–140, 2012.

[153] I. H. Riedel, K. Kruse, and J. Howard, "A self-organized vortex array of hydrodynamically entrained sperm cells," *Science*, vol. 309, no. 5732, pp. 300–303, 2005.

[154] A. Creppy, O. Praud, X. Druart, P. L. Kohnke, and F. Plouraboué, "Turbulence of swarming sperm," *Physical Review E*, vol. 92, no. 3, p. 032722, 2015.

[155] H. Fisher and H. Hoekstra, "Competition drives cooperation among closely related sperm of deer mice," *Nature*, vol. 463, pp. 801–803, 2010.

[156] M. Pearcy, N. Delescaille, P. Lybaert, and S. Aron, "Team swimming in ant spermatozoa," *Biology Letters*, vol. 10, no. 6, p. 20140308, 2014.

[157] Y. Yang, J. Elgeti, and G. Gompper, "Cooperation of sperm in two dimensions: Synchronization, attraction, and aggregation through hydrodynamic interactions," *Physical Review E*, vol. 78, no. 6, p. 061903, 2008.

[158] T. Ihle and D. M. Kroll, "Stochastic rotation dynamics. i. formalism, galilean invariance, and green-kubo relations," *Physical Review E*, vol. 67, no. 6, p. 066705, 2003.

[159] G. Gompper, T. Ihle, D. M. Kroll, and R. G. Winkler, *Multi-Particle Collision Dynamics: A Particle-Based Mesoscale Simulation Approach to the Hydrodynamics of Complex Fluids*, pp. 1–87. Berlin, Heidelberg: Springer Berlin Heidelberg, 2009.

[160] L. J. Fauci and C. S. Peskin, "A computational model of aquatic animal locomotion," *Journal of Computational Physics*, vol. 77, no. 1, pp. 85–108, 1988.

[161] S. D. Olson, S. S. Suarez, and L. J. Fauci, "Coupling biochemistry and hydrodynamics captures hyperactivated sperm motility in a simple flagellar model," *Journal of Theoretical Biology*, vol. 283, no. 1, pp. 203–216, 2011.

[162] N. Taketoshi, T. Omori, and T. Ishikawa, "Elasto-hydrodynamic interaction of two swimming spermatozoa," *Physics of Fluids*, vol. 32, no. 10, p. 101901, 2020.

[163] S. F. Schoeller and E. E. Keaveny, "From flagellar undulations to collective motion: predicting the dynamics of sperm suspensions," *Journal of The Royal Society Interface*, vol. 15, no. 140, p. 20170834, 2018.

[164] D. J. G. Pearce, L. A. Hoogerbrugge, K. A. Hook, H. S. Fisher, and L. Giomi, "Cellular geometry controls the efficiency of motile sperm aggregates," *Journal of Royal Society Interface*, vol. 15, no. 148, p. 20180702, 2018.

[165] H. Moore and D. A. Taggart, "Sperm pairing in the opossum increases the efficiency of sperm movement in a viscous environment," *Biology of Reproduction*, vol. 52, no. 4, pp. 947–953, 1995.

[166] H. Moore, K. Komrskova, N. Jenkins, and W. Breed, "Exceptional sperm cooperation in the wood mouse," *Nature*, vol. 418, pp. 174–177, 2002.

[167] S. Immler, "Sperm competition and sperm cooperation: the potential role of diploid and haploid expression," *Reproduction*, vol. 135, no. 3, pp. 275–283, 2008.

[168] S. Ishijima, S. A. Ishijima, and B. A. Afzelius, "Movement of turritella spermatozoa: Direction of propagation and chirality of flagellar bends," *Cell Motility*, vol. 44, no. 2, pp. 85–95, 1999.

[169] K. A. Hook, W. D. Weber, and H. S. Fisher, "Postcopulatory sexual selection is associated with sperm aggregate quality in peromyscus mice," *Behavioral Ecology*, vol. 33, no. 1, pp. 55–64, 2021.

[170] S. P. Flaherty, N. J. Swann, P. Primakoff, and D. G. Myles, "A role for the wh-30 protein in sperm-sperm adhesion during rouleaux formation in the guinea pig," *Developmental Biology*, vol. 156, no. 1, pp. 243–252, 1993.

[171] H. S. Fisher, L. Giomi, H. E. Hoekstra, and L. Mahadevan, "The dynamics of sperm cooperation in a competitive environment," *Proceedings of the Royal Society B: Biological Sciences*, vol. 281, no. 1790, p. 20140296, 2014.

[172] P. Hernandez-Herrera, F. Montoya, J. M. Rendón-Mancha, A. Darszon, and G. Corkidi, "3-d $+t$ human sperm flagellum tracing in low snr fluorescence images," *IEEE Transactions on Medical Imaging*, vol. 37, no. 10, pp. 2236–2247, 2018.

[173] B. Walker, K. Ishimoto, and R. Wheeler, "Automated identification of flagella from videomicroscopy via the medial axis transform," *Scientific Reports*, vol. 9, p. 5015, 2019.

[174] V. Kapoor, W. Hirst, C. Hentschel, S. Preibisch, and S. Reber, "Mtrack: Automated detection, tracking, and analysis of dynamic microtubules," *Scientific Reports*, vol. 9, p. 3794, 2019.

[175] M. T. Gallagher, G. Cupples, E. H. Ooi, J. C. Kirkman-Brown, and D. J. Smith, "Rapid sperm capture: high-throughput flagellar waveform analysis," *Human Reproduction*, vol. 34, no. 7, pp. 1173–1185, 2019.

[176] H. P. Zhang, A. Be'er, E.-L. Florin, and H. L. Swinney, "Collective motion and density fluctuations in bacterial colonies," *Proceedings of the National Academy of Sciences*, vol. 107, no. 31, pp. 13626–13630, 2010.

[177] S. Butail, N. Manoukis, M. Diallo, J. M. Ribeiro, T. Lehmann, and D. A. Paley, "Reconstructing the flight kinematics of swarming and mating in wild mosquitoes," *Journal of Royal Society Interface*, vol. 9, no. 75, pp. 2624–2638, 2012.

[178] J. Elgeti and G. Gompper, "Emergence of metachronal waves in cilia arrays," *Proceedings of the National Academy of Sciences*, vol. 110, no. 12, pp. 4470–4475, 2013.

[179] J. C. Nawroth, H. Guo, E. Koch, E. A. C. Heath-Heckman, J. C. Hermanson, E. G. Ruby, J. O. Dabiri, E. Kanso, and M. McFall-Ngai, "Motile cilia create fluid-mechanical microhabitats for the active recruitment of the host microbiome," *Proceedings of the National Academy of Sciences*, vol. 114, no. 36, pp. 9510–9516, 2017.

[180] F. Verni and P. Gualtieri, "Feeding behaviour in ciliated protists," *Micron*, vol. 28, no. 6, pp. 487–504, 1997.

[181] W. E. Burnett and J. Heinze, "Sperm bundles in the seminal vesicles of sexually mature lasius ant males," *PLoS One*, vol. 9, no. 3, pp. 1–4, 2014.

[182] M. Tătulea-Codrean and E. Lauga, "Elastohydrodynamic synchronization of rotating bacterial flagella," *Physical Review Letter*, vol. 128, no. 20, p. 208101, 2022.

[183] S. Camalet and F. Jülicher, "Generic aspects of axonemal beating," *New Journal of Physics*, vol. 2, no. 1, p. 324, 2000.

[184] J. Elgeti, U. B. Kaupp, and G. Gompper, "Response to comment on article: Hydrodynamics of sperm cells near surfaces," *Biophysical Journal*, vol. 100, no. 9, pp. 2321–2324, 2011.

[185] R. Yanagimachi, Y. D. Noda, M. Fujimoto, and G. L. Nicolson, "The distribution of negative surface charges on mammalian spermatozoa," *American Journal of Anatomy*, vol. 135, no. 4, pp. 497–519, 1972.

[186] A. Nandagiri, A. S. Gaikwad, D. L. Potter, R. Nosrati, J. Soria, M. K. O'Bryan, S. Jadhav, and R. Prabhakar, "Flagellar energetics from high-resolution imaging of beating patterns in tethered mouse sperm," *eLife*, vol. 10, p. e62524, 2021.

[187] T. Su, I. Choi, J. Feng, K. Huang, E. Mcleod, and A. Ozcan, "Sperm trajectories form chiral ribbons," *Scientific Reports*, vol. 3, p. 1664, 2013.

[188] G. K. Batchelor, "The stress system in a suspension of force-free particles," *Journal of Fluid Mechanics*, vol. 41, no. 3, pp. 545–570, 1970.

[189] D. J. Smith, E. A. Gaffney, H. Gadêlha, N. Kapur, and J. C. Kirkman-Brown, "Bend propagation in the flagella of migrating human sperm, and its modulation by viscosity," *Cell Motility*, vol. 66, no. 4, pp. 220–236, 2009.

[190] V. Magdanz, S. Sanchez, and O. G. Schmidt, "Development of a sperm-flagella driven micro-bio-robot," *Advanced Materials*, vol. 25, no. 45, pp. 6581–6588, 2013.

[191] P. T. Underhill, J. P. Hernandez-Ortiz, and M. D. Graham, "Diffusion and spatial correlations in suspensions of swimming particles," *Physical Review Letter*, vol. 100, no. 24, p. 248101, 2008.

[192] L. J. Fauci and A. McDonald, "Sperm motility in the presence of boundaries," *Bulletin of Mathematical Biology*, vol. 57, no. 5, pp. 679–699, 1995.

[193] K. Ishimoto, H. Gadêlha, E. A. Gaffney, D. J. Smith, and J. Kirkman-Brown, "Human sperm swimming in a high viscosity mucus analogue," *Journal of Theoretical Biology*, vol. 446, pp. 1–10, 2018.

[194] P. E. Lindahl and P. Sjöblom, "On Mechanisms of Head-to-Head Association in Bovine Spermatozoa," *Biology of Reproduction*, vol. 25, no. 1, pp. 29–43, 1981.

[195] J. J. Parrish, J. Susko-Parrish, M. A. Winer, and N. L. First, "Capacitation of bovine sperm by heparin," *Biology of Reproduction*, vol. 38, no. 5, pp. 1171–1180, 1988.

[196] B. M. Friedrich and F. Jülicher, "Flagellar synchronization independent of hydrodynamic interactions," *Physical Review Letter*, vol. 109, no. 13, p. 138102, 2012.

[197] D. R. Brumley, K. Y. Wan, M. Polin, and R. E. Goldstein, "Flagellar synchronization through direct hydrodynamic interactions," *eLife*, vol. 3, p. e02750, 2014.

[198] X.-Z. Chen, M. Hoop, F. Mushtaq, E. Siringil, C. Hu, B. J. Nelson, and S. Pané, "Recent developments in magnetically driven micro- and nanorobots," *Applied Materials Today*, vol. 9, pp. 37–48, 2017.

[199] D. González-Abreu, S. García-Martínez, V. Fernández-Espín, R. Romar, and J. Gadea, "Incubation of boar spermatozoa in viscous media by addition of methylcellulose improves sperm quality and penetration rates during in vitro fertilization," *Theriogenology*, vol. 92, pp. 14–23, 2017.

[200] F. Striggow, M. Medina-Sánchez, G. K. Auernhammer, V. Magdanz, B. M. Friedrich, and O. G. Schmidt, "Sperm-driven micromotors moving in oviduct fluid and viscoelastic media," *Small*, vol. 16, no. 24, p. 2000213, 2020.

[201] E. Olstad, C. Ringers, J. Hansen, A. Wens, C. Brandt, D. Wachten, E. Yaksi, and N. Jurisch-Yaksi, "Ciliary beating compartmentalizes cerebrospinal fluid flow in the brain and regulates ventricular development," *Current Biology*, vol. 29, no. 2, pp. 229–241.e6, 2019.

[202] H.-Q. Tu, S. Li, Y.-L. Xu, Y.-C. Zhang, P.-Y. Li, L.-Y. Liang, G.-P. Song, X.-X. Jian, M. Wu, Z.-Q. Song, T.-T. Li, H.-B. Hu, J.-F. Yuan, X.-L. Shen, J.-N. Li, Q.-Y. Han, K. Wang, T. Zhang, T. Zhou, A.-L. Li, X.-M. Zhang, and H.-Y. Li, "Rhythmic cilia changes support

scn neuron coherence in circadian clock," *Science*, vol. 380, no. 6648, pp. 972–979, 2023.

[203] J. Nawroth, A. Does, A. (Firth), and E. Kanso, "Multiscale mechanics of mucociliary clearance in the lung," *Philosophical Transactions of the Royal Society B: Biological Sciences*, vol. 375, p. 20190160, 2019.

[204] D. Tam and A. E. Hosoi, "Optimal feeding and swimming gaits of biflagellated organisms," *Proceedings of the National Academy of Sciences*, vol. 108, no. 3, pp. 1001–1006, 2011.

[205] K.-I. Okamoto and Y. Nakaoka, "Reconstitution of Metachronal Waves in Ciliated Cortical Sheets of Paramecium: I. Wave Stabilities," *Journal of Experimental Biology*, vol. 192, no. 1, pp. 61–72, 1994.

[206] T. Ishikawa and M. Hota, "Interaction of two swimming Paramecia," *Journal of Experimental Biology*, vol. 209, no. 22, pp. 4452–4463, 2006.

[207] M. Polin, I. Tuval, K. Drescher, J. P. Gollub, and R. E. Goldstein, "Chlamydomonas swims with two gears in a eukaryotic version of run-and-tumble locomotion," *Science*, vol. 325, no. 5939, pp. 487–490, 2009.

[208] K. Zhang, A. Klingner, Y. L. Gars, S. Misra, V. Magdanz, and I. S. M. Khalil, "Locomotion of bovine spermatozoa during the transition from individual cells to bundles," *Proceedings of the National Academy of Sciences*, vol. 120, no. 3, p. e2211911120, 2023.

[209] R. Di Leonardo, A. Búzás, L. Kelemen, G. Vizsnyiczai, L. Oroszi, and P. Ormos, "Hydrodynamic synchronization of light driven microrotors," *Physical Review Letter*, vol. 109, no. 3, p. 034104, 2012.

[210] M. Tătulea-Codrean and E. Lauga, "Elastohydrodynamic synchronization of rotating bacterial flagella," *Physical Review Letter*, vol. 128, no. 20, p. 208101, 2022.

[211] S. Samatas and J. Lintuvuori, "Hydrodynamic synchronization of chiral microswimmers," *Physical Review Letter*, vol. 130, no. 2, p. 024001, 2023.

[212] J. Elgeti, R. G. Winkler, and G. Gompper, "Physics of microswimmers—single particle motion and collective behavior: a review," *Reports on Progress in Physics*, vol. 78, no. 5, p. 056601, 2015.

[213] R. Pramanik, R. W. C. P. Verstappen, and P. R. Onck, "Nature-inspired miniaturized magnetic soft robotic swimmers," *Applied Physics Reviews*, vol. 11, no. 2, p. 021312, 2024.

[214] M. Zaferani, F. Javi, A. Mokhtare, P. Li, and A. Abbaspourrad, "Rolling controls sperm navigation in response to the dynamic rheological properties of the environment," *eLife*, vol. 10, p. e68693, 2021.

[215] C. Li, B. Chakrabarti, P. Castilla, A. Mahajan, and D. Saintillan, "Chemomechanical model of sperm locomotion reveals two modes of swimming," *Physical Review Fluids*, vol. 8, no. 11, p. 113102, 2023.

[216] J. O. Carvalho, L. P. Silva, R. Sartori, and M. A. N. Dode, "Nanoscale differences in the shape and size of x and y chromosome-bearing bovine sperm heads assessed by atomic force microscopy," *PLoS One*, vol. 8, no. 3, pp. 1–7, 2013.

[217] P. Bayly, B. Lewis, E. Ranz, R. Okamoto, R. Pless, and S. Dutcher, "Propulsive forces on the flagellum during locomotion of chlamydomonas reinhardtii," *Biophysical Journal*, vol. 100, no. 11, pp. 2716–2725, 2011.

[218] A. Gong, S. Rode, U. B. Kaupp, G. Gompper, J. Elgeti, B. M. Friedrich, and L. Alvarez, "The steering gaits of sperm," *Philosophical Transactions of the Royal Society B: Biological Sciences*, vol. 375, no. 1792, p. 20190149, 2020.

[219] A. Yundt, W. Shack, and T. Lardner, "Applicability of hydrodynamic analyses of spermatozoan motion," *Journal of Experimental Biology*, vol. 62, no. 1, pp. 27–41, 1975.

[220] T. Eiter and H. Mannila, "Computing discrete fréchet distance," tech. rep., Technische Universitat Wien, 1994.

[221] K. C. Leptos, K. Y. Wan, M. Polin, I. Tuval, A. I. Pesci, and R. E. Goldstein, "Antiphase synchronization in a flagellar-dominance mu-

tant of chlamydomonas," *Physical Review Letter*, vol. 111, no. 15, p. 158101, 2013.

[222] G. Quaranta, M.-E. Aubin-Tam, and D. Tam, "Hydrodynamics versus intracellular coupling in the synchronization of eukaryotic flagella," *Physical Review Letter*, vol. 115, no. 23, p. 238101, 2015.

[223] K. Y. Wan and R. E. Goldstein, "Coordinated beating of algal flagella is mediated by basal coupling," *Proceedings of the National Academy of Sciences*, vol. 113, no. 20, pp. E2784–E2793, 2016.

[224] H. Guo, L. Fauci, M. Shelley, and E. Kanso, "Bistability in the synchronization of actuated microfilaments," *Journal of Fluid Mechanics*, vol. 836, pp. 304–323, 2018.

[225] H. Guo, Y. Man, K. Y. Wan, and E. Kanso, "Intracellular coupling modulates biflagellar synchrony," *Journal of The Royal Society Interface*, vol. 18, no. 174, p. 20200660, 2021.

[226] N. Uchida and R. Golestanian, "Generic conditions for hydrodynamic synchronization," *Physical Review Letter*, vol. 106, no. 5, p. 058104, 2011.

[227] R. Golestanian, J. M. Yeomans, and N. Uchida, "Hydrodynamic synchronization at low Reynolds number," *Soft Matter*, vol. 7, no. 7, pp. 3074–3082, 2011.

[228] G. S. Klindt, C. Ruloff, C. Wagner, and B. M. Friedrich, "In-phase and anti-phase flagellar synchronization by waveform compliance and basal coupling," *New Journal of Physics*, vol. 19, no. 11, p. 113052, 2017.

[229] D. J. Hickey, R. Golestanian, and A. Vilfan, "Nonreciprocal interactions give rise to fast cilium synchronization in finite systems," *Proceedings of the National Academy of Sciences*, vol. 120, no. 40, p. e2307279120, 2023.

[230] N. Osterman and A. Vilfan, "Finding the ciliary beating pattern with optimal efficiency," *Proceedings of the National Academy of Sciences*, vol. 108, no. 38, pp. 15727–15732, 2011.

[231] R. E. Goldstein, E. Lauga, A. I. Pesci, and M. R. E. Proctor, "Elastohydrodynamic synchronization of adjacent beating flagella," *Physical Review Fluids*, vol. 1, no. 7, p. 073201, 2016.

[232] W. Liao and E. Lauga, "Energetics of synchronization for model flagella and cilia," *Physical Review E*, vol. 103, no. 4, p. 042419, 2021.

[233] R. E. Johnson, "An improved slender-body theory for stokes flow," *Journal of Fluid Mechanics*, vol. 99, no. 2, pp. 411–431, 1980.

[234] I. Riedel, *Mechanics of the axoneme: Self-organized beating patterns and vortex arrays of spermatozoa*. PhD thesis, Ph. D. dissertation, TU Dresden, 2005.

[235] A. Chen, C. Li, S. Zou, M. M. Rahaman, Y. Yao, H. Chen, H. Yang, P. Zhao, W. Hu, W. Liu, and M. Grzegorzek, "Svia dataset: A new dataset of microscopic videos and images for computer-aided sperm analysis," *Biocybernetics and Biomedical Engineering*, vol. 42, no. 1, pp. 204–214, 2022.

[236] I. Tiab, A. Belaid, S. Yahiaoui, D. Belazzougui, N. Hafsi, and M. Iguer-Ouada, "Deep characterization for sperm analysis: Leveraging a novel dataset to enhance motility assessments," in *2024 IEEE 7th International Conference on Advanced Technologies, Signal and Image Processing (ATSIP)*, vol. 1, pp. 200–205, 2024.

[237] T. B. Haugen, S. A. Hicks, J. M. Andersen, O. Witczak, H. L. Hammer, R. Borgli, P. Halvorsen, and M. Riegler, "VISEM: a multimodal video dataset of human spermatozoa," in *Proceedings of the 10th ACM Multimedia Systems Conference*, MMSys '19, (New York, NY, USA), pp. 261–266, Association for Computing Machinery, 2019.

[238] V. Thambawita, S. Hicks, A. Storås, T. Nguyen, J. Andersen, O. Witczak, T. Haugen, H. Hammer, P. Halvorsen, and M. Riegler, "VISEM-tracking, a human spermatozoa tracking dataset," *Scientific Data*, vol. 10, p. 260, 05 2023.

[239] F. Ghasemian, S. A. Mirroshandel, S. Monji-Azad, M. Azarnia, and Z. Zahiri, "An efficient method for automatic morphological abnormality detection from human sperm images," *Computer Methods and Programs in Biomedicine*, vol. 122, no. 3, pp. 409–420, 2015.

[240] S. Javadi and S. A. Mirroshandel, "A novel deep learning method for automatic assessment of human sperm images," *Computers in Biology and Medicine*, vol. 109, pp. 182–194, 2019.

[241] F. Shaker, S. A. Monadjemi, J. Alirezaie, and A. R. Naghsh-Nilchi, "A dictionary learning approach for human sperm heads classification," *Computers in Biology and Medicine*, vol. 91, pp. 181–190, 2017.

[242] H. O. Ilhan, I. O. Sigirci, G. Serbes, and N. Aydin, "A fully automated hybrid human sperm detection and classification system based on mobile-net and the performance comparison with conventional methods," *Medical Biological Engineering Computing*, vol. 58, pp. 1047–1068, 03 2020.

[243] V. Chang, A. Garcia, N. Hitschfeld, and S. Härtel, "Gold-standard for computer-assisted morphological sperm analysis," *Computers in Biology and Medicine*, vol. 83, pp. 143–150, 2017.

[244] G. Dardikman-Yoffe, S. K. Mirsky, I. Barnea, and N. T. Shaked, "High-resolution 4-d acquisition of freely swimming human sperm cells without staining," *Science Advances*, vol. 6, no. 15, p. eaay7619, 2020.

[245] G. Corkidi, B. Taboada, C. Wood, A. Guerrero, and A. Darszon, "Tracking sperm in three-dimensions," *Biochemical and Biophysical Research Communications*, vol. 373, no. 1, pp. 125–129, 2008.

[246] F. Silva-Villalobos, J. A. Pimentel, A. Darszon, and G. Corkidi, "Imaging of the 3d dynamics of flagellar beating in human sperm," in *2014 36th Annual International Conference of the IEEE Engineering in Medicine and Biology Society*, pp. 190–193, 2014.

[247] F. Sadak, E. Gerena, C. Dupont, R. Lévy, and S. Haliyo, "Human sperm detection and tracking using event-based cameras and unsupervised learning," in *2024 International Conference on Manipulation, Automation and Robotics at Small Scales (MARSS)*, pp. 1–6, 2024.

[248] R. E. Goldstein, M. Polin, and I. Tuval, "Noise and synchronization in pairs of beating eukaryotic flagella," *Physical Review Letter*, vol. 103, no. 16, p. 168103, 2009.

[249] K. Y. Wan and R. N. Poon, "Mechanisms and functions of multiciliary coordination," *Current Opinion in Cell Biology*, vol. 86, p. 102286, 2024.

[250] C. Ringers, S. Bialonski, M. Ege, A. Solovev, J. N. Hansen, I. Jeong, B. M. Friedrich, and N. Jurisch-Yaksi, "Novel analytical tools reveal that local synchronization of cilia coincides with tissue-scale metachronal waves in zebrafish multiciliated epithelia," *eLife*, vol. 12, p. e77701, 2023.

[251] M. R. Leung, J. Zeng, X. Wang, M. C. Roelofs, W. Huang, R. Zenezini Chiozzi, J. F. Hevler, A. J. Heck, S. K. Dutcher, A. Brown, R. Zhang, and T. Zeev-Ben-Mordehai, "Structural specializations of the sperm tail," *Cell*, vol. 186, no. 13, pp. 2880–2896.e17, 2023.

[252] C. B. Lindemann, "A model of flagellar and ciliary functioning which uses the forces transverse to the axoneme as the regulator of dynein activation," *Cell Motility*, vol. 29, no. 2, pp. 141–154, 1994.

[253] C. B. Lindemann, "A "geometric clutch" hypothesis to explain oscillations of the axoneme of cilia and flagella," *Journal of Theoretical Biology*, vol. 168, no. 2, pp. 175–189, 1994.

[254] C. Brokaw, "Computer simulation of flagellar movement. i. demonstration of stable bend propagation and bend initiation by the sliding filament model," *Biophysical Journal*, vol. 12, no. 5, pp. 564–586, 1972.

[255] M. Hines and J. Blum, "Bend propagation in flagella. i. derivation of equations of motion and their simulation," *Biophysical Journal*, vol. 23, no. 1, pp. 41–57, 1978.

[256] Y. Morita and C. Shingyoji, "Effects of imposed bending on microtubule sliding in sperm flagella," *Current Biology*, vol. 14, no. 23, pp. 2113–2118, 2004.

[257] C. J. Brokaw, "Thinking about flagellar oscillation," *Cell Motility*, vol. 66, no. 8, pp. 425–436, 2009.

[258] P. Sartori, V. F. Geyer, A. Scholich, F. Jülicher, and J. Howard, "Dynamic curvature regulation accounts for the symmetric and asymmetric beats of *Chlamydomonas* flagella," *eLife*, vol. 5, p. e13258, 2016.

[259] C. J. Brokaw, "Molecular mechanism for oscillation in flagella and muscle.," *Proceedings of the National Academy of Sciences*, vol. 72, no. 8, pp. 3102–3106, 1975.

[260] F. Jülicher and J. Prost, "Spontaneous oscillations of collective molecular motors," *Physical Review Letter*, vol. 78, no. 23, pp. 4510–4513, 1997.

[261] A. Hilfinger, A. K. Chattopadhyay, and F. Jülicher, "Nonlinear dynamics of cilia and flagella," *Physical Review E*, vol. 79, no. 5, p. 051918, 2009.

[262] H. Gadêlha, E. A. Gaffney, and A. Goriely, "The counterbend phenomenon in flagellar axonemes and cross-linked filament bundles," *Proceedings of the National Academy of Sciences*, vol. 110, no. 30, pp. 12180–12185, 2013.

[263] T. Qiu, T.-C. Lee, A. Mark, K. Morozov, R. Münster, O. Mierka, S. Turek, A. Leshansky, and P. Fischer, "Swimming by reciprocal motion at low Reynolds number," *Nature communications*, vol. 5, p. 5119, 11 2014.

[264] T. Kobayashi and R. Yamamoto, "Steady motions of single spherical microswimmers in non-newtonian fluids," *Physics of Fluids*, vol. 36, p. 121912, 12 2024.

[265] G. Li, E. Lauga, and A. M. Ardekani, "Microswimming in viscoelastic fluids," *Journal of Non-Newtonian Fluid Mechanics*, vol. 297, p. 104655, 2021.

[266] G.-J. Li and A. Ardekani, "Undulatory swimming in non-newtonian fluids," *Journal of Fluid Mechanics*, vol. 784, p. R4, 12 2015.

[267] H. Xu, M. Medina-Sánchez, V. Magdanz, L. Schwarz, F. Hebenstreit, and O. G. Schmidt, "Sperm-hybrid micromotor for targeted drug delivery," *ACS Nano*, vol. 12, no. 1, pp. 327–337, 2018. PMID: 29202221.

[268] N. Celi, J. Cai, H. Sun, L. Feng, D. Zhang, and D. Gong, "Biohybrid flexible sperm-like microrobot for targeted chemo-photothermal therapy," *ACS Applied Materials & Interfaces*, vol. 16, pp. 24341–24350, 04 2024.

[269] I. S. M. Khalil, A. Fatih Tabak, A. Klingner, and M. Sitti, "Magnetic propulsion of robotic sperms at low-Reynolds number," *Applied Physics Letters*, vol. 109, p. 033701, 07 2016.

[270] H.-W. Huang, F. E. Uslu, P. Katsamba, E. Lauga, M. S. Sakar, and B. J. Nelson, "Adaptive locomotion of artificial microswimmers," *Science Advances*, vol. 5, no. 1, p. eaau1532, 2019.

[271] M. Wang, T. Wu, R. Liu, Z. Zhang, and J. Liu, "Selective and independent control of microrobots in a magnetic field: A review," *Engineering*, vol. 24, pp. 21–38, 2023.

Acknowledgements

Now I can start writing the Acknowledgements—the part of a thesis I like most every time. But this part also always makes me sentimental. When the first word of this page is written down, I know that my wonderful time in the Netherlands is coming to an end. Time flies. Some people, I want to thank.

First, I would like to express my sincere gratitude to my supervisor **Prof. Sarthak Misra**. I still remember the day I sent an email to you, and you replied and suggested arranging an online meeting in a few weeks. I did not realize that day that I would later come to Groningen, but now four years have passed. Over the past four years at Surgical Robotics Lab, I have grown significantly as a researcher and learned to work professionally under your mentorship. I really appreciate that you give me much academic freedom so that I can explore some areas of scientific research. Even though some explorations failed, the academic outputs in this thesis could not have happened without your great support. In addition, I would like to express my sincere gratitude to my supervisor **Dr. Islam Khalil**. I deeply thank you for your patience and great help in my scientific research, especially the first year when I did not even know how to start writing an academic paper. Your mentorship guides me to move forward on the right track. Your time spent in our meetings and your knowledge and experiences shared in our discussions have enabled me to complete my academic journey over the past four years. I probably would have given up when facing some challenges without your continuous encouragement and trust.

I would also like to express my appreciation to the members of my assessment committee—**Prof. Romana Schirhagl** from the University Medical Center Groningen and the University of Groningen, **Prof. Yang He** from the Northwestern Polytechnical University, **Prof. Patrick Onck** from the University of Groningen. I am very grateful for your valuable insights and constructive comments on my thesis, as well as your critical evaluation of my research. In addition, I would like to express my sincere gratitude to **Dr. Juliane Simmchen** from the University of Strathclyde, **Dr. Prashant Sharma** from the University Medical Center Groningen and the University of Groningen, and **Dr. Arturo Susarrey Arce** from

the University of Twente. Thank you for accepting my invitation to serve as the members of my examining committee.

I want to thank my labmates. **Zhengya**, you are a nice person. Your perseverance in research has earned my respect. **Yiyang**, thank you for coming downstairs to pick me up when I left my UMCG pass at home. **Chuang**, I like your upstanding personality. I will remember the happy time we cycled around the lake and talked on the train. **Zihan**, we have been sitting in the same office for the past four years. We talked a lot, from which I was often enlightened. I also received a lot of help from you. Wish you can achieve what you have been longing for. **Chen**, thank you for helping me a lot, like helping me move furniture to my room, instructing me in the use of the saw, and giving me a lift to Enschede. Wish you and **Yiling** can achieve what you desire in the near future. **Zhuoyue**, thank you for your help in the 3D printing. It was very happy to visit Italy with you when we were wandering around the cities listening to the melodious music in the streets. But we never had another chance to hang out after your wife came to you. **Adriana Vasi**, you are always helpful and your spirited vibe always brings happiness to us. Hope you have a wonderful, fruitful and happy PhD journey for the next few years.

Venkat Kalpathy Venkiteswaran, **Jeanine Lodeweges-de Vries**, **Mert Kaya**, **Sumit Mohanty**, **Theodosia Lourdes Thomas**, **Juan Julian Jesus Huaroto Sevilla**, **Amin Lotfiani**, **Michiel Richter**, **Yu-Hsiang Lin**, and **Yuxin Jin**. Thank you for your warm welcome every time I went to Enschede.

I also want to thank the staff of the Department of Biomaterials & Biomedical Technology (BBT)—**Hélder Santos**, **Henny van der Mei**, **Henk Busscher**, **Inge Zuhorn**, **Patrick van Rijn**, **Theo van kooten**, **Brandon Peterson**, **Ali Shahbazi**, **Monize Caiado Decarli**, **Ed de Jong**, **Joop de Vries**, **Willem Woudstra**, **Jelly Atema**, **Marja Slomp**, **Wytse Hogewerf**, **Willy de Haan**, **Reinier Bron**, **Willy van den Beukel-Koebrugge**, and **Stephen Sullivan**. Your efforts in providing a fantastic academic environment greatly benefit every BBT member including me.

Dize Li, **Lei Li**, **Raquel Bártolo Vitor**, **Siyu Fan**, **Fenghua Zhao**, **Xixi Wu**, **Yuanyuan Chai**, and **Hui Ting Li**, thank you for your kind help during my stay in the BBT. In addition, I want to convey my appreciation to my officemates and colleagues in the BBT—**Renata Maia**,

Sidi Liu, **Arturo Elías Llumbet**, **Jiachen Li**, **Han Gao**, **Anastasia Sevciuc**, **Suzan Abrishami**, **Huijie Han**, **Minle Zhan**, **Torben van der Boon**, **Harsh Jain**, **Tianqi Feng**, **Yuewen Zhu**, **Jie Gao**, **Kaiqi Wu**, **Yue Zhang**, **Yong Chen**, **Meng Qiao**, **Ke Ren**, **Yuanlong Cao**, **Guang Yang**, and **Guimei Jiang**. It is wonderful to work and chat with you.

I acknowledge financial support from the China Scholarship Council. Moreover, I want to express my thanks to **Yinan Wang** and **Jiayan Wang**, thank you for your great help when I was helpless. You are the sunlight through the heavy clouds, bringing me warmth. **Hugh** (**Jiliang Liu**) and **Ruoyu Chen**, it is pleasant to chat with you. Your knowledge and wisdom inspire me significantly and open a gate to a new world.

To my beloved family, there is no need to say anything more. You are my everything. But here I want to and have to express my deep gratitude to my lovely girlfriend, **Mengyu**. Without you, I cannot imagine how easy my work and life would be. But, without you, how boring my life would be. You are not only my dearest but also my best friend.